
POLITECNICO DI TORINO

Master of Science in Building Engineering

MASTER'S DEGREE THESIS

# Investigation Of Post-Construction Stress Distribution and Influence of Deficiencies in Post-Tension System.

Supervisor:
Prof. Eng. Marco Domaneschi
Co-supervisors:
Eng. Mattia Mairone
Eng. Rebecca Asso
Eng. Davide Masera

Candidate:
Abdul Razzak Mohammad

---

March 2024 - A.Y. 2023/2024

## Abstract:

Stress losses in tendons of post-tensioned bridges not only significantly impact their structural performance but also pose risks to their serviceability state and overall integrity over time. These losses can lead to a reduction in structural capacity due to decreased prestress force, increased deflection under load, and the development of cracks compromising structural integrity. Furthermore, they contribute to a loss of structural redundancy and heightened vulnerability to dynamic loading effects such as fatigue and damage.

This research aims to investigate the implications of such damage during both construction and operational lifespan of a post-tensioned bridge located in northern Italy, highlighting the crucial factors affecting its long-term performance and safety. Specifically, the author aimed to identify and quantify the consequences of progressive tendon damage during both construction and service life, to establish potential causes of failure, and to predict the bridge's current state and remaining lifespan. These objectives were addressed through a comprehensive approach involving simulation of a replica bridge using Finite element modelling. Various scenario tests were conducted to reflect real-life damage and stress loss in tendons, including stress losses due to friction, concrete instantaneous deformation, and long-term relaxation of the tendons. Additionally, scenarios accounted for corrosion and pitting effects. To ensure the accuracy and reliability of the data, extensive verification was undertaken through both hand calculations and comparison with data from previous research works.

After conducting extensive simulations on the bridge, it was determined that immediate stress losses, comprising friction losses and losses due to concrete instantaneous deformation, in addition to long-term losses, affects the serviceability state of the bridge after 55 years. Regarding corrosion effects, it was found that it takes over 100 years for sufficient diffusion of chlorides into the concrete at the tendon level to initiate corrosion. In cases of execution errors leading to water seepage into tendon ducts, corrosion was considered to begin immediately, resulting in the initiation of tendon area loss due to pitting. When stress losses are combined with pitting effects, the most conservative scenario indicates crack initiation after 29 years. The harvested data played a crucial role in understanding how the bridge behaves in different situations, giving us valuable insights into its structural response and expected lifespan.

# Acknowledgments

A special thanks goes to my supervisor Professor, Marco Domaneschi, who has guided me, with his endless availability, through every step of completing this paper, starting from the choice of the topic.

I am grateful to the "Masera Engineering Group" led by Dr. Davide Masera, for welcoming me and offering me the opportunity to work on an engaging topic for my master's thesis.

Thanks also to my co-advisors, Rebbeca Asso and Mattia Mairone. I extend my sincere appreciation to you for your unwavering support and invaluable contributions to this research project. Your theoretical guidance and professional advice have played a crucial role in shaping the direction and depth of this work. I am immensely grateful for your constant backing and guidance throughout every phase of this research endeavor.

Thanks to Harpaceas for their generous support in providing the software license for Midas Civil, which was essential to the success of this thesis.

I am infinitely grateful to my family and friends who have always supported me, backing every decision of mine, from the beginning of my initial academic journey.

I dedicate this paper to the sleepless nights, anxieties, and fears, but also to the joys and victories obtained throughout my complex academic journey. Lastly, I dedicate this thesis to myself, to my sacrifices, and to my tenacity that has allowed me to come this far.

# Table of Contents

# Table of Figures

# Table of Tables

# 1. INTRODUCTION

Bridges are vital components of transportation infrastructure, facilitating the movement of goods and people across vast distances. However, when bridge failures occur, their consequences extend far beyond the loss of the structure itself. The economic impact can be substantial, encompassing not only the value of the asset but also the loss of human lives and disruptions to traffic flow (G. C. Lee et al. 2013).

While various assessment methods exist for detecting corrosion in reinforced concrete structures, Jeon et al. the challenges are amplified in post-tensioned bridges. Unlike pre-tensioned bridges where strands are placed in concrete without ducts, post-tensioned bridges feature strands enclosed within metallic ducts, thereby impacting the reliability and performance of non-destructive evaluation (NDE) techniques (Hurlebaus et al. 2016). In the case of pre-tensioned bridges, conventional NDE and destructive evaluation (DE) methods developed for reinforced concrete can be employed to identify reinforcement corrosion. However, the presence of ducts in post-tensioned bridges necessitates more specialized approaches.

Nonetheless, the importance of understanding bridge damage and learning from past failures is widely recognized in the field of bridge engineering (Choudhury and Hasnat 2015). This knowledge serves as a valuable resource for improving design practices, enhancing maintenance protocols, and ensuring the long-term performance and safety of bridge structures.

This thesis aims to address the challenges associated with identifying and quantifying the consequences of tendon failure, establishing potential causes of failure, and predicting the bridge's current state and remaining lifespan. It will delve into the complexities of evaluating tendon damages in post-tensioning strands, considering the limitations of NDE techniques and the necessity of destructive testing. Additionally, the thesis will explore the lessons learned from historical bridge failures and examine the technical knowledge derived from these incidents. This study seeks to contribute to the development of a comprehensive approach for deformation assessment and management in post-tensioned bridges, ultimately enhancing their durability and reliability.

## 1.1. Research Purpose

The primary aim of this collaborative research is to enhance the understanding of the structural implications arising from damage and corrosion in post-tensioned systems, while also conducting a comprehensive investigation into diverse methods for identifying defects in post-tensioned bridges. The research seeks to delve into potential failure mechanisms, such as inadequate grouting leading to tendon corrosion or anchor corrosion. Through a meticulous analysis of specific post-tensioned system failures, the research will recalibrate critical cross-sections to gain valuable insights into their impact on the serviceability state of structures. Furthermore, relevant case studies will be carefully selected to have better knowledge about the consequences in scenarios of post-tensioned system damage. By centring on these key areas, the thesis aims to make a significant contribution to the knowledge base in the field, fostering the advancement of practices that ensure the safety and durability of post-tensioned bridge infrastructure.

### ➢ Main objectives & sub-objectives

The main goal of this collaborative research is to enhance the comprehension of the structural implications arising from damage and corrosion in post-tensioned systems, while also comprehensively investigating the diverse array of methods available for identifying defects in post-tensioned bridges. This aim encompasses the following key areas:

- Exploring and comprehending various methods for detecting deformations in post-tensioned bridges.
- Assessing the influence of specific post-tensioned system deficiencies on the serviceability state of structure.
- Advancing knowledge regarding potential failure mechanisms, such as the corrosion of tendons due to chlorination or execution mistakes.
- Selecting relevant case studies to develop comprehensive guidelines to understand structural consequences in cases of post-tensioned system damage.

### ➢ Research questions.

This collaborative research aims to delve into the complexities of post-tensioned systems and their vulnerabilities, seeking to address critical questions concerning potential mechanisms of failure, the impact of system deficiencies on serviceability state of structures, guidelines for assessing structural consequences, and methods for detecting deformations.

- What are the various methods available for detecting deformations in post-tensioned bridges, and how can their effectiveness be comprehended to ensure early detection of potential issues?
- What are the potential mechanisms of failure in post-tensioned systems, specifically focusing on the losses of stress and area in tendons?
- Which relevant case studies can be selected to develop comprehensive understanding for structural consequences in cases of post-tensioned system damage?
- How do specific post-tensioned system failures influence the Serviceability state of the structures?

## 1.2. Research Methodology

This research seeks to comprehensively investigate the structural implications arising from damage and corrosion in post-tensioned bridge systems. The methodology encompasses several key components to achieve the research objectives.

The study will commence with an extensive literature review, which will critically analyze relevant academic works, technical papers, and industry reports. The literature review will cover crucial topics, including a comprehensive list of Non-Destructive Evaluation (NDE) methods employed for inspecting internal tendons in post-tensioned bridges, failure categorization, causes of failures, and their impact on the overall performance of post-tensioned bridges. Additionally, the review will explore the presence of warning signs, the location and age of failures, and a quantitative study of corrosion products in such structures. Furthermore, Italian guidelines pertaining to risk management and safety assessment for existing bridges will be reviewed to inform the practical implications of the research.

Subsequently, a pertinent case study of the Morandi Bridge failure will be presented and discussed. This case study will serve as a critical reference point to gain deeper insights into real-world implications and challenges associated with post-tensioned bridge deficiencies.

Following the case study, an in-depth analysis of a Bridge located in northern Italy will be conducted. Specifically, this analysis will focus on examining the impact of stress loss and cross-sectional area loss in tendons on the overall structural stability of the bridge. Utilizing advanced analytical tools and simulation techniques, this investigation aims to highlight the critical role of tendons in maintaining the integrity and serviceability state of post-tensioned bridges.

Finally, the research will conclude with a comprehensive discussion of the obtained results, drawing meaningful connections between the literature review, the Polcevera bridge, and the results of the Bridge under study. This discussion will provide valuable insights into the practical implications of the research findings and offer recommendations for enhancing the safety, resilience, and maintenance practices of post-tensioned bridge systems.

# 2. LITERATURE REVIEW

In this section of the master's degree thesis, a comprehensive exploration of Non-Destructive Evaluation (NDE) methods and failure categorization in post-tensioned bridges is presented. The aim is to provide a thorough understanding of the various techniques utilized for assessing the condition of bridges without causing damage, as well as to categorize different failure modes and their impact on bridge structures. The literature review delves into specific NDE methods such as electromagnetic, radiography, magnetic, mechanical wave and vibration, ultrasonics, visual, electrochemical, and sensor methods, offering insights into their principles, applications, and limitations. Additionally, the discussion encompasses failure categorization aspects including causes of failure, effects of incorrect tendon layout on structural deflection, warning signs, collapse, demolition, failure age, failure location, corrosion causes and warning signs, corrosion products, and adherence to Italian guidelines for risk management and safety assessment in existing bridges. This comprehensive review sets the foundation for the subsequent analysis and findings presented in the thesis.

## 2.1. Non-Destructive Evaluation (NDE)

Internal post-tensioning systems are embedded in concrete box girders, making it difficult to inspect using NDE methods for assessing the condition of the internal tendons(Hurlebaus et al. 2016). However, some of the NDE techniques that have been used in the past for the inspection of internal tendons are discussed in the following section.

### 2.1.1. Electromagnetic Methods

Electromagnetic (EM) methods use charged particles that interact with the object of inspection through wave-like behavior. The frequency spectrum for EM methods ranges from the VHF-class (Very High Frequency, on the order of 109 Hz) used by ground penetrating radar to the gamma- class (greater than 1019 Hz) used by gamma-ray spectroscopy. The following is a summary of EM methods used for internal tendon systems.

- Ground Penetrating Radar (GPR)

GPR is a radar imaging technique that involves emitting electromagnetic pulses (typically on the order of 109 Hz) from an antenna and receiving the reflected pulses from internal reflectors. Reflections are caused by changes in the material's electrical conductivity and dielectric permittivity.

- GPR can identify the location and depth of reinforcement and internal tendons embedded in concrete decks or walls, yet mats of reinforcement that are below other reinforcement mats are difficult to detect. (Pollock et al. 2008)
- Concrete structures that are less than six months old still contain moisture that limits GPR. (Pollock et al. 2008)
- (Derobert, Aubagnac, and Abraham 2002) recommend using either ground coupled GPR as a primary NDE method to quickly obtain general information of a structure, such as layout and

depth of reinforcement and tendons, then following up with appropriate in-depth methods for additional testing. Inspection depth to approximately 10 in.

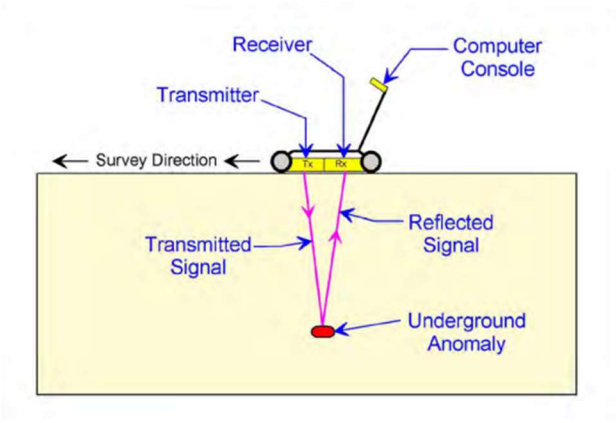


*Figure 1 GPR technology.*(Hutchinson and Teschke, n.d.)

- Infrared Thermography (IRT)

Infrared thermography is an imaging technique that translates thermal energy emissions that escape the surface under inspection to a temperature map. This is an extremely convenient NDE technique, as delamination and voids act as thermal barriers for heat released from concrete.

- conducting these tests can pose challenges due to the strong reliance of IRT devices on ambient temperature conditions. The most favorable outcomes are achieved during periods of the day characterized by the most rapid fluctuations in temperature.
- IRT devices are classifiable into two main types: active systems and passive systems.

- Passive IRT

Passive infrared systems are contactless technologies that rely on the heat of the sun and different times of the day when the surroundings are either warming or cooling to provide temperature gradients for thermal inspection. The voided area had to be directly between the heat source and the steel strands to be effectively identified. (Pollock et al. 2008)

- Active IRT

Active infrared systems distinguish themselves from passive systems solely based on how the heat source is utilized. In active IRT, a heater is employed to warm specific areas of the structure within a controlled environment. Active IRT could successfully and consistently locate air voids, but only in plastic ducts in thin specimens. (Pollock et al. 2008)

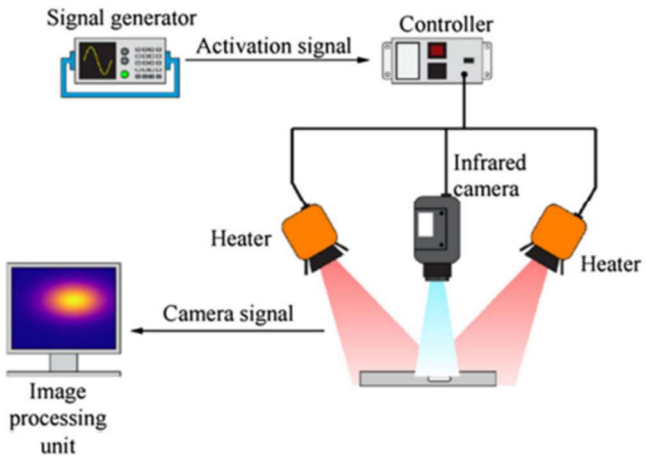


*Figure 2 Setup of infrared thermography (IRT)*(Siang et al. 2021)

### 2.1.2. Radiography

Radiography is a technique that assesses images of an object by projecting high energy beams of electromagnetic radiation (typically x-rays or gamma-rays). Both x-rays and gamma-rays can be used with multiple scan angles and computer processing and reconstruction techniques to display 2D images of a 3D object.

- X-ray Radiography.

  - The method is very time consuming, costly, and poses potential health risks for implementation.
  - X-ray scans noted inclusions, voids, and broken and cut strands within the internal ducts.

It should be noted that x-ray radiography only provides images of internal composition; therefore, it does not provide any information regarding the depth of defects. (Harris 2003)

- Gamma-ray Radiography

The gamma-ray radiography technique was applied to a PT box girder bridge in Portugal and was successful in assessing the grout condition and location of internal tendons.

- Gamma-ray radiography can detect and locate voids, and in some cases detect wire or strand fractures. (Derobert, Aubagnac, and Abraham 2002)
- This technique cannot detect corrosion and emphasized the impracticality of field inspection due to the cost of equipment, health hazards, and time required for a small testing location. (Derobert, Aubagnac, and Abraham 2002)
- It should be noted that it does not provide any information regarding the depth of defects.

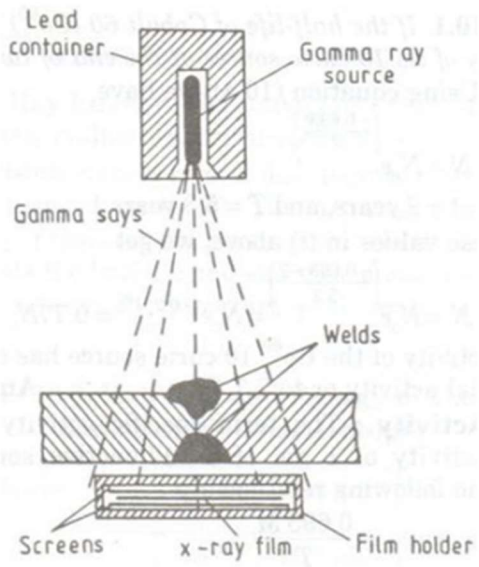


*Figure 3 Gamma-Ray Setup*

### 2.1.3. Magnetic Methods

Magnetic methods are promising techniques in the NDE field for locating steel section loss due to corrosion, strand/wire pitting, or breakage. (Azizinamini and Gull 2012) noted that active MFL was primarily useful for scanning specimens where large areas of corrosion were present, while residual MFL was better at determining small areas of corrosion.

- Active Magnetic Flux Leakage (MFL) Method

In the active MFL method, a ferrous material (steel) is subjected to a strong magnetic field by a portable magnet. This induces flux paths in the material between the two poles. At locations where there is a section loss, the magnetic field in the material "leaks" from its typical path of least resistance. A magnetic field detector between the poles of the magnet that is sensitive to this change in magnetic field indicates the leak.

- In a study performed by (DaSilva et al. 2009), MFL devices were able to detect corrosion (mimicked by both gaps and induced corrosion) levels of eight percent cross-section loss and up.
- (Harris 2003) reported that MFL was not able to detect flaws in PT tendons near anchorage zones, but this was primarily due to the magnets being too weak to saturate the tendons.

- Residual Magnetic Flux Leakage

In the residual method, the steel is brought to full magnetic saturation in order to erase its unknown magnetic history, then the magnet is removed, and the sensors are passed over the section for residual magnetic field measurements.

- (Hillemeier and Scheel 1998) described the successful use of residual MFL (sometimes referred to as remnant MFL) applied to prestressed and post-tensioned bridge beams, bridge slabs,
- Reports indicate that the device cannot detect ducts through layers of reinforcement. (Ghorbanpoor et al. 2000)

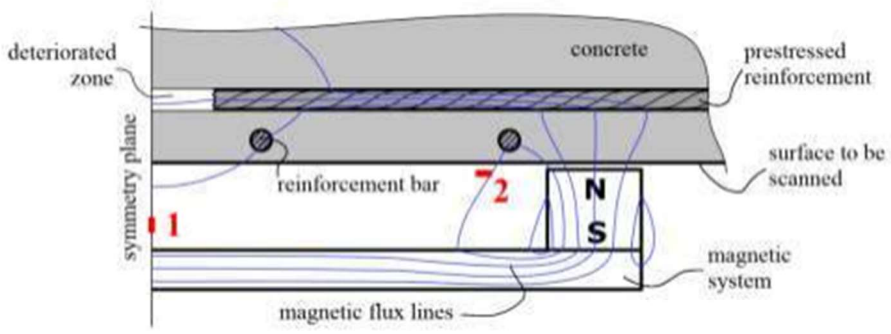


*Figure 4 Schematic of magnetic NDT* (Myakushev et al. 2018)

### 2.1.4. Mechanical Wave and Vibration Methods

NDE methods based on mechanical waves are one of the oldest methods used in any field. Below is a summary of each method and their use in the NDE of internal PT tendons.

➢ Acoustic Emission (AE)

The AE method is a passive NDE technique that allows continuous testing of a structure while in-service rather than at regular intervals. (Blitz and Simpson 1995). Acoustic emission is based on recording (in-situ) damage events (called acoustic emissions) from a structure. As damage occurs, whether it is cracking of the concrete or strands/wire embedded in tendons, data acquisition systems collect the events picked up by sensors attached or embedded in the structure.

➢ Impact Echo (IE)

The impact echo method uses a mechanical impact to generate stress pulses in the concrete. Because the impact generates a high energy pulse and can penetrate the concrete, the IE method is particularly promising for identifying defects in concrete structures (Celaya, Shokouhi, and Nazarian 2007)

- The IE method involves hitting the concrete surface with a small impactor or impulse hammer and identifying the reflected wave energy with a displacement or accelerometer receiver mounted on the surface near (within 50 mm, 2 in.) the impact point. Then the time domain test data are processed with a Fast Fourier Transform (FFT) which allows identification of frequency peaks (echoes).
- (Tinkey and Olson 2008) reported that the scanning system could not detect voids well when the diameter of the ducts was small, and the concrete cover was large. Also, the IE scanner system was incapable of identifying voids when the ducts were partially filled with water.

- (Harris 2003) reported that IE could detect large voids in grouted ducts with 60 percent accuracy The size of the voids could not be determined.
- The system evaluated voids in metallic ducts but failed to identify voids in plastic ducts.
- (Azizinamini and Gull 2012) noted that the IE method can be slow and challenging in the evaluation of anchorage zones or areas of complex geometries.

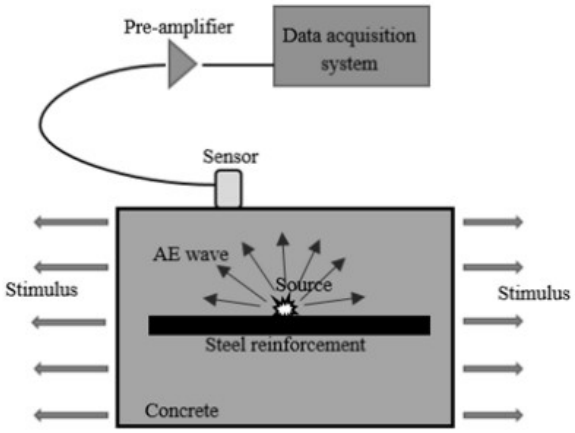


*Figure 5 Acoustic emission technique* (Zaki and Ibrahim 2021)

### 2.1.5. Ultrasonics (US)

The ultrasonic technique encompasses all methods that employ the use of acoustic waves over 20 kHz. The principle of operation is the same regardless of the type of US system: A sensor or a set of sensors releases a stress pulse into the specimen. As the waves travel through the material, areas with variations in impedance reflect parts of the wave, which are then detected by sensors. Through time-of-flight measurements and frequency/amplitude characteristics, defects and/or discontinuities can be determined.

- ultrasound may also be used to study components with high reinforcement density.
- The US technique has shown a promising future for detecting and locating internal defects in concrete structures, including concrete thickness, internal duct locations, material layers, reinforcement presence, elastic modulus, cracks, voids, delamination, and corrosion. (Im and Hurlebaus 2012)

➢ Pulse-Echo, Through-Transmission, and Linear Array

In the pulse-echo mode, US measurements are made with a single sensor or group of sensors that both emit a unified stress pulse and receive the reflected pulse after it has interacted with internal objects by the same sensor or group of sensors.

- In pulse echo technique, the measured values are the travel time of the pulse and the amplitude of the signal. Time and amplitude of the pulse can be illustrated in a time/amplitude diagram. This diagram is usually called A-scan.

- All the pulse echo tested techniques could detect the metal tendon location and thickness of the member accurately. (Krause et al. 2011)
- Another way of data evaluation is to analyze the phase information of the pulse. The cause of the change in the phase angle is dependent on the respective process method. During the transmission on an interface like concrete to steel for transverse waves (SH wave), phase of the reflected pulse remains the same as the phase of the pulse source. On the other hand, if the ultrasound pulse for transversal wave meets with an interface, like from concrete to air, it will change the phase angle. This effect can be used for the detection of un-grouted sections of the ducts.
- Although this technique yielded successful results for detecting voids in PT concrete beams, it is relatively time-consuming and costly because of the large number of transducers required. (Martin et al. 2001)
- A special automated imaging system, including linearly arrayed multiple transducers, was developed to considerably reduce the measurement time (Krause et al. 2011). It is capable of detecting delamination and voids (water- and air-filled) up to 36 in. and 8 in. in depth, respectively (Wimsatt et al. 2014).
- Although the automated scanning system is capable of identifying voids within the internal tendon system, it is difficult to directly assess the condition of strands. (Streicher et al. 2006)

➢ Ultrasonic Guided Waves (UGW)

The ultrasonic guided wave method is a technique in which complex combinations of wave modes propagate axially along a steel rod, tendon, or strand and are reflected at areas containing defects or section loss. The UGW method is applied at the free end of a tendon where the individual strands/wires are exposed.

- (Pavlakovic et al. 1997) discovered that the maximum inspection range for complete wire breaks was 47.2 in. for 0.28 in. diameter wires, and 31.5 in. for 0.2 in. diameter wires. For partial section loss or breaks, these distances are reduced significantly.

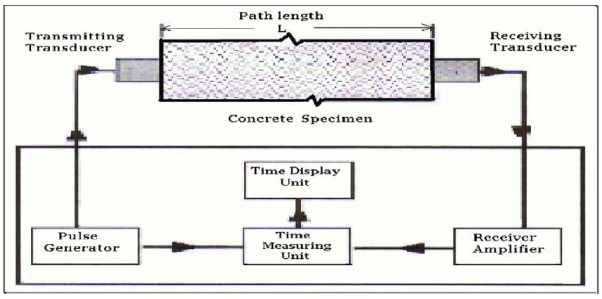


*Figure 6 Ultrasonic technique* (Jagannadha Rao 2018)

### 2.1.6. Visual Methods

Visual inspection is the most common and the most applied method of evaluation.

- In internal PT ducts, non-invasive visual inspection is virtually limited to inspection of the anchorage zone, of evaluation.

Borescope is an inspection technique used to explore anchorage zones or exposed internal ducts for voids and corrosion activity directly.

- A borescope consists of flexible optic fibers with a small eyepiece at one end.
- borescope require access holes.
- Borescopes can also have miniature video cameras attached at their ends to video record the inspection.

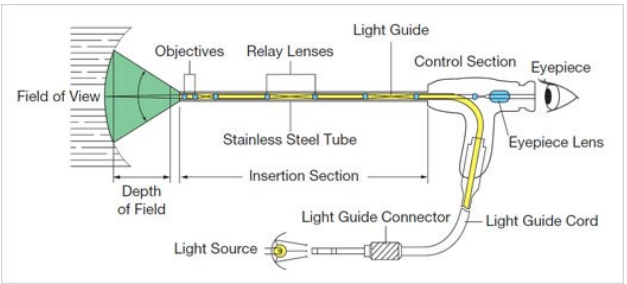


*Figure 7 Borescope technique.*

### 2.1.7. Electrochemical Methods

Electrochemical NDE methods are used to determine the electrochemical activity present in a structure. Most of these methods require additional information provided by visual inspection, chloride concentration, concrete resistivity, temperature, humidity, concrete type, bar coatings, duct type, and other factors.

- Half-cell Potential

The half-cell potential technique indicates the likelihood of corrosion by measuring the electrical potential difference between the steel reinforcement and a portable reference electrode. This method requires direct access to bars or strands.

- (Azizinamini and Gull 2012) note that this method may indicate corrosion activity, it certainly does not guarantee that corrosion damage is present, nor does it indicate the type of damage.
- The use of half-cell potential is typically limited to upper-layer reinforcement corrosion maps. The method has seen limited use for internal PT tendons, as it would only be useful for providing the likelihood of corrosion for the tendon as a whole and not the individual strands.

➢ Linear Polarization Resistance (LPR)

LPR provides an instantaneous measure of the rate of corrosion of steel embedded in concrete. This is achieved through potentiostatic means by inducing a potential change and observing the subsequent decay of the current, or through galvanostatic means by inducing a current change and observing the resulting decay of the potential. (Law, Millard, and Bungey 2000)

- A disadvantage of this method is its inability to differentiate between the various electrochemical processes involved in corrosion such as
  - resistance to charge transfer,
  - concentration polarization,
- This technique is also not wholly non-destructive as access to the steel is required for post-construction testing.

It should be noted that epoxy-coated or galvanized steel cannot be used with this method, and concrete cover must be less than 2 in. The concrete also needs to be smooth and uncracked.

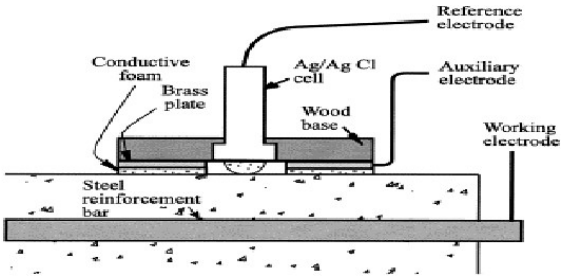


*Figure 8 linear polarization Resistance technique* (Velu 2007)

### 2.1.8. Sensor Methods

It is a special category of NDE systems developed for short- and long-term monitoring of structures.

➢ Time Domain Reflectometry (TDR)

TDR is a technique that utilizes an embedded probe alongside reinforcement or strands. As an electromagnetic pulse is sent to the probe, the material's relative dielectric constant influences the pulse velocity. By comparing the pulse travel time to the travel time in free space, the dielectric constant can be calculated. This in turn can be used to determine the changes in impedance or indication of strand discontinuity.

(W. Liu et al. 2001) explored TDR and reported that the method could detect, locate, and identify the extent of corrosion.

- Wireless sensors

In internal PT tendons, wireless technologies are quickly becoming viable options for impairment detection because internal ducts are difficult to access by other technologies.

The disadvantage of wireless sensors for internal PT tendon monitoring is that the structural components can only be monitored after device installation. Pre-existing damage is typically not detected.

- Fiber Optic Sensors

Fiber optic sensors use optical fibers (typically made of glass or plastic) as both intrinsic and extrinsic sensors to collect material quantities such as strain, temperature, moisture, and pressure by measuring the characteristics of light propagating through the fiber. The benefits of using these technologies are the sensors' small size, light weight, and immunity to electromagnetic interference and electrical noise.

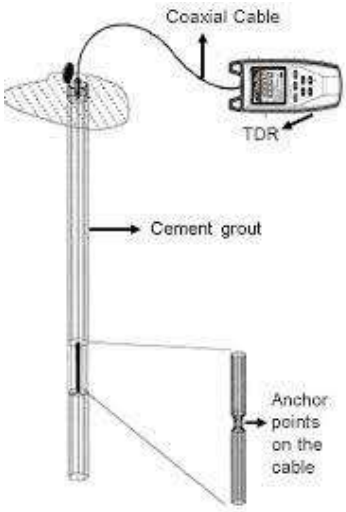


*Figure 9 Time Domain Reflectometry (TDR) technique* (Matos et al., n.d.)

### 2.1.9. Summary Table of all NDE methods

In this subsection, a comprehensive overview and analysis of various non-destructive evaluation (NDE) techniques were provided, highlighting their respective applications, operational domains, and inherent limitations. Subsequently, a concise summary table encapsulating the key characteristics of each method is presented.

| Method | Name | Use of | Works on | Limitation |
|---|---|---|---|---|
| **Electromagnetic Methods** | Ground Penetrating Radar | electromagnetic pulses | reinforcement location & depth | Preliminary survey |
| | Infrared Thermography | thermal energy emissions | Locating air voids in concrete | Works only on plastic or concrete ducts |
| **Radiography** | X-ray Radiography | X-ray electromagnetic radiation | voids & strand corrosion | time consuming, costly, health risk |
| | Gamma-ray Radiography. | Gamma-ray electromagnetic radiation | voids & strand corrosion | time consuming, costly, health risk |
| **Magnetic Methods** | Active Magnetic Flux Leakage | magnetic field | Strand corrosion | 8% cross-section loss and up. |
| | Residual Magnetic Flux Leakage | magnetic field | Strand corrosion | cannot detect ducts through layers of reinforcement |
| **Mechanical Methods** | Acoustic Emission (AE) | Sound Prints | Concrete & strand rapture | - |
| | Impact Echo (IE) | Mechanical stress pulses | defects in concrete | slow and challenging in anchorage zones |
| **Ultrasonics** | Pulse-Echo | Acoustic stress pulses | Voids & defects in concrete | time-consuming and costly |
| | Ultrasonic Guided Waves | Ultrasonic waves | Strand defects or section loss | - |
| **Visual Methods** | Borescope | - | Concrete voids & strand corrosion | limited to inspection of the anchorage zone |
| **Electrochemical Methods** | Half-cell Potential | electrical potential difference | Strand corrosion | does not guarantee corrosion damage |
| | Linear Polarization Resistance | electrical potential difference | Strand corrosion | not wholly non-destructive |
| **Sensor Methods** | Time Domain Reflectometry | electromagnetic pulse | Strand corrosion | - |
| | Wireless sensors | - | Strand corrosion | Pre-existing damage is typically not detected. |

*Table 1 NDE Methods for Internal post-tension bridges*

## 2.2. Failure categorization.

In accordance with the report conducted by (Menga, Kanstad, and Cantero 2022), the following descriptions outline the levels of damage and failures observed in post-tensioned structures.

The term “failure” is defined as a state where the performance level of a structure or a structural element is deemed inadequate (Menga, Kanstad, and Cantero 2022). The failures discussed are specifically associated with the corresponding structural damage.

The description of failures is organized based on three key factors, as highlighted by (Menga, Kanstad, and Cantero 2022): the timing of damage detection, the typology and suitability of interventions, and the resulting structural consequences.

- Timing of Damage Detection

  - **Early:** Damage that is identified during planned inspections, characterized by light severity such as small crack width, minimal spalling of the concrete cover, or minor tendon issues.
  - **Late:** Damage that has significantly affected parts of the prestressing system, indicating a delayed detection and intervention.
  - **Too Late:** Severe damage that has rendered the structure beyond repair, exemplified by wide cracks, extensive concrete cover spalling, or failed tendons.
  - **Not on Time**: Damage that was present, but went unnoticed, leading to irreversible consequences for the structure.

- Typology and Suitability of Interventions

  - **Ordinary:** Ordinary maintenance activities prove to be sufficient in restoring the structure to a safe condition.
  - **Extensive:** Extensive operations on the prestressing system, such as tendon substitution, are required due to the extent of the damage.
  - **Extraordinary:** Extraordinary interventions, including demolition, are necessary to address the damage.
  - **Inadequate or Absent:** The interventions carried out are inadequate compared to the severity of the damage or, in some cases, completely absent.

➢ Structural Consequences of Damage

- **Maintenance:** Moderate damage that can be repaired through ordinary maintenance activities.
- **Tendon Failure:** Damage that involves the breakage of tendons, potentially jeopardizing the overall safety of the structure. Extensive operations, such as tendon substitution, become necessary.
- **Demolition:** Severe damage that compromises the overall safety of the structure, necessitating demolition as an extraordinary intervention.
- **Collapse:** The structure experiences partial or total collapse due to inadequate or absent interventions, often resulting from the absence of warning signs.

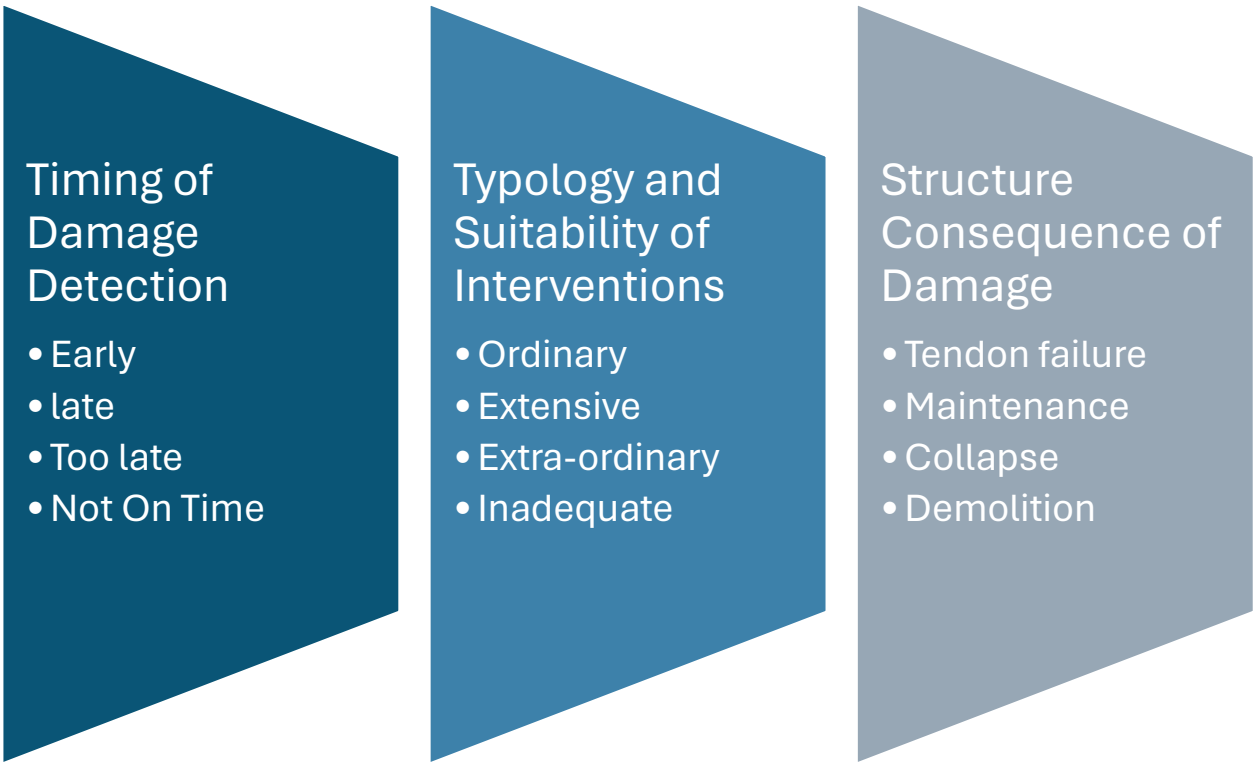


*Figure 10 Failure Categorization*

By categorizing failures based on the timing of damage detection, intervention typology, and resulting structural consequences, a comprehensive understanding of the implications of damage and the effectiveness of interventions can be gained. This information is essential for developing strategies to mitigate failures and improve the durability and safety of post-tensioned structures.

### 2.2.1. Failure Causes and Their Impact on Post-Tensioned Bridge.

Understanding the causes of failures in post-tensioned bridges is crucial for enhancing their design, construction, and maintenance practices. This section analyzes and discusses the major failure causes identified in the reported cases; performed by (Menga, Kanstad, and Cantero 2022); highlighting their impact on bridge performance and integrity.

➢ Major Failure Causes

Failures in post-tensioned bridges are typically the result of multiple factors that accumulate over time. The principal reasons for failure can be attributed to execution, conceptual design mistakes, grout problems, presence of cracks, use of inappropriate materials, and inadequate concrete cover.

➢ Influence of Failure Causes on Different Levels of Damage

To better comprehend how the identified causes contribute to failure, they are classified according to the level of damage observed in the bridges. The data presented in the following sections sheds light on the relationship between failure causes and specific types of damage.

- Collapses

Collapses in post-tensioned bridges are predominantly influenced by execution issues, conceptual design mistakes, use of inappropriate materials, and inadequate concrete cover. These factors were found to be significant contributors to structural failures, with execution-related problems being the most prevalent cause.

- Demolished Structures

Demolished structures exhibited similar issues as collapsed ones, with execution problems and conceptual design mistakes being primary factors. Additionally, the use of inappropriate materials and inadequate concrete cover were observed in some cases, further compromising the structural integrity.

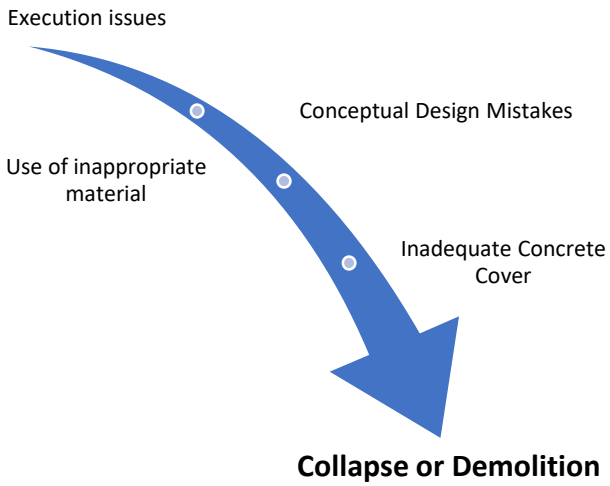


*Figure 11 Collapse and Demolition Causes*

- Tendon Failures

Failures of post-tensioning tendons were primarily caused by grouting problems, execution errors, conceptual design mistakes, presence of cracks, and use of inappropriate materials. Among these, grouting problems emerged as the most common cause of tendon failures, emphasizing the critical role of proper grouting practices.

- Damage at the Maintenance Level

Structures with damage categorized at the maintenance level are mainly attributed to conceptual design mistakes, execution issues, and the presence of cracks. These causes highlight the importance of addressing design flaws and ensuring proper construction practices to mitigate ongoing maintenance needs.

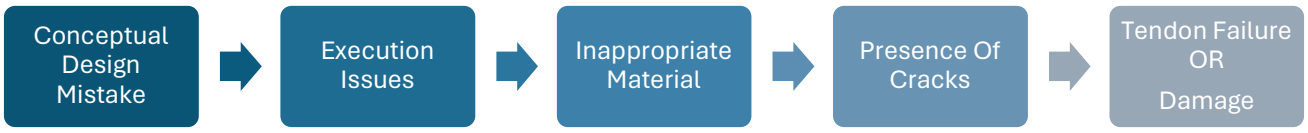

- Importance of Cracks in Failure Causes

Cracks were found to have significance in cases where monitoring and inspections were possible. While cracks can be induced by various factors, including shrinkage and thermal effects, their presence indicates potential weaknesses in design and execution. This further emphasizes that corrosion in post-tensioned bridges can result not only from planning and construction issues but also from events occurring during the structure's service life.

Understanding the major causes of failures in post-tensioned bridges provides valuable insights into improving design, construction, and maintenance practices. Effective execution, careful conceptual design, proper grouting, adequate concrete cover, and proactive crack management are critical factors in ensuring the long-term performance and durability of post-tensioned bridge structures.

### 2.2.2. Incorrect Tendon Layout Effect on The Structure Deflection

Prestressing plays a crucial role in deflection prediction, but its effectiveness in reducing deflections is heavily influenced by the layout arrangement of prestressing tendons. During construction, cantilever tendons are typically highly efficient. However, when structural modifications are made to create a continuous structural system, such as closing midspan joints, the long-term efficiency of cantilever tendons in minimizing deflections may be considerably reduced. This limitation arises due to the development of additional forces resulting from the redundancy in the new structural system. Hence, careful consideration of the layout arrangement of prestressing tendons and the potential effects of structural changes is essential for accurate deflection predictions in post-tensioned structures.

To understand better the effect of tendons on long term deflection the Highway (D8) bridge over the river Ohre was taken as a case study. It is a three-span continuous box girder bridge with tapered shape, erected using cantilever technology.

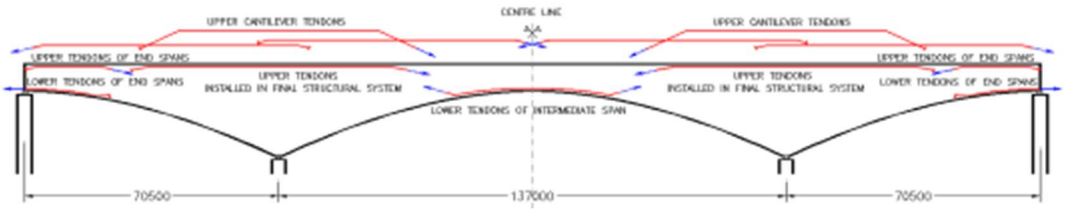


*Figure 12 Scheme of Layout of Prestressing Tendons*

In a research study conducted by (Vrablik, Matous, and Kristek 2013) on the bridge, it was observed that only the tendons positioned at the bottom surface of the first and third spans exhibited detrimental effects, leading to an increase in deflection within the central region of the main span of the bridge. Conversely, it was found that relocating the anchorages of tendons located on the top surface to the bottom surface of the box beam proved advantageous in reducing midspan deflection. This arrangement also offered significant benefits in minimizing shear forces near internal support. (Vrablik, Matous, and Kristek 2013).

### 2.2.3. Presence Of Warning Signs, Collapse, and Demolition

In the cases examined by (Menga, Kanstad, and Cantero 2022), several collapsed structures exhibited warning signs prior to their failure.

➢ Collapse

Several collapsed structures discussed in this report exhibited warning signs prior to their collapse, emphasizing the importance of proactive monitoring.

- Lowe's Motor Speedway:
  - Longitudinal cracks along the stem soffit at mid-span directly under the grout plug location.
  - Corrosion staining around the grout plugs in several beams.

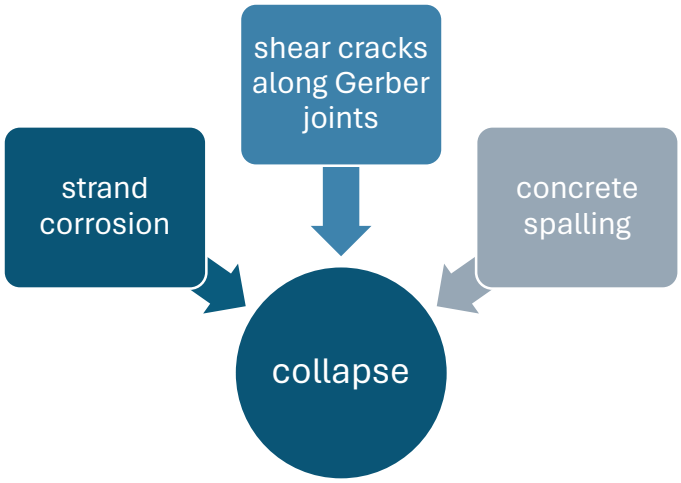


*Figure 13 Collapse warning signs*

- Polcevera Bridge:
  - Extensive strand corrosion.
  - Oxidation of the metallic duct.
  - Cables with loose strands.
- Annone Overpass:
  - High levels of corrosion.
  - Concrete spalling along the beams.
  - Presence of a shear crack at the Gerber joint.

These warning signs served as indicators of structural distress and played a significant role in the subsequent collapse of these bridges.

➢ Demolition

A structure is typically demolished when the severity and extent of the detected damage pose a significant threat to the overall safety of the structure, and the cost of repair measures surpasses the value of the structure itself. The following bridge cases exemplify such situations.

- Sorell Bridge:
  - Appearance of cracking along the web of the beams, following the path of the post-tensioning tendons, which left the tendons without concrete protection in some cases.
- Walnut Street Bridge:
  - Stains observed on the sides of the beams, indicating water seepage through the shear key joints between all beams.
- Other bridge cases:
  - Extensive corrosion of the post-tensioning tendons at the anchorages.
  - Cracks observed at diaphragm and joint locations.
  - Deterioration of concrete, including longitudinal cracks and spalling.

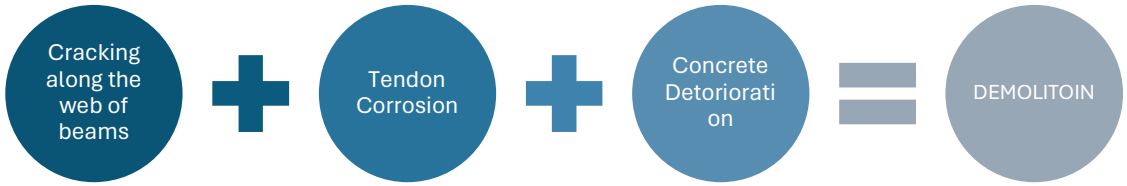


*Figure 14 Demolition warning signs*

In these instances, the detected damage reached a critical level where the safety of the structure could not be guaranteed, and the cost of repairing the extensive damage outweighed the value of preserving the structure.

➢ Tendon Failure

Tendon failures in post-tensioned systems are often preceded by certain warning signs. These signs include:

- Cracked ducts.
- Unplugged grout vents
- Extensive water leakage
- Cementitious grout efflorescence

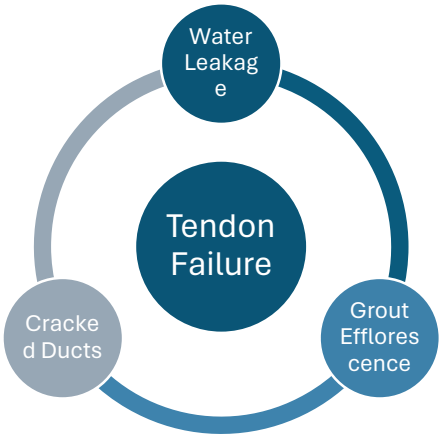


*Figure 15 Tendon Failure warning signs*

When one tendon is found broken, it is common to discover that other tendons in the same beam and/or adjacent beams have also experienced failures. Therefore, it is crucial to inspect the condition of the tendons not only in the affected beam but also in the surrounding beams when a failed tendon is detected. This comprehensive examination allows for a thorough assessment of the overall integrity of the post-tensioned system.

➢ Maintenance

Effective maintenance plays a vital role in ensuring the longevity and safety of structures. Early detection of warning signs enables timely intervention through maintenance activities. However, failure to carry out planned maintenance can lead to an escalation of damage levels.

These signs include:

- concrete cover spalling
- efflorescence
- cracks of various sizes
- rust stains.

The damage observed in internally post-tensioned bridges varied in severity, leading to different outcomes such as collapse, maintenance, and demolition. Warning signs were evident in half of the cases, including cracking along the beams following the path of post-tensioning tendons, signs of water penetration, cracking at diaphragms, corrosion staining, and concrete spalling. These warning signs highlight the importance of accurate design and execution, particularly in these specific locations within the superstructure.

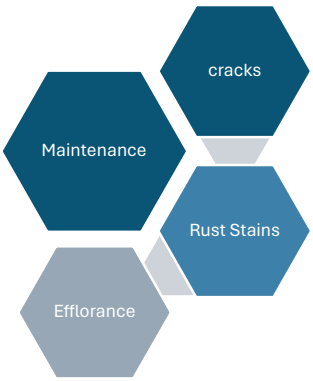


*Figure 16 Maintenance warning signs*

### 2.2.4. Failure Age

The findings of the research executed by (Menga, Kanstad, and Cantero 2022), indicate a correlation between the age of structures and the occurrence of failures. The following observations were made.

- The majority of failures tend to happen within the first 10 years of the structure's life.
- No failures have been reported for structures older than 60 years, except for the Williamsburg Bridge, which failed at the age of 79.
- Demolitions occurred between 10 and 50 years of age, with a concentration of cases between 30 and 40 years.
- Most tendon failures were observed within the first 20 years of the structures' life, with the majority occurring within the first 10 years.

These age-related patterns shed light on the vulnerability of post-tensioned structures at different stages of their lifespan (Menga et al. 2023).

### 2.2.5. Location of failures

According to the study executed by (Menga et al. 2023), the locations of failure in the investigated structures can be categorized into three main groups.

- Superstructure (19 out of 43 cases):
  - This category includes failures in the superstructure itself (4 cases), anchorages (1 case), beams (8 cases), and joints (6 cases).
- Tendons (20 out of 43 cases):
  - This category comprises failures in cable-stays (3 cases), external tendons (16 cases), and internal tendons (1 case).
- Miscellaneous (4 out of 43 cases):
  - This category includes failures in pillars (2 cases) and samples (2 cases).

These macro categories provide a framework for understanding the distribution of failures within the structures under investigation (Menga et al. 2023).

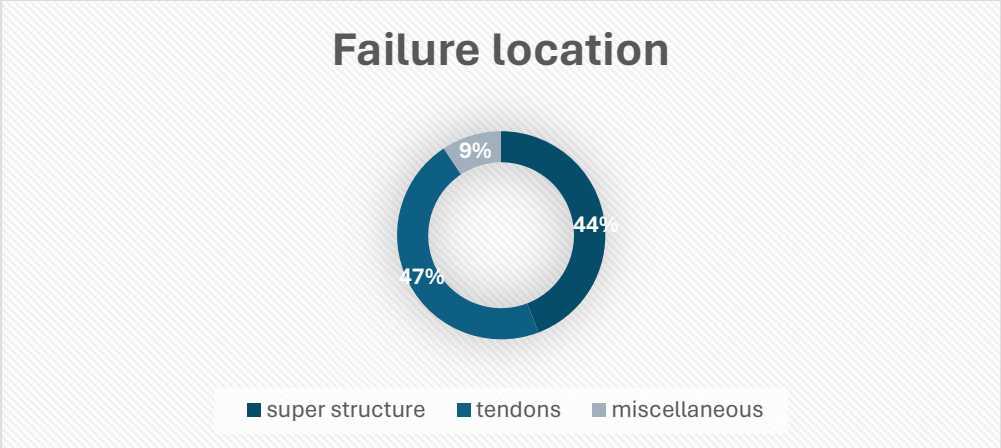


*Figure 17 Failure location according to* (Menga, Kanstad, and Cantero 2022)

➢ Superstructure (bridges)

Failures related to the superstructure primarily occurred at joints and deviation points, resulting in various types of damage (Menga et al. 2023)

- **Cracked diaphragms:** The diaphragms, which provide structural support and distribute loads, exhibited cracks.
- **Deteriorated concrete:** The concrete in the superstructure showed signs of deterioration, indicating a decrease in its overall strength and integrity.
- **Surface corrosion on anchorages and bearing plates:** Corrosion marks were observed on the anchorages and bearing plates, suggesting the presence of corrosive elements and potential weakening of the structural components.
- **Opening of joints:** Joints, intended to allow movement and accommodate structural changes, showed signs of opening or separation.
- **Severe concrete cracking:** Extensive cracking in the concrete was identified, indicating significant stress and potential structural instability.

*Figure 18 Joint damage*

➢ Tendons

Failures related to tendons in bridges exhibited distinct characteristics, indicating corrosion and damage to the tendon system (Menga et al. 2023)

- **Corroded and split tendons:** Failed tendons often displayed signs of corrosion and longitudinal or transverse splits in the polyethylene (PE) duct. In some cases, the tendons were completely ruptured and found lying at the bottom of the span. Additionally, tendon slippage from the ducts was observed in the failed section of the structure.
- **Evidence of strand corrosion:** Tendons showed indications of strand corrosion, manifested as localized pitting and breakdown of wires. These signs further confirmed the presence of corrosion-related damage within the tendon system.

These observations highlight the detrimental effects of corrosion on the integrity and performance of tendons in bridges, underlining the importance of monitoring and addressing corrosion-related issues to prevent structural failures (Menga et al. 2023).

Notably, tendon anchorages and deviation points are particularly susceptible to corrosion attacks as they represent critical points where the continuity of the structural element is compromised. These vulnerable areas emphasize the need to address corrosion-related issues to ensure the long-term integrity and safety of post-tensioned bridges (Menga, Kanstad, and Cantero 2022).

*Figure 19 Tendon corrosion*

The locations of failure and damage in post-tensioned bridges provide valuable insights into the vulnerabilities of these structures. Internally post-tensioned bridges were predominantly affected by damage in the superstructure, with 13 out of 19 cases exhibiting issues in this area. This damage occurred at joint locations, beams, anchorage locations, and other elements of the superstructure.

### 2.2.6. Corrosion Causes and Warning Signs

Corrosion is a significant factor contributing to the failure of post-tensioned bridges. This subsection examines the major corrosion causes identified in the reported cases by (Menga et al. 2023) and highlights the warning signs associated with corrosion-induced failures.

- Major Corrosion Causes

Corrosion causes creates the conditions for corrosion to occur, while failure causes contribute to the overall failure of the structure. Among the corrosion causes, the presence of external chlorides is the most frequent cause. It is important to note that problems in the grout, is the second most frequent cause. The majority of structures in (Menga et al. 2023) report experienced corrosion-induced failure due to external chloride penetration and grouting issues.

*Figure 20 Corrosion in Tendons*

- Sources of External Chlorides

External chlorides can enter the concrete from various sources, including de-icing road salts, which are a major contributor in cold climates, and seawater, whether in liquid or air-form state.

- Corrosion Warning Signs

In failures caused by external chlorides, it is evident that chlorides penetrated the concrete primarily through cracks or at joint locations. Several warning signs were observed, providing indications of potential corrosion-related issues, including:

  - Mild general or severe localized corrosion
  - Reduction in prestress and/or tendon cross-section
  - Presence of cracks and efflorescence
  - Concrete spalling and/or delamination

Detecting warning signs can aid in identifying potential corrosion-related issues and guide appropriate maintenance and repair strategies.

*Figure 21 Concrete spalling due to corrosion*

- Voids in Ducts and Tendon Corrosion:

When voids exist in the ducts, tendons are surrounded by air instead of grout, creating a favorable environment for corrosion initiation. Once chlorides penetrate the duct, they react with the air and trigger corrosion of the tendons. Notably, even if voids are subsequently filled with grout, actively corroding tendons can continue to corrode. It is essential to recognize that the penetration of chlorides into the concrete takes time. Therefore, in short-term failures, particularly in structures less than 10 years old, where external chlorides are the major corrosion cause, the combination of other failure causes may contribute to the overall failure.

*Figure 22 Voids in Ducts*

- Grouting Issues and Tendon Failures:

The integrity of grout plays a fundamental role in protecting post-tensioned tendons from corrosion. Problems in the grout, such as bleeding and segregation, are identified as the primary corrosion cause for tendon failures (Carsana and Bertolini 2015). Corrosion, often in the form of pitting, occurs in segments of the tendon where visible segregation of the grout or partial and full-depth voids are present. The unhardened grout exhibits a white, soft, and chalky appearance. Despite the absence of significant

chloride or sulfate infiltration into the ducts, corrosion can take place. It is worth noting that no corrosion attacks are usually found in areas where the tendons are embedded in regular hardened cement grout.

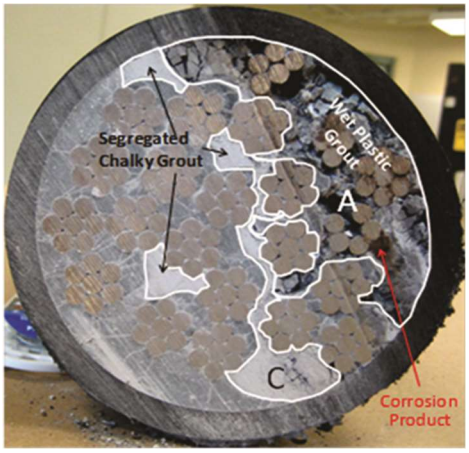


*Figure 23 Grouting Deficiencies*

Recognizing the significance of these factors is crucial for implementing appropriate measures to prevent and mitigate corrosion in post-tensioned bridges. Ensuring proper grouting techniques and addressing voids in ducts are essential for preserving the integrity and durability of the tendon system.

### 2.2.7. Corrosion products

The corrosion of steel within concrete is predominantly triggered by a chemical reaction involving iron ions, water, and oxygen. In the context of reinforcement corrosion, an extensive review study has identified two primary factors contributing to this phenomenon: internal and external. Internal factors mainly revolve around the environmental conditions prevailing within the concrete surrounding the steel reinforcement, such as the presence of oxygen, relative humidity, temperature, carbonation levels, and exposure to acidic gaseous pollutants and chloride ions. The interplay of these factors can lead to a decrease in the pH level and instigate chemical reactions that ultimately result in corrosion. On the other hand, external factors are tied to the quality aspects of both the concrete and steel components, encompassing various parameters such as the cement content, usage of admixtures, curing methods, presence of chloride salts in aggregates, water-to-cement ratio, chemical composition of the materials, and the structural characteristics of the reinforcing steel.

- Corrosion inspection and section loss

The pit depth gauge presents a more convenient and efficient alternative to microscopic and metallographic techniques when conducting field inspections. This gauge employs a needle that penetrates from the base plate's center to the corroded surface of a wire, enabling precise measurement of the distance from the base plate to the needle's tip. This approach offers a faster and simpler way to assess pit depths. Evaluating section loss based on pit configuration involves utilizing specific formulas corresponding to different pit types (Jeon et al. 2019).

- $A_{sl1} = 2r^2(\theta_1 - sin\theta_1 cos\theta_1)\ for\ 0 \le dp\ \le 2r$
  - $\theta_1 = \arccos\left(1 - \frac{d_p}{2r}\right)$
- $A_{sl2} = 2r^2(2\theta_2 - sin\theta_2 cos\theta_2)\ for\ 0 \le dp\ \le 2r$
  - $\theta_2 = \arccos\left(-\frac{d_p}{2r}\right)$
- $A_{sl}\ = 2r^2(\theta_3 - sin\theta_3 cos\theta_3)\ for\ 0 \le dp\ \le 2r$
  - $\theta_3 = \arccos\left(1 - \frac{d_p}{r}\right)$

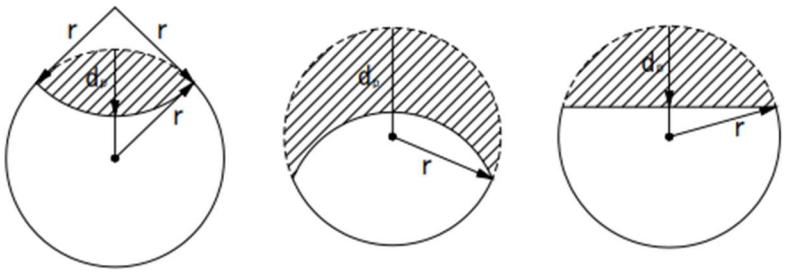


*Figure 24 pitting type* (Jeon et al. 2019)

- r is the radius of a wire
- dp is the pit depth measured by depth gauge at the deepest location.

For the quantitative comparison of corrosion, the extent of section loss, denoted as ∩, was expressed as follows:

$$\cap = A_{sl}/A_0$$

where $A_0$ is the sectional area of a wire, and Asl is the loss of sectional area.

➢ Stress–strain relation of corroded wires derived from analysis.

equations derived from regression analysis to define the ultimate state properties.

- $f_{u,c} = a \cap + \beta$
- $\varepsilon_{u,c} = \begin{cases} (c \cap^2 + d_\cap + e) & for\ d_p \le 0.5 \\ f_n g & for\ d_p \ge 0.5 \end{cases}$
- $f_{y,c} = 0.85\, f_{u,c}$
- $\varepsilon_{y,c} = 0.85 * f_{u,c}/E_s$

- $\sigma_w(\varepsilon) = \begin{cases} E_s * \varepsilon & for\ \varepsilon \leq \varepsilon_{y,c} \\ 0.85f_{u,c} + \frac{\varepsilon - \varepsilon_{y,c}}{\varepsilon_{u,c} - S_{y,c}} 0.15f_{u,c} & for\ \varepsilon_{y,c} < \varepsilon \leq \varepsilon_{u,c} \end{cases}$
- $\sigma_S(\varepsilon) = \sum_{I=1}^{N}(\sigma_{w,i}(\varepsilon) * A_{0,i}) / \sum_{I=1}^{N}(A_{0,i})$

❖ Ultimate Stress and Strain of Corroded Strand:
- $f_{u,c}$ : Represents the ultimate stress of the corroded strand.
- $\varepsilon_{u,c}$ : Denotes the ultimate strain of the corroded strand.
- ∩: Refers to the section loss.

❖ Coefficients from Regression Analysis:
- Coefficients a, b, c, d, e, f, and g: These coefficients are derived from regression analysis, considering various pit configurations.

❖ Yield Stress and Strain of Corroded Wire:
- $f_{y,c}$ : Represents the yield stress of the corroded wire.
- $\varepsilon_{y,c}$ : Denotes the yield strain of the corroded wire.

❖ Elastic Modulus of the Strand:
- Es: Refers to the elastic modulus of the strand, which is an important parameter in determining its mechanical properties.

❖ stress–strain relation of a corroded wire.
- $\sigma_w(\varepsilon)$ : is the stress of a wire with respect to $\varepsilon$.
- $\sigma_S(\varepsilon)$ : is the stress of a strand with respect to ε.
- $\sigma_{w,i}(\varepsilon)$ : is the stress of an I$^{th}$ wire making up the strand.
- $A_{0,i}$ is the cross-sectional area of the I$^{th}$ wire.

### ➢ Corroded Strand Behavior and Failure Mechanisms

In a study conducted by (Jeon, Nguyen, and Shim 2020), the tensile strength and ductility of corroded strands were investigated. The findings revealed distinct behavior between strands with little or no corrosion and those with corrosion. Strands without significant corrosion experienced simultaneous failures, with all wires fracturing simultaneously. However, in corroded strands, the most corroded wire fractured earlier than the others, resulting in an abrupt decrease in the overall strength. Nevertheless, the remaining wires continued to carry the load until the next wire fractured. Notably, there was a reduction in load between the first and second fractures, amounting to approximately 1/7 of the ultimate strength of the corroded strand ($f_{pu}$). This suggests that the load was distributed evenly among the seven wires, with the most corroded wire failing first. Consequently, the study defined the failure event of the strand as the moment when at least one wire fractured, and the corresponding strength and strain values were used to determine the ultimate strength and strain. This approach accounted for the fact that even if one wire yielded first due to cross-sectional loss, the remaining wires continued to bear the load until they reached their yield point.

The study conducted investigated the tensile strength and ductility of corroded strands, revealing intriguing findings. Despite a significant section loss of 22.52% in the most corroded specimen, there was no substantial difference in the observed yield strength. However, the ultimate strain of the wire was more severely impacted, with a mere 5% section loss resulting in an 85% maximum reduction in deformation capacity.

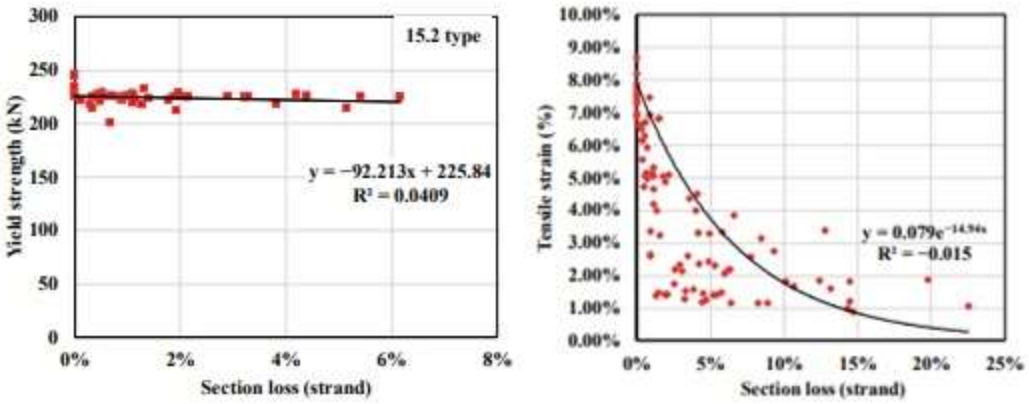


*Figure 25 Yielding & Ultimate Strength with Respect to Cross-sectional Area*

The approximate value of $f_{ps}$, which refers to the stress of the strand at the moment of the beam's failure, can be obtained through the following equation.

- $f_{c,ps} = f_{c,pu}\left[1 - \frac{\gamma_p}{\beta_1}\left\{\rho_{c.p}\frac{f_{c,pu}}{f_{ck}} + \frac{d}{d_p}(\omega - \omega')\right\}\right]$

❖ $f_{c,ps}$ : is the stress of the corroded prestressing strand when the beam fails.

❖ $f_{c,pu}$ : is the ultimate stress of the corroded prestressing strand.

❖ $\gamma_p$ is a coefficient according to the type of strand.

❖ $\gamma_p = \begin{cases} 0.55\ when\ {f_{py}}/{f_{pu}} \geq 0.80 \\ 0.40\ when\ {f_{py}}/{f_{pu}} \geq 0.85 \\ 0.28\ when\ {f_{py}}/{f_{pu}} \geq 0.90 \end{cases}$

❖ $\beta_1 = {a}/{c}$ ratio between the depth of an equivalent rectangular concrete stress block and the neutral axis depth

❖ $\rho_{c,p} = {A_{c,p}}/{bd_p}$ corroded prestressing steel ratio.

❖ $d$: depth of tensile reinforcement.

❖ $d_p$: depth of prestressing strand.

❖ $\omega = \rho\frac{f_y}{f_{ck}}, \rho = \frac{A_s}{bd}$ tensile reinforcement index

❖ $\omega' = \rho'\frac{f_y}{f_{ck}}, \rho' = \frac{A_{s\prime}}{bd}$ compression reinforcement index

- corrosion-induced cracking

The corrosion products generated from the degradation of the strand have a greater volume than the iron consumed, leading to corrosion expansion. As the corrosion proceeds, some of these products fill in pores and cracks, while others contribute to the pressure exerted by expansion. According to the constant volume principle, the overall volume of corrosion products in the strand, denoted as $\Delta V_r$, can be mathematically expressed.

$$\Delta V_r = \Delta V_w + \Delta V_c + \Delta V_p$$

Where $\Delta V_r = n\Delta V_w$, n is the strand rust-expansion ratio; $\Delta V_w$ is the volume change of wires; $\Delta V_c$ is the volume change of concrete induced by expansive pressure; $\Delta V_p$ is the volume of corrosion products that fill cracks and pores.

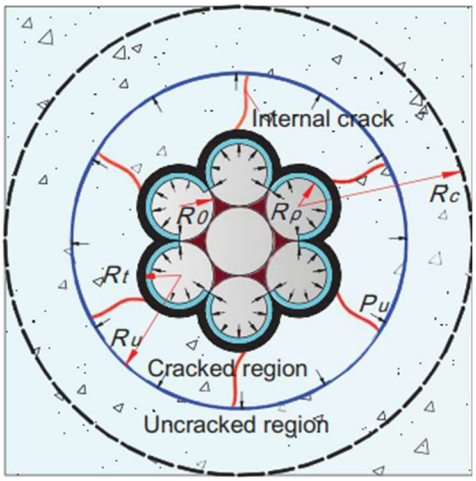


*Figure 26 concrete cracking due to strand corrosion.* (Wang et al. 2019)

### 2.2.8. Italian guidelines on risk management & safety assessment for existing bridges

The existing technical code provisions in Italy primarily concentrate on buildings, with the commentary offering minimal guidance on the seismic safety assessment of existing bridges, while neglecting assessments under service loads. In order to develop standardized evaluation protocols for existing bridges, both at regional and individual levels, the Superior Council of Public Works, a division of the Ministry of Infrastructure, released the "Guidelines on risk classification and management, safety assessment, and monitoring of existing bridges." These guidelines have been officially endorsed as a technical code by Decree No. 578 of the Ministry of Infrastructure. (17 December 2020). The approach adopted by the Guidelines tackles the challenges posed by existing bridges through a multilevel procedure, beginning with regional-scale risk evaluations based on qualitative assessments of bridges. The process then proceeds to define rules for detailed assessment procedures, providing a comprehensive framework for assessing the safety and risk of existing bridges in a consistent and standardized manner.(Santarsiero et al. 2021)

- Methodology of the Guidelines

The methodology outlined in the Guidelines for typical bridge structures involves a thorough analysis comprising five levels (0 to 4). For bridges of critical significance, an additional level (5) is introduced, which addresses network resilience aspects. The initial three levels (0 to 2) primarily focus on risk classification and management. In level 0, data is gathered from design documentation and routine inspections. Level 1 entails on-site inspections to assess the current state of deterioration and detect any notable defects affecting both structural and non-structural elements. Building upon the findings from levels 0 and 1, level 2 utilizes a procedure to determine the level of attention required for four risk categories: structure-foundation, seismic activity, flooding, and landslides. A qualitative risk assessment is conducted, taking into account hazard, vulnerability, and exposure factors.

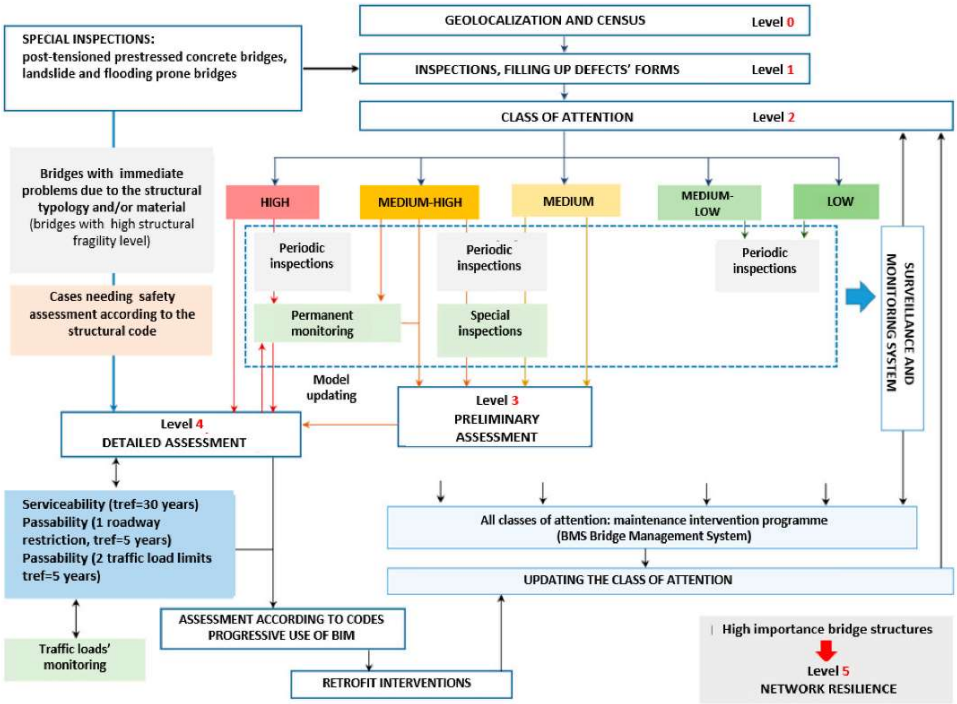


*Figure 27 Mapping the Layers: A Comprehensive Multi-Level Analysis.*(Santarsiero et al. 2021)

By amalgamating the outcomes of the individual levels of attention, a comprehensive level of attention is allocated to each bridge, placing them into five risk categories ranging from low to high: low, medium-low, medium, medium-high, and high. Based on this classification, the bridge owner is required to implement appropriate measures. Bridges with a medium-low or low class of attention can maintain serviceability with routine periodic inspections. However, for other cases, more comprehensive safety evaluations are necessary to decide on potential traffic load reduction measures or retrofit interventions. The methodology provides a systematic approach for bridge risk assessment and enables informed decision-making to ensure the safety and integrity of the bridge network.

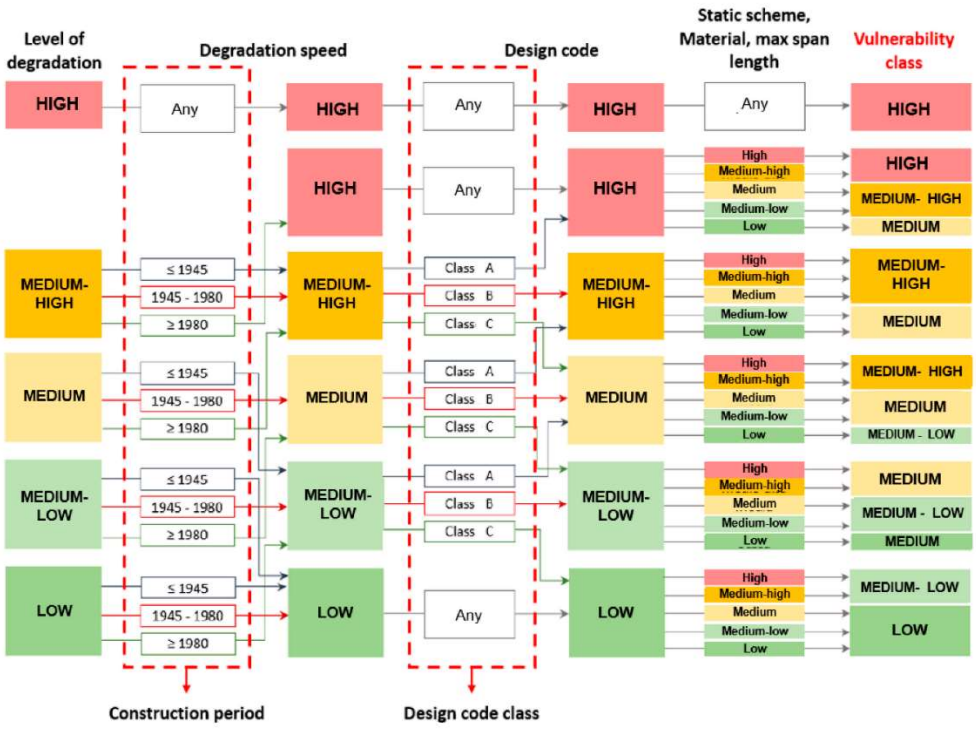


*Figure 28 Step-by-Step: A Logical Guide to Assessing Vulnerability Class*(Santarsiero et al. 2021)

## 2.3. Conclusion of the Second Chapter (Literature Review)

In summary, this segment of the master's thesis has delved into the intricate realm of Non-Destructive Evaluation (NDE) methods and the categorization of failures within post-tensioned bridges. By thoroughly examining various NDE techniques, including electromagnetic, radiography, magnetic, mechanical wave and vibration, ultrasonics, visual, electrochemical, and sensor methods, alongside a detailed analysis of failure modes and their implications on bridge structures, a comprehensive understanding of bridge assessment and management has been achieved. This exploration has shed light on the principles, applications, and limitations of NDE methods, as well as the identification and assessment of failure causes, warning signs, and corrosion-related challenges. Furthermore, the incorporation of established guidelines, such as the Italian guidelines on risk management and safety assessment for existing bridges, serves as a valuable framework for effective bridge maintenance and safety protocols. In essence, this thorough review contributes significantly to the field of bridge engineering, offering valuable insights and paving the way for future research and practical implementations aimed at ensuring the longevity and safety of post-tensioned bridge structures.

# 3. Polcevera Bridge

Most collapses of bridges occur while they are in-service, functioning under their normal operational conditions. The collapse of Morandi's Polcevera viaduct falls within this category. Many of the failed bridges were built during the mid-twentieth century and remained in service for 40 years or more before experiencing failure. These bridges exhibited compromised health conditions, displaying indications of corrosion, fatigue cracks, and, in some instances, concealed design flaws. Lacking redundancy and often containing fracture-critical elements, the failure of these bridges had the potential to result in partial or complete collapse. Over the past few decades, with population growth and the global economy's expansion, these failed bridges faced a continuous increase in traffic volume and heavy axle weights. Unfortunately, these bridges did not receive consistent maintenance, and their condition was not regularly evaluated. In most countries, bridges are typically designed with a service life of 75 years. The Polcevera bridge, one of its three pylons, underwent repairs in 1992, during which corroded cables were replaced with new ones. However, the remaining pylons did not undergo similar repairs, leading to the failure of one of them and causing the partial collapse of the bridge. (Morgese et al. 2020)

*Figure 29 polcevera bridge prior to collapse*

## 3.1. Description of the Polcevera Viaduct

The viaduct is composed of three cable-stayed systems, each supporting a three-span continuous beam with two sets of prestressed concrete cables positioned on either side of the pylon. These cables traverse over saddles on both sides of the pylon to reach the opposite side of the continuous beam. Buffer beams with Gerber saddles connect the three sets of continuous beams. The bridge deck is constructed from a partially prestressed concrete slab. The pylons are designed in a double V shape, with one V supporting the deck beam and the other (upside-down V) supporting the stays over the saddle. However, the design of cable stays at Morandi Bridge deviates from the norm, featuring only two stays per pylon. This, coupled with the saddle seats and the use of prestressed concrete tendons rather than steel cables, introduces a vulnerability in the bridge's structural integrity. if one cable fail, the bridge cannot remain intact. Additionally, the inspection of prestressed concrete tendons is challenging, and the corrosive effects of

the Mediterranean air and airborne pollution from steel mills contribute to the deterioration of the resistance of the concrete's chemical, leading to corrosion problems.

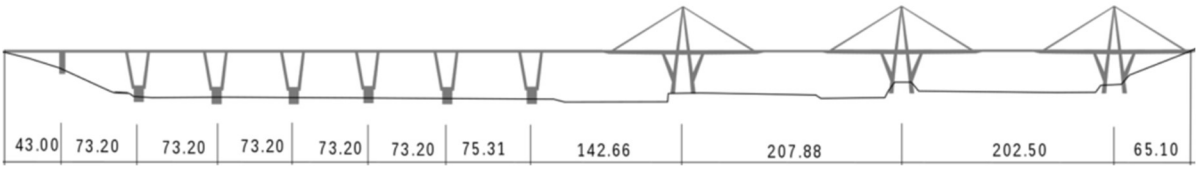


*Figure 30 Polcevera bride structural scheme*

During phase 4 of the operations, the original plan to inject grout into the ducts was unsuccessful, leaving many segments incompletely filled with grout materials. Subsequently, in the official investigation conducted by the ministry of infrastructure and transportation in 2018, the deficiency of grout in the tendon ducts was identified as the primary cause of pitting corrosion in the steel tendons. Pitting corrosion, discovered during the post-collapse inspection of the cables of Polcevera Bridge, manifests as localized holes and cavities in the steel tendons, posing a more destructive force than uniform corrosion and resulting in reduced load-bearing capacity, particularly under repeated loads. Its local occurrence makes pitting corrosion challenging to detect, exposing the cables to high levels of stress concentration.

*Figure 31 Polcevera bridge after collapse*

## 3.2. Discussions and Findings

Despite the hypothesis suggesting the combination of fatigue and corrosion of the cable stays as the main factor leading to the partial collapse of the bridge, the study's results indicated that the collapse of the bridge should have occurred approximately 2 to 4 years before the actual collapse date in 2018. The analysis utilized a limited amount of information about the corrosion-fatigue models available in the technical literature. Surprisingly, the results demonstrated that even without an active instrumented structural health monitoring system, basic engineering principles could provide a basis for estimating the remaining life of infrastructure. (Morgese et al. 2020)

# 4. Case Study Analysis

*Figure 32 case study Bridge*

## 4.1. Initiating the Case Study: Overview and Addressing the Challenge

In the context of prestressed segmental bridges, the assessment of serviceability is of paramount importance to guarantee their long-term performance and functionality. Unlike safety evaluations that focus on ultimate load capacities, serviceability considerations delve into predicting the evolving stresses and deformations under varying load conditions. Prestressed segmental bridges, constructed incrementally and composed of precast prestressed concrete segments, introduce unique challenges due to the dynamic interplay of time-dependent effects. Creep, shrinkage of concrete, and relaxation of prestressed steel contribute to continuous variations in stresses and deformations. As each segment is added, the structure undergoes changes in stiffness and internal forces, necessitating a meticulous analysis of the prestress loss over time. This time-dependent phenomenon, often overlooked, significantly influences both prestressed and non-prestressed steel within the structure. Hence, when evaluating the state of prestressed segmental bridges, a thorough assessment of serviceability becomes imperative to ensure sustained functionality, durability, and structural integrity over their operational lifespan.

- location of the Case Study

The case study bridge, completed in November 1992, is located in northern Italy. This road viaduct is a vital link connecting Italy, with France. Moreover, it forms an integral part of the European route E70, a major corridor running from La Coruna in Spain to Trabzon in Turkey, crossing from west to east. The completion of the bridge represented a remarkable feat in modern engineering and transportation advancement, facilitating enhanced connectivity between Italy and France.

*Figure 33 satellite photo of the bridge*

## 4.2. Structural Review

The post-tensioned bridge consists of two separate bridges, each accommodating two lanes, with individual piers. The bridge was executed using the free cantilevered scheme and is composed of five spans, stretching over a length of 320 meters. This modern and innovative structure is a 'Box Segmental Girder' bridge, featuring precast concrete girders with a hollow box-like cross-section, divided into smaller segments. Its design ensures structural efficiency, high torsional stiffness, and superior resistance to bending moments and shear forces, making it ideal for long-span applications. The 'Box Segmental Girder' construction method offers versatility, reduced construction time, and the ability to address complex geometries and site-specific challenges effectively.

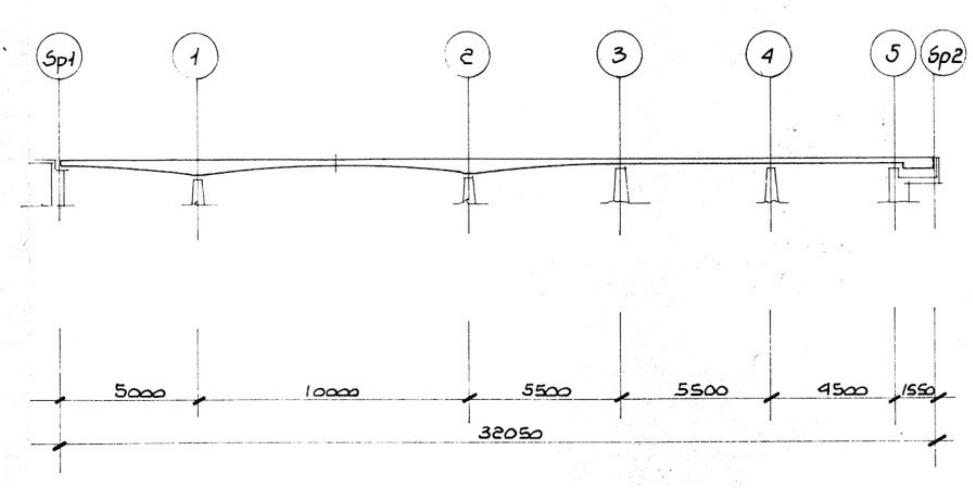


*Figure 34 layout of the bridge spans*

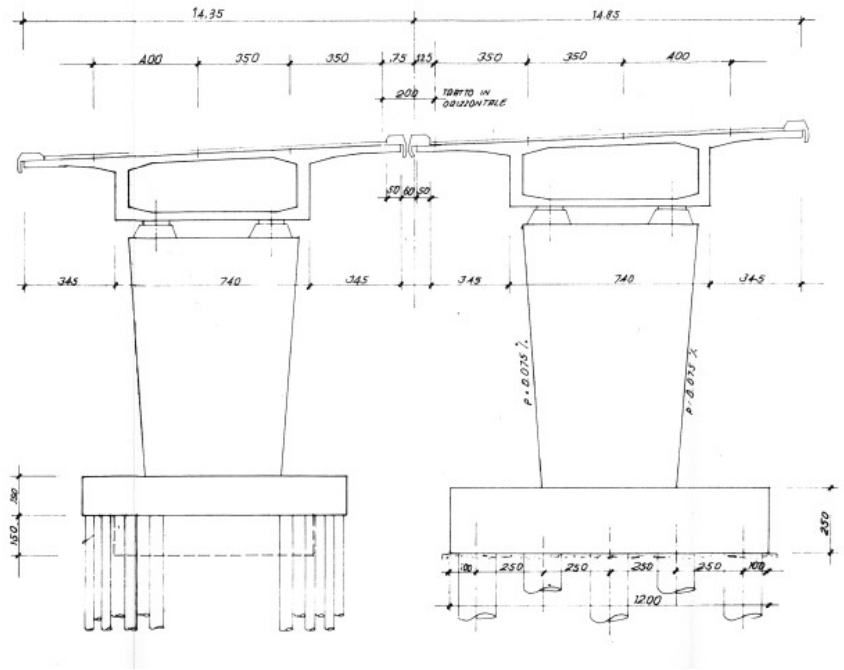


*Figure 35 cross section layout of the bridge*

## 4.2.1. Defining the Geometrical Properties of the Structure

- Girders properties
    - 1st span (sp1 & 1st piers):

The 1st span is 50 meters long with a varying segmental depth ranging from 245cm to 455cm. It consists of 18 consecutive segments of variable lengths, covering dimensions from 180cm to 305cm. The bridge's post-tensioning system includes 56 upper tendons that start at pier 1 and cross towards both sides, reaching abutment sp1 and pier 2. Additionally, there are 12 bottom tendons that start at abutment sp1 and traverse towards the first pier.

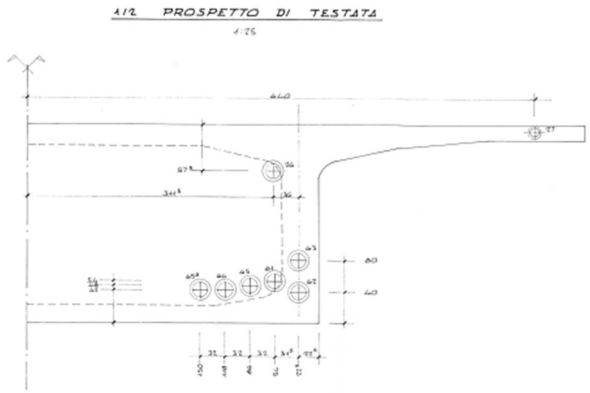


*Figure 36 section and layout of tendons at abutment sp1*

- 2nd span (1st & 2nd piers):

A 100-meter-long span features a varying depth, with measurements of 435 cm at the extremities and 245 cm at midspan. It comprises 35 consecutive parts, including 5 parts at each extremity measuring 260 cm long, 29 parts of length 305 cm, and one lock part of 70 cm long. The bridge's post-tensioning system consists of upper tendons, totaling 56 in number, which originate in the 1st span and extend to the midpoint of the 2nd span. Additionally, 26 bottom tendons start at the midspan between piers 1 and 2 and traverse towards the piers.

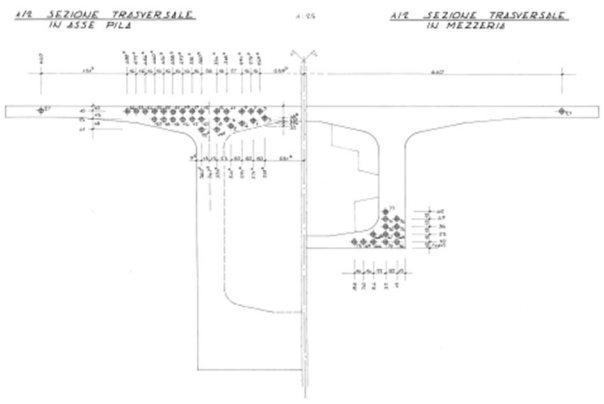

*Figure 37 section and layout of tendons between peer 1 & 2*

- 3rd span (2nd & 3rd piers):

The 55-meter-long span features a varying depth, with a measurement of 435cm at (pier 2) and gradually decreasing to 245cm at pier 3. It consists of 19 consecutive segments, with lengths ranging from 260cm to 305cm. The bridge's post-tensioning system comprises upper tendons, with 56 tendons starting in the second half of span 2 and continuing into span 3. Additionally, there are 24 additional upper tendons that traverse towards the midspan, originating from the 3rd pier. Moreover, 8 bottom tendons start at the 3rd pier and traverse towards the midspan.

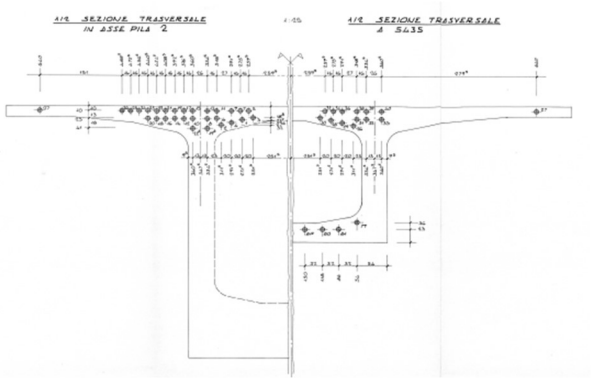

*Figure 38 section and layout of tendons between peer 2 & 3*

- 4th span (3rd & 4th pier):

The 55-meter-long span maintains a constant depth of 245 cm throughout its length. Comprising 20 consecutive segments, the bridge includes 15 segments with a uniform length of 305 cm, one starting segment measuring 235 cm, and two ending segments with lengths of 260 cm and 235 cm, respectively. Additionally, there is one middle segment acting as a lock, spanning 65 cm. The bridge's post-tensioning system consists of upper tendons, with 24 tendons originating in span 3 and continuing into span 4.

Furthermore, 28 additional upper tendons traverse towards the midspan from pier 4. Moreover, 20 bottom tendons initiate at the midspan between piers 3 & 4, traversing towards the piers.

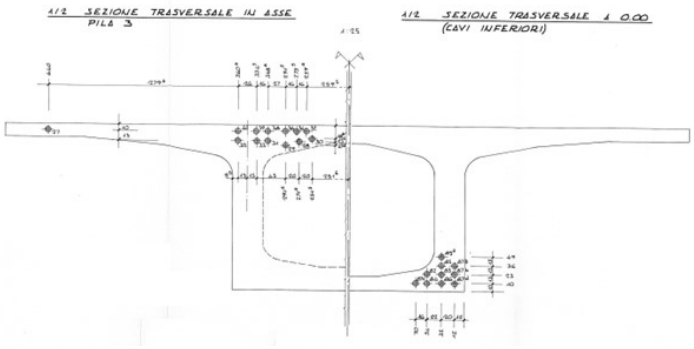


*Figure 39 section and layout of tendons between peer 3 & 4*

- 5th span (4th & 5th peer):

The 45-meter-long span features a constant depth of 245 cm across its length. It consists of 19 consecutive segments, with 15 segments having a uniform length of 305 cm. Additionally, there are 2 starting segments measuring 260 cm and 235 cm, respectively, 5 ending segments of 260 cm, and one final part of 240 cm. The span includes one middle segment acting as a lock, spanning 80 cm. The post-tensioning system of the bridge comprises upper tendons, with 28 tendons originating in span 4 and continuing into span 5. Additionally, 14 upper tendons start at abutment sp2 and traverse towards the midspan of span 5. Moreover, 16 bottom tendons initiate at the midspan between piers 4 & 5, traversing towards the piers.

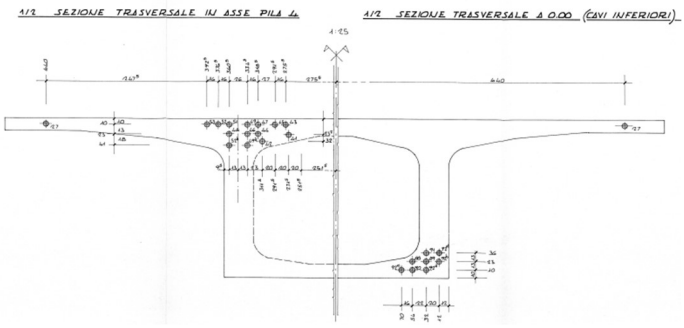


*Figure 40 section and layout of tendons between peer 4 & 5.*

At the opposite end of pier 5, there exists a 15.5-meter-long counter-balance element. A significant tendon, designated as number 27, extends across all the spans along the sides of the girders, as evident in all the provided sections. Moreover, all tendons are divided symmetrically on both sides of the girder, ensuring a well-balanced and even distribution of loads throughout the entire bridge structure. This well-considered design, with the incorporation of the counterbalance and symmetrically duplicated tendons,

greatly enhances the bridge's stability, safety, and overall performance, solidifying its status as a reliable and effective transportation infrastructure.

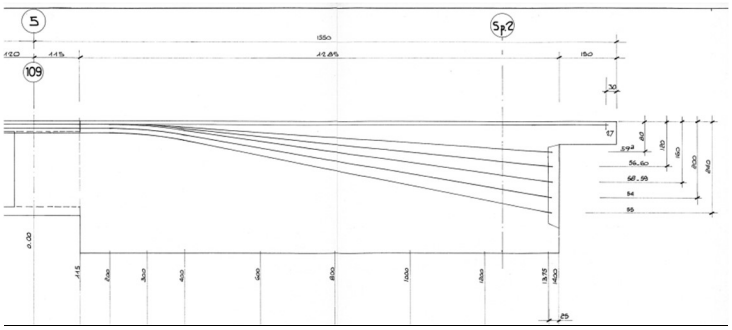

*Figure 41 layout of tendons in the counterbalance*

- Pier properties
  - Foundations:

The foundations of the bridge in the plans are grouped into groups that share the same reinforcements.

- GROUP1: 1S – 2S – 3S – 4S – 5S – 1D – 2D

The foundations of this group are circular in shape with a consistent thickness of 3 meters. These foundations are divided into two equal parts: an upper ring with a diameter of 10.6 meters and a bottom ring with a diameter of 6.9 meters. Acting as both a foundation and a pile cap, a total of 136 piles support the structure. Among these piles, those connected to the upper ring have a length of 16.5 meters, while the remaining piles have a length of 15 meters. To reinforce this group of foundations, a comprehensive steel reinforcement scheme has been implemented, as depicted in Figure 42 steel reinforcement scheme of group's 1 foundations Additionally, Figure 43 distribution of piles under group's 1 illustrates the distribution of piles supporting this particular type of foundation.

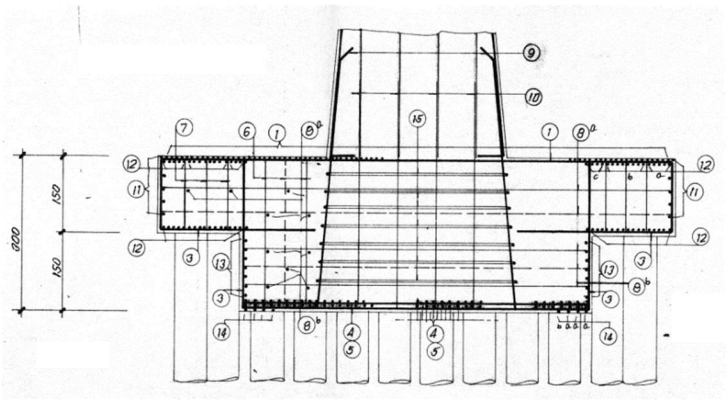

*Figure 42 steel reinforcement scheme of group's 1 foundations*

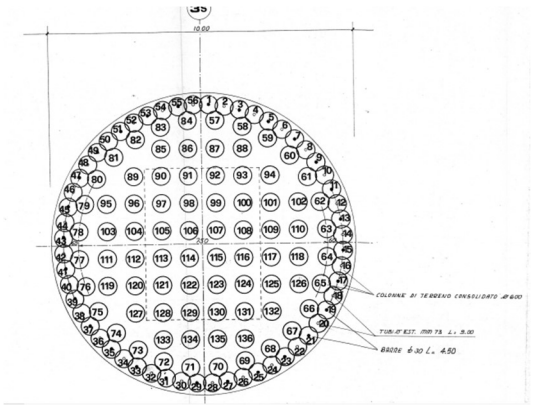

*Figure 43 distribution of piles under group's 1 foundations*

- GROUP2: 3D – 4D

The foundations of this structure are rectangular, measuring 8.5 meters by 12 meters, and have a uniform thickness of 2.5 meters. These foundations serve as both the foundation and pile cap, being supported by a total of 15 main piles. Each main pile comprises several minor piles, with a combined count of 58 minor piles. The length of the piles varies within the range of 10.5 to 18 meters beneath this foundation group. To enhance the strength and stability of these foundations, an extensive steel reinforcement scheme has been implemented, as illustrated in Figure 44 steel reinforcement scheme of group's 2 . Furthermore, Figure 45 distribution of piles under group's 2 provides a visual representation of the pile distribution that supports this specific type of foundation.

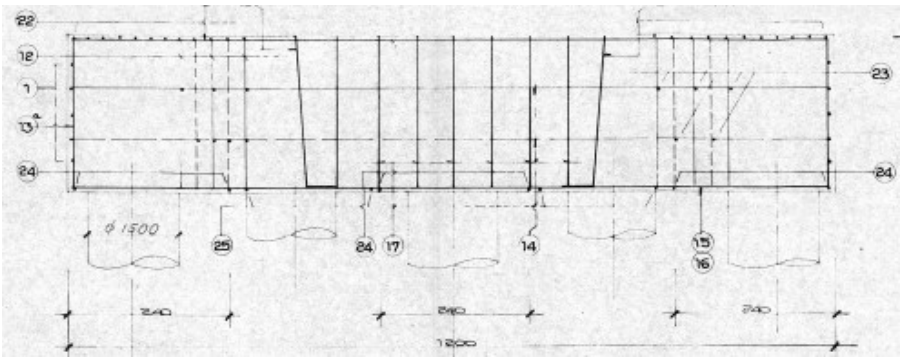


*Figure 44 steel reinforcement scheme of group's 2 foundations*

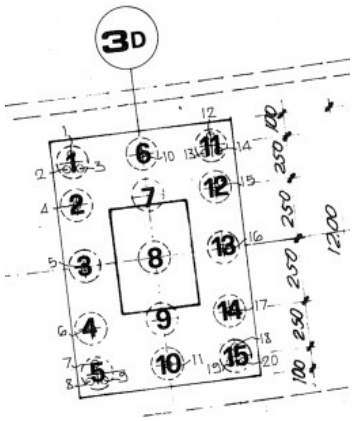


*Figure 45 distribution of piles under group's 2 foundations*

- GROUP3: 5D

The foundation of this group is rectangular, measuring 6 meters by 15.5 meters, with a uniform thickness of 2.5 meters. It serves a dual purpose, acting both as the foundation and the pile cap, and is supported by a total of 48 piles, each with a consistent length of 18 meters. To ensure robust strength and stability, an extensive steel reinforcement scheme has been thoughtfully incorporated, as shown in Figure 46steel reinforcement scheme of group's 3 , Furthermore, Figure 47 distribution of piles under group's 3 foundations provide a visually clear representation of the pile distribution, highlighting its effective support for this specific type of foundation.

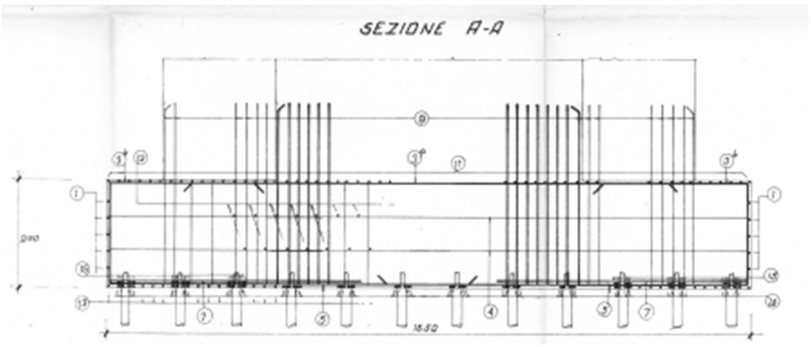


*Figure 46steel reinforcement scheme of group's 3 foundations*

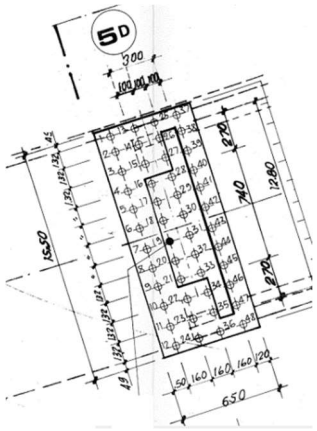


*Figure 47 distribution of piles under group's 3 foundations*

- Piles

All piles, regardless of their positions, are reinforced in a uniform manner. The piles contain longitudinal steel with a diameter of ϕ24 mm, which provides axial strength and load-bearing capacity. Additionally, spiral steel with a diameter of ϕ12 mm is incorporated to enhance the lateral stability and confinement of the concrete within the piles. Figure 48 steel reinforcement layout of the piles illustrates the layout and distribution of these steel reinforcements within the midsection of the piles.

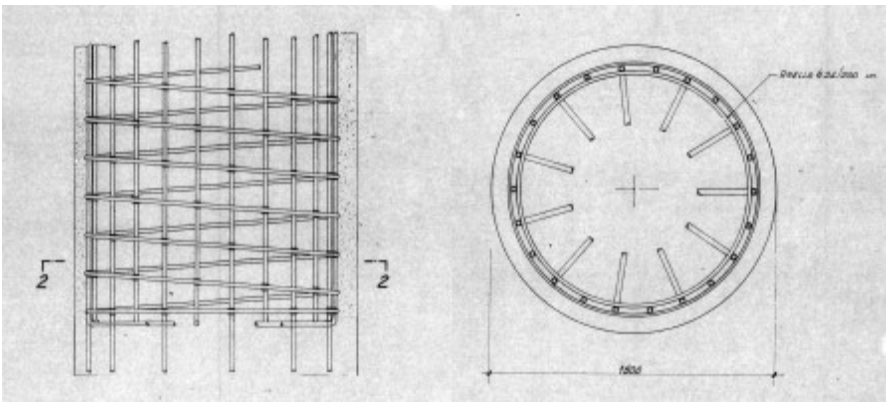


*Figure 48 steel reinforcement layout of the piles*

- Piers & Columns

Columns are also bundled into different groups as follows:

  - Group A: 1S – 1D – 2S – 2D – 3S – 3D – 4S – 4D.

In this group, the columns exhibit a consistent shape, but their heights vary due to the uneven terrain beneath. The tallest column stands at approximately 10 meters, while the shortest measures almost 7.5 meters. To provide structural integrity and support, the vertical reinforcement in the columns is composed of ϕ 26 mm diameter steel bars. Additionally, all other steel bars, such as transverse and shear reinforcements, have a ϕ 16 mm diameter.

| N: PILA | h |
|---|---|
| 1S | 7,471 |
| 2S | 9,166 |
| 3S | 10,056 |
| 4S | 9.766 |
| 1D | 7,674 |
| 2D | 9,464 |
| 3D | 9,036 |
| 4D | 9,553 |

*Figure 49 column heights of group A*

The vertical load on the structure is initially distributed onto two pads situated directly above the columns, as depicted in Figure 51 Bridge-Column Connection. From there, the load is efficiently transferred to each column, enabling them to effectively bear the vertical loads. A detailed discussion regarding the load bearing pads will be presented at the conclusion of this section.

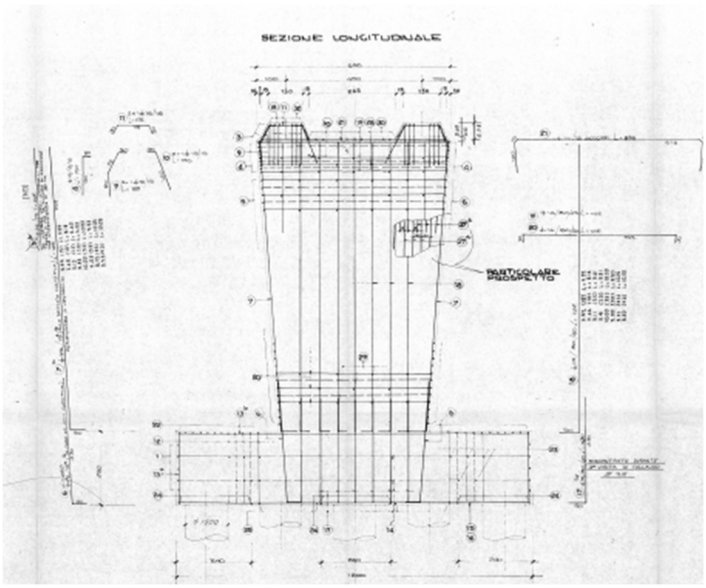


*Figure 50 cross section of group A columns*

*Figure 51 Bridge-Column Connection*

- Group B: 5S – 5D.

In this group of columns, a distinctive feature sets them apart from the others - they serve as counter-balance columns. This design incorporates a counter-balance weight on the opposite side of the main load to achieve multiple benefits. Termed "counter-balance columns," they are strategically employed to reduce negative moments on the column, enhance bridge stability, and improve vibration damping.

The reinforcement of these columns is categorized into two parts:

- **Column Reinforcement:** For the main column, all primary steel bars have a diameter of ϕ 26 mm, while the secondary reinforcements are ϕ 16 mm in diameter.
- **Counter-Balance Side Reinforcement:** On the counter-balance side, the main transverse reinforcements are ϕ 26 mm, while the transverse reinforcements going in the other direction have a diameter of ϕ 20 mm. Additionally, all other secondary steel bars are ϕ 16 mm in diameter.

To support the vertical load of the counter-balance weight, the structure utilizes two pads situated above four piles on one side and two other pads located above the column on the opposite side. Figure 52 Counterbalance column scheme shows the scheme of the counterbalance column.

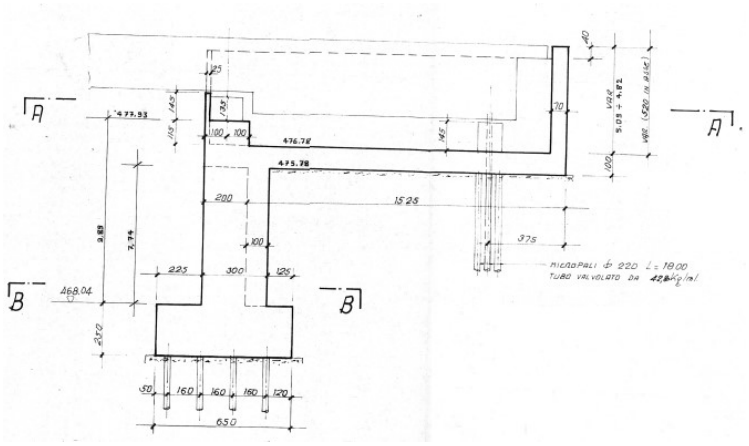


*Figure 52 Counterbalance column scheme*

- Group C: SP1

At the opposite end of the bridge a different type of column is present, standing at a height of 4 meters above the foundation. Similar to the other columns in the structure, this column features main steel vertical reinforcement with a diameter of ϕ26 mm, along with secondary reinforcement comprising ϕ16 mm steel bars. Figure 53 reinforcement layout of sp1describes the steel reinforcement layout of the sp1 column.

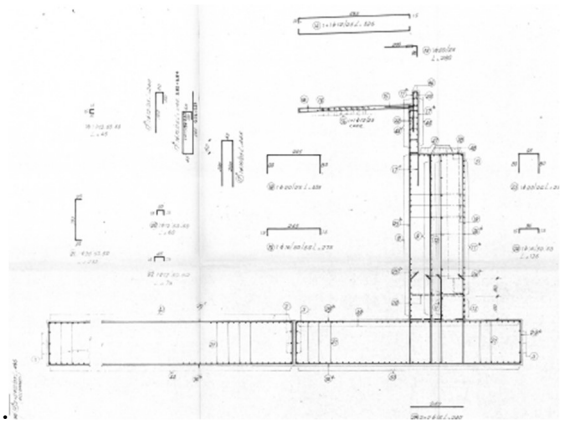

*Figure 53 reinforcement layout of sp1*

## 4.2.2. Defining Boundary Conditions

In the field of civil engineering, the design of bridges involves careful consideration of various factors that impact their structural integrity. One pivotal aspect is the choice of boundary conditions. Engineers deliberately avoid fully fixing these conditions due to the dynamic nature of bridge environments. The inclusion of temperature fluctuations, live loads, and natural movements necessitates a certain level of adaptability within the bridge structure. The absence of flexibility in boundary conditions can lead to structural issues caused by thermal expansion and contraction, resulting in stress and deformation. Furthermore, live loads, such as vehicular traffic, impose dynamic forces, making a degree of flexibility essential to prevent excessive stress. This delicate balance between stability and flexibility constitutes a fundamental principle in bridge engineering.

The bridge under examination adheres to the principle of partially fixed supports, a crucial concept in bridge engineering. The bridge's boundary conditions are meticulously outlined in the project plans, detailing how it bears its weight and transfers loads to the supporting piers and abutments. At the heart of this structural design are bearing pads, serving a multitude of critical functions. These pads play a pivotal role in evenly distributing the formidable loads generated by the bridge's superstructure onto the supporting piers and abutments. By preventing direct contact that could lead to uneven stress, they ensure structural integrity. Additionally, bearing pads act as shock absorbers, effectively reducing vibrations and impacts, thus enhancing passenger comfort. This multifaceted role also involves facilitating controlled movement and alignment, which is essential for accommodating temperature-induced expansion and contraction. By minimizing stress concentrations and permitting controlled movement, bearing pads significantly contribute to the bridge's longevity and safe operation. Their accessibility further simplifies maintenance tasks, solidifying their role in ensuring the reliability and durability of bridges.

*Figure 54 Pier Elevation*

- Regarding the specific boundary conditions:

The boundary conditions of the bridge were thoughtfully designed to optimize performance. On the piers, two bearing pads have been strategically placed. All right-side pads permit motion in both the X and Y directions, while the left-side pads restrict movement to the Y-axis. The Z direction is essentially fixed, necessitated by the substantial self-weight of the bridge. Atop the right-side abutment (5s), four bearing pads serve specific roles. Pad 1 is unrestrictive, allowing free movement in both X and Y directions. Pad 2 permits motion solely along the X-axis, while Pad 3 facilitates movement exclusively along the Y-axis. Pad 4, in contrast, is securely restrained in all directions, ensuring stability and optimal load distribution. These carefully tailored boundary conditions, combined with the versatile bearing pads, collectively form the foundation of the bridge's structural integrity and safe operation.

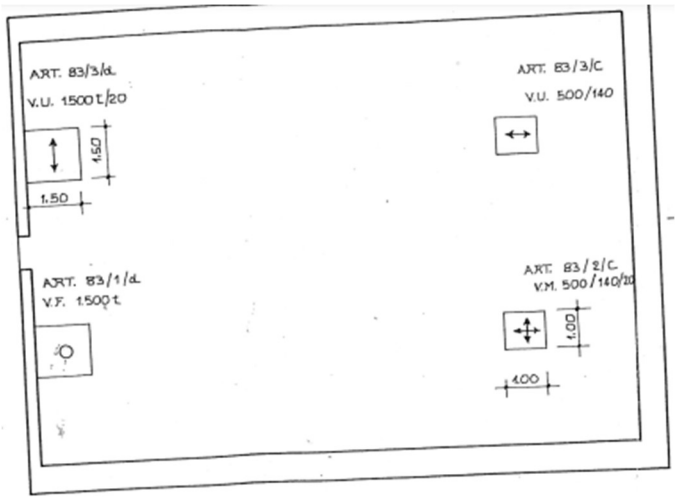


*Figure 55 5S abutment Bearing pads restrains*

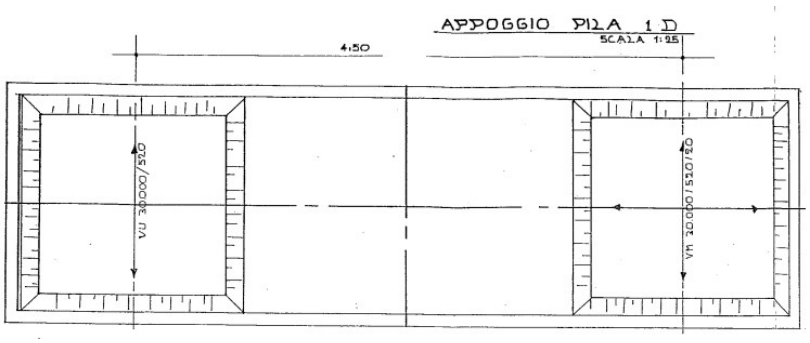


*Figure 56 Pier Bearing pads restraints*

## 4.2.3. Defining material properties for the model

- Material properties

The designer's plans include information regarding the concrete mixes' compressive strength for the project. Additionally, the plans provide specifications concerning the yielding and ultimate stresses associated with both the tendons and the steel bars.

- **<u>Concrete Compressive Strength</u>**:
  - The concrete mix used for decks is **C50/60**, which has a compressive strength of **50 MPa**.
  - The concrete mix used for peers is **C35/45**, with a compressive strength of **35 MPa**.

- **<u>Steel Properties</u>**:
  - Reinforcement Steel:
    - Type: Fe B 44 K
    - Yielding strength: 260 MPa
  - tendons:
    - Type of steel: not provided.
    - Yielding strength: 1600 MPa
    - Ultimate strength: 1800 MPa
    - Number of wires in the tendon: 19
    - Diameter of tendon: 0.6”

- Time dependent material

The well-designed MIDAS Civil interface facilitates the process of specifying time-dependent material properties, which encompasses factors like creep, shrinkage, and the progressive gain of compressive strength in concrete.

- Creep: is a phenomenon where a concrete element gradually elongates or deforms over time due to sustained loading. It's a time-dependent process related to the internal structure rearrangement of concrete under stress.
- Shrinkage: is the reduction in volume of a concrete element over time, primarily due to moisture loss during drying. Shrinkage can result in cracks and is particularly relevant during concrete curing and hardening.

Moreover, MIDAS Civil facilitates the modelling of concrete's progressive increase in compressive strength over time. Users have the flexibility to access and choose compressive strength development equations from relevant codes.

For each of these material properties, MIDAS Civil offers an intuitive graphical representation in the form of curves, illustrating how these properties change over time. Once these properties are defined, users can seamlessly link them with pre-defined materials, making the whole process more efficient.

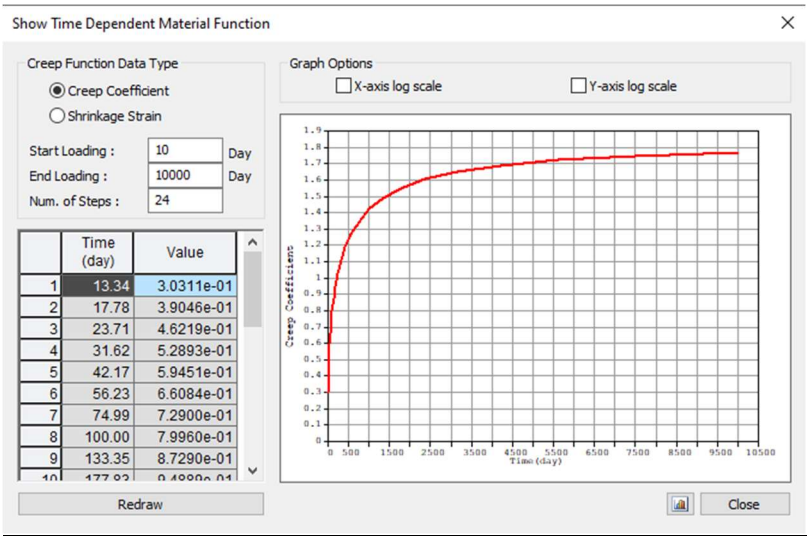


*Figure 57 Creep coefficient Graph provided by Midas*

### 4.2.4. Defining Loads Acting on the Structure

The loads acting on bridges largely resemble those encountered by other structures, yet with some unique considerations. Below, we will outline a list of loads specified by the bridge designer that will exert their force on the structure.

The designer considered two key types of forces: vertical and horizontal loads. Vertical forces impact the bridge spans initially, transferring their effects to the piers where they and the spans meet. In contrast, horizontal forces are primarily assessed in relation to their impact on the piers.

Group 1: Vertical Loads

- ➔ SELF-WEIGHT which is variable in accordance with the shape of the section the specific weight of the section is considered to be 25 kN /$m^{3.}$
- ➔ SUPER IMPOSED DEAD LOAD
  - Barrier load: (10.4 kN /m & 13.1kn/m)
  - channels load: (4.5 kN /m)
  - ballast load or gravel layer load: (38.1 kN/m)
  - all SDL will sum up for a total of (66.1 kN/m)
- ➔ Moving loads or accidental loads. This type of load is unique for highway projects. The designer divided the load into 2 parts. The first is the crowd load and the other is the vehicular load. Since the bridge is 2 lanes, The vehicular load consists of 2 loads. The designer also provided the value of this load for every span in the bridge.

The moving load can be derived from the NTC 2018 code through the following formula:

$$q_{L,a} = 128.95\ (\frac{1}{L})^{0.25}\ [\frac{kn}{m}]$$

$$q_{L,b} = 88.71\ (\frac{1}{L})^{0.38}\ [\frac{kn}{m}]$$

$$q_{L,c} = 77.12\ (\frac{1}{L})^{0.38}\ [\frac{kn}{m}]$$

Group2: Horizontal Loads

- ➔ Wind load:

Having the bridge in zone 1 region A and on an altitude less than 500m and with an exposition coefficient = 1.3 the wind load is equal to Q20 = 1.17 kN /m2

The wind load can be calculated and verified using the guidelines and formulas that are provided by the NTC 2018 code.

$$p = q_b . c_e . c_p . c_d$$

- $q_b$: is the referance of kinetic pressure
- $c_e$: is the exposure coefficent
- $c_p$: is the shape coefficent
- $c_d$: is the dynamic coefficient

| Zona | Descrizione | $v_{b,0}$ [m/s] | $a_0$ [m] | $k_s$ |
|---|---|---|---|---|
| 1 | Valle d'Aosta, Piemonte, Lombardia, Trentino Alto Adige, Veneto, Friuli Venezia Giulia (con l'eccezione della provincia di Trieste) | 25 | 1000 | 0,40 |
| 2 | Emilia Romagna | 25 | 750 | 0,45 |
| 3 | Toscana, Marche, Umbria, Lazio, Abruzzo, Molise, Puglia, Campania, Basilicata, Calabria (esclusa la provincia di Reggio Calabria) | 27 | 500 | 0,37 |
| 4 | Sicilia e provincia di Reggio Calabria | 28 | 500 | 0,36 |
| 5 | Sardegna (zona a oriente della retta congiungente Capo Teulada con l'Isola di Maddalena) | 28 | 750 | 0,40 |
| 6 | Sardegna (zona a occidente della retta congiungente Capo Teulada con l'Isola di Maddalena) | 28 | 500 | 0,36 |
| 7 | Liguria | 28 | 1000 | 0,54 |
| 8 | Provincia di Trieste | 30 | 1500 | 0,50 |
| 9 | Isole (con l'eccezione di Sicilia e Sardegna) e mare aperto | 31 | 500 | 0,32 |

*Figure 58 Italian wind zones*

$$V_b = V_{b0} * C_a$$

$$C_a = 1 \quad a_s \leq a_0$$

$$C_a = 1 + K_s \left(\frac{a_s}{a_0} - 1\right) \quad a_0 < a_s < 1500m$$

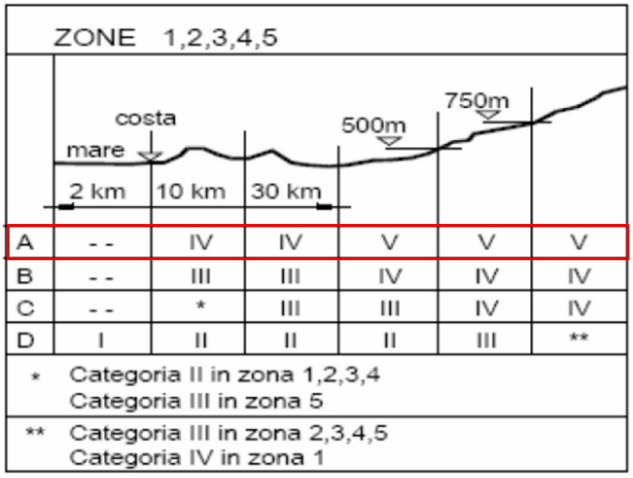


| | | | | | | |
|---|---|---|---|---|---|---|
| A | - - | IV | IV | V | V | V |
| B | - - | III | III | IV | IV | IV |
| C | - - | * | III | III | IV | IV |
| D | I | II | II | II | III | ** |

* Categoria II in zona 1,2,3,4
Categoria III in zona 5

** Categoria III in zona 2,3,4,5
Categoria IV in zona 1

*Figure 59 Zoning in accordance with altitude*

| Categoria di esposizione del sito | $K_r$ | $z_0$ [m] | $z_{min}$ [m] |
|---|---|---|---|
| I | 0,17 | 0,01 | 2 |
| II | 0,19 | 0,05 | 4 |
| III | 0,20 | 0,10 | 5 |
| IV | 0,22 | 0,30 | 8 |
| V | 0,23 | 0,70 | 12 |

*Figure 60 site exposition categories*

$$Ce(Z) = K_r^2 * C_t * \ln\left(\frac{z}{z_0}\right) * [7 + C_t * \ln(Z/Z_0)], \qquad Z \geq Z_0$$

$$C_e(Z) = C_e(Z_{min}), \qquad Z < Z_{min}$$

➔ Centrifugal force:

Because of the curvature of the bridge with a radius of 600m a horizontal force is formed Fc = 0.5 kN/M

## 4.3. Finite Element Modeling of the Structure

### 4.3.1. Construction Stages Analysis

The bridge construction employed the innovative free cantilevered method, a technique characterized by the incremental assembly of segments in a sequential manner. This process involved adding one segment at a time from both sides of the bridge, meticulously maintaining equilibrium throughout the construction process. By carefully orchestrating the placement of segments from either end, the construction team ensured the structural integrity and balance of the bridge were consistently preserved.

| ID | Task Mode | Task Name | Duration |
|---|---|---|---|
| 1 | | peer 1 Construction (construction stage 1) | 2 days |
| 2 | | Segment Additions | 34 days |
| 3 | | Left Span Attachment | 2 days |
| 4 | | Peer 2 Construction (construction stage 2) | 2 days |
| 5 | | Segment Additions | 34 days |
| 6 | | Mid-segment Addition | 2 days |
| 7 | | Cantilevered Span addition "peer 2" | 4 days |
| 8 | | Peer 3 Construction (construction stage 3) | 2 days |
| 9 | | Segments Addition "cantilevered span 3" | 18 days |
| 10 | | Peer 4 construction (construction stage 4) | 2 days |
| 11 | | Segments Addition "cantilevered span 4) | 18 days |
| 12 | | Mid-segment Addition | 2 days |
| 13 | | Abbutment SP2 & counter-weight placement | 2 days |
| 14 | | Cantilevered Span Extension | 2 days |
| 15 | | Final Structure Connection | 2 days |

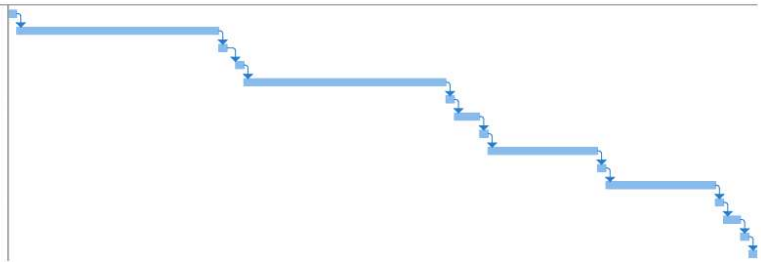

*Figure 61 Gantt Chart of the bridge*

- Peer 1 Construction (Construction Stage 1)

The initial phase involves the construction of Peer 1.

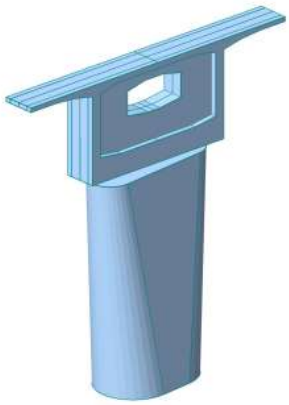

*Figure 62 Peer 1*

- Segments Addition (Construction Stage 2)

Seventeen segments are simultaneously added from each side of the column to maintain the cantilevered equilibrium state of the structure.

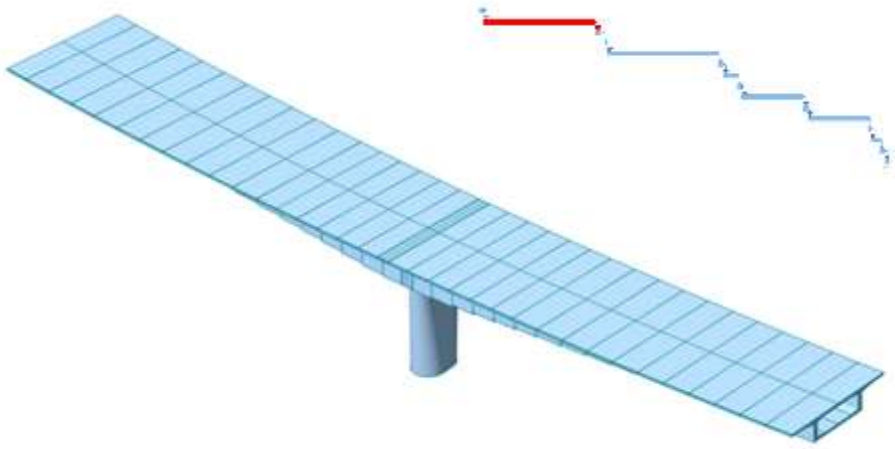

*Figure 63 Span 1*

- Left Span Attachment (Construction Stage 3)

The left span of the bridge is attached to abutment SP1, transitioning the structure from both ends cantilevered to a simply supported beam with one end cantilevered.

- Peer 2 Construction (Construction Stage 4)

Peer 2 is constructed during this period.

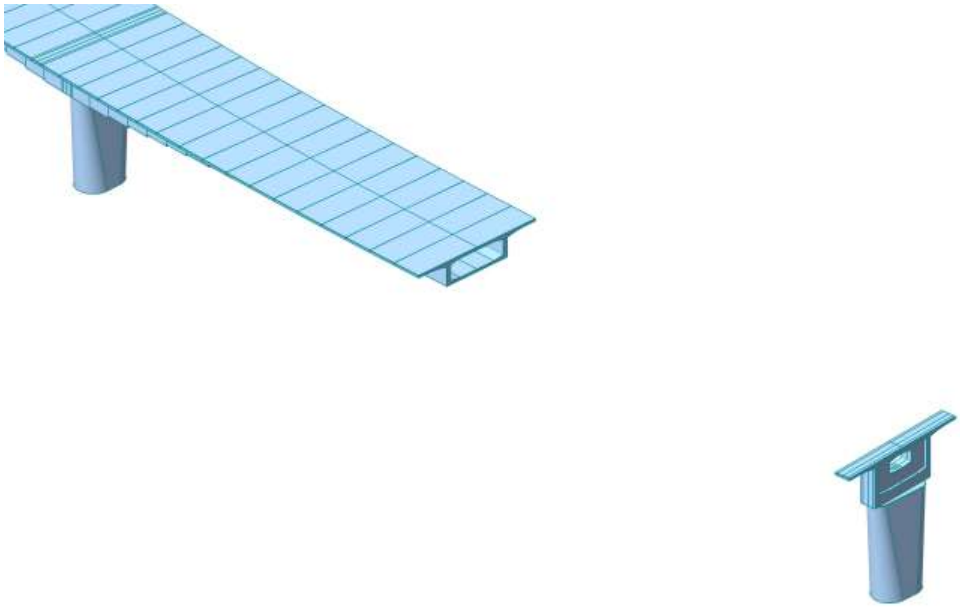

*Figure 64 Peer 2 construction.*

- Segments Addition (Construction Stage 5)

Seventeen segments are added from each side of column 2, maintaining the same scheme as in Construction Stage 1.

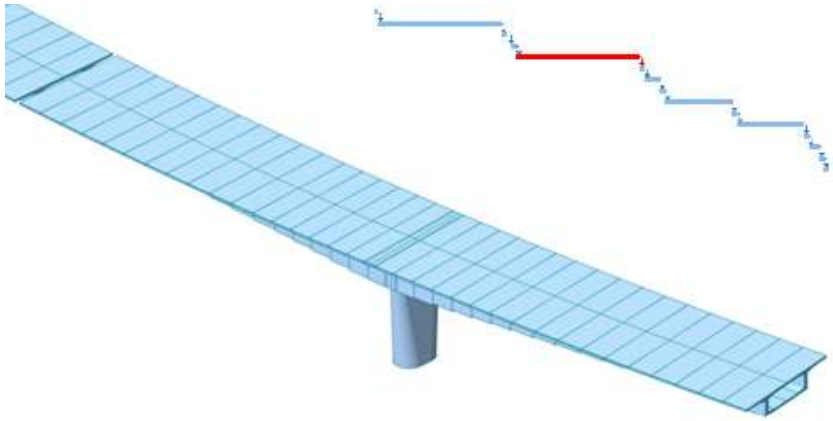

*Figure 65 Completion of span 2*

- Mid-Segment Addition. (Construction Stage 6)

The mid-segment connecting the cantilevered spans from Peer 1 and Peer 2 changes the structural scheme to have two continuous spans with one end cantilevered from Peer 2.

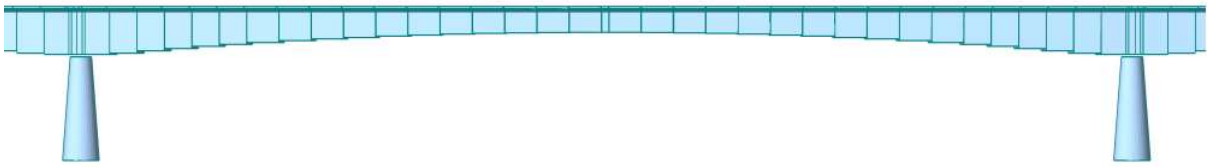

*Figure 66 Span 1 & 2 Connection*

- Cantilevered Span Addition (Peer 2) (Construction Stage 7)

Two segments are added to the cantilevered span originating from Peer 2.

- Peer 3 Construction (Construction Stage 8)

Peer 3 is constructed, and the cantilevered span is attached to it, transforming the structure scheme to three simply supported beams.

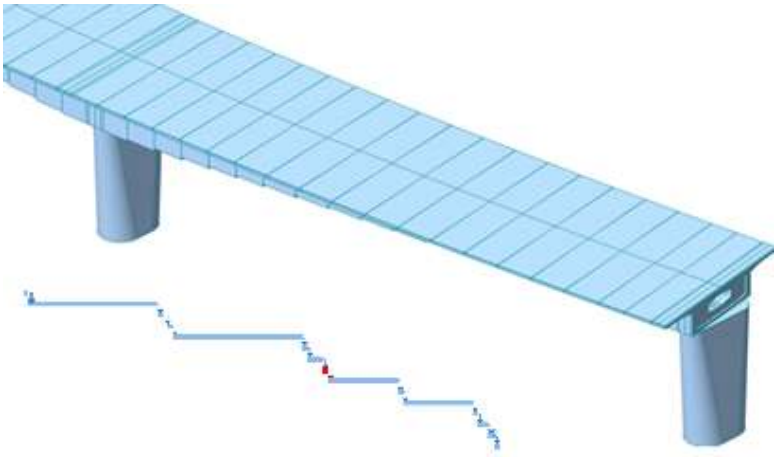

*Figure 67 Peer 3 construction*

- Segments Addition, Cantilevered Span. (Construction Stage 9)

Nine segments are added to the left side of Peer 3, forming a cantilevered span.

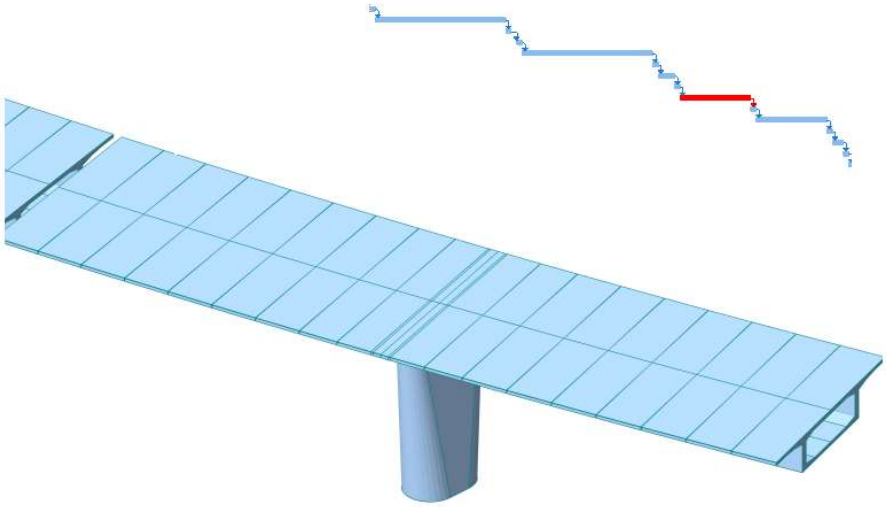

*Figure 68 Completion of span 3*

- Peer 4 Construction (Construction Stage 10)

Peer 4 is constructed.

- Segments Addition (Construction Stage 11)

Nine segments are added from each side of Peer 4, maintaining the same equilibrium cantilevered scheme.

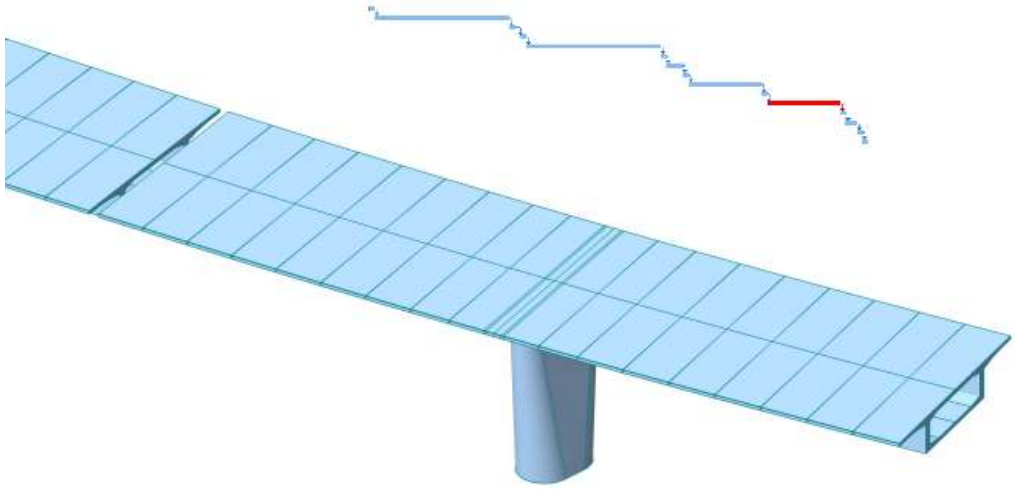

*Figure 69 Completion of span 4*

- Mid-Segment Addition (Construction Stage 12)

The mid-segment connecting the cantilevered spans from Peer 3 and Peer 4 is added.

- Abutment SP2 and Counterweight Placement (Construction Stage 13)

Abutment SP2 and the counterweight above it are placed.

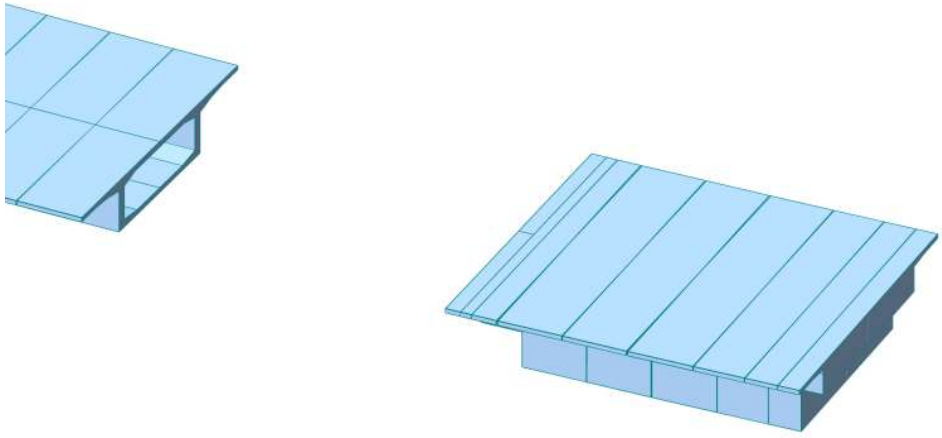

*Figure 70 Construction of Sp2 Abutment*

- Cantilevered Span Extension (Construction Stage 14)

Six segments are added to the abutment SP2 during this phase.

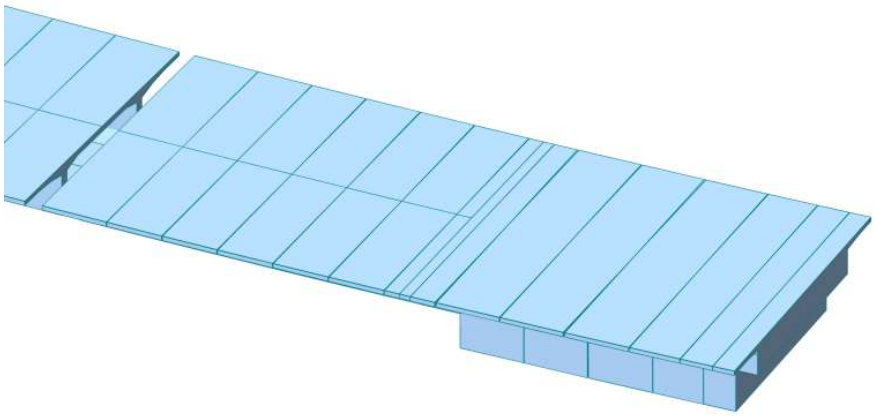

*Figure 71 Completion of span 5*

- Final Structural Connection

The mid segment between the cantilevered parts from Peer 4 and Abutment SP2 is connected, marking the completion of the structure.

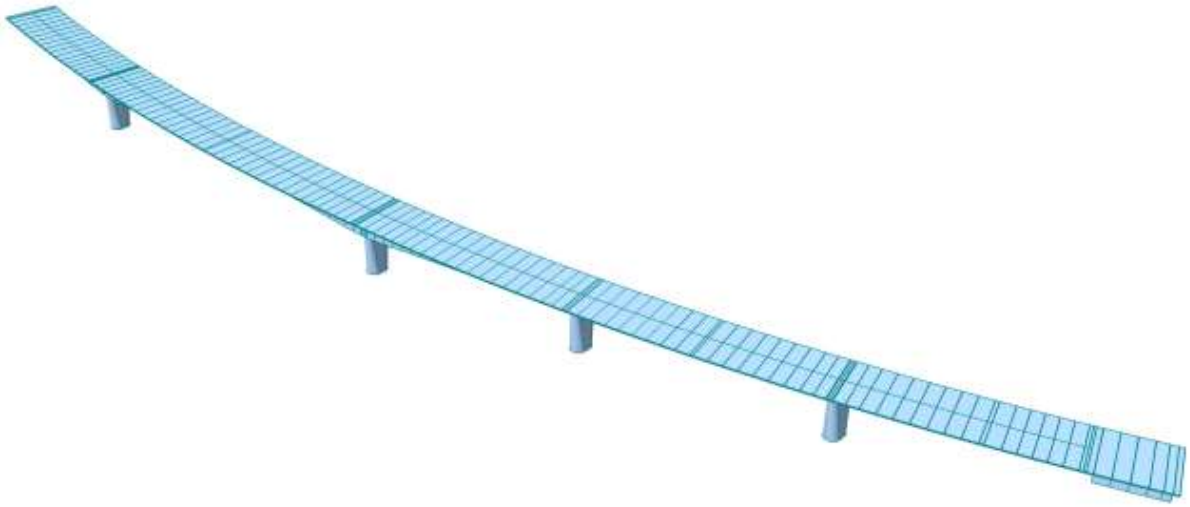

*Figure 72 Final layout of the bridge*

### 4.3.2. Torsional Effect on the Curved Model

Due to the substantial curvature of the bridge, there was initial speculation that this curvature would have a negligible impact on the overall torsional moment. Consequently, two models were simulated: one with a straight configuration and the other with a curved design. The analysis specifically focused on the longest span of the bridge, referred to as span 2, under the assumption that the maximum torsion would occur at this location.

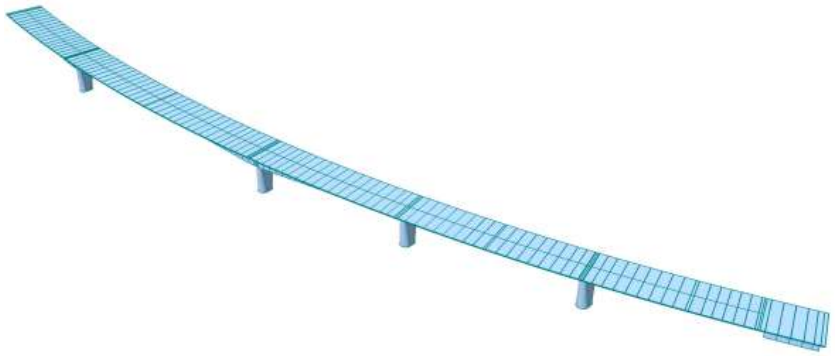

*Figure 73 Curved bridge*

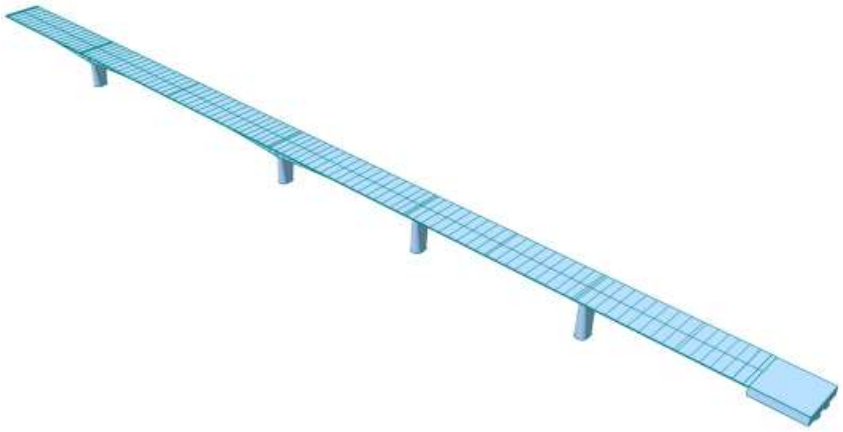

*Figure 74 Straight bridge*

To better comprehend the influence of the curvature, the applied loads on the bridge were minimized, and the study exclusively considered the effects of moving loads and tendons. These two factors were identified as the primary contributors to the torsional moment.

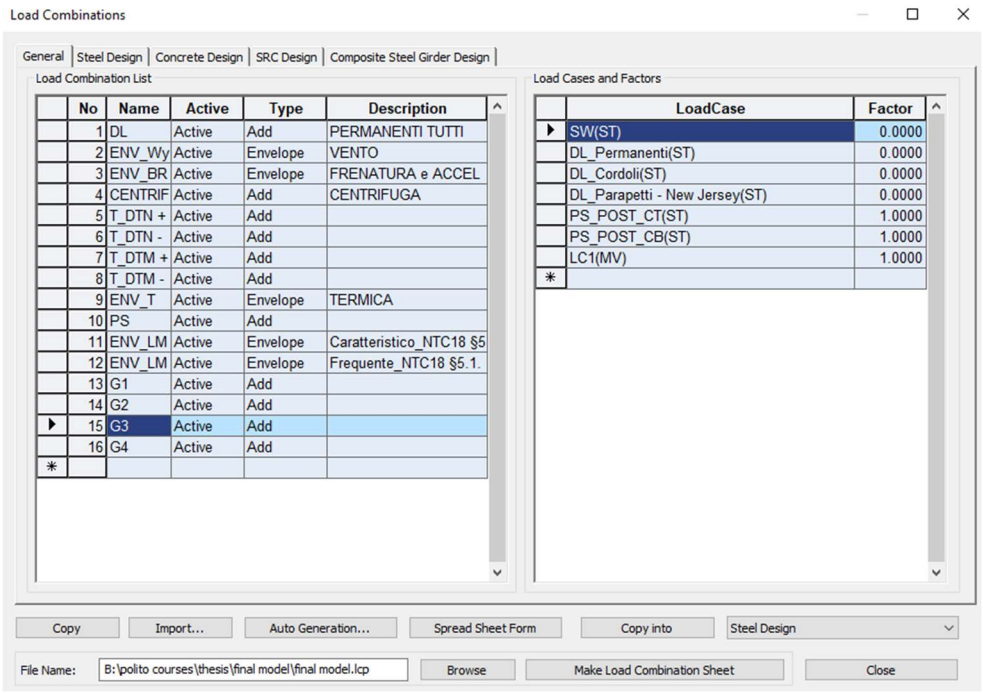


*Figure 75 loads acting on the bridge*

Upon completing the simulation, it was determined that the curvature amplified the torsional effect by 20%, signifying a notable increase.

| Data extracted from curved bridge | | | |
|---|---|---|---|
| Elem | Shear-z (kN) | Torsion (kN·m) | Moment-y (kN·m) |
| 1 | -3850.92 | 11237.78 | -66301.75 |
| 2 | -3261.57 | 10145.39 | -35919.27 |
| 3 | -2617.29 | 8593.82 | 16493.82 |
| 4 | -1964.19 | 6757.09 | 26749.91 |
| 5 | -1371.29 | 5194.94 | 33935.58 |
| 6 | -1288.32 | -5001.58 | 34154.71 |
| 7 | 1337.62 | -5131.25 | 34124.58 |
| 8 | 1928.76 | -6702.68 | 28157.59 |
| 9 | 2580.84 | -8544.26 | 18269.63 |
| 10 | 3224.91 | -10126.35 | -35415.04 |
| 11 | 3814.59 | -11269.86 | -65327.28 |

*Table 2 data extracted from curved bridge*

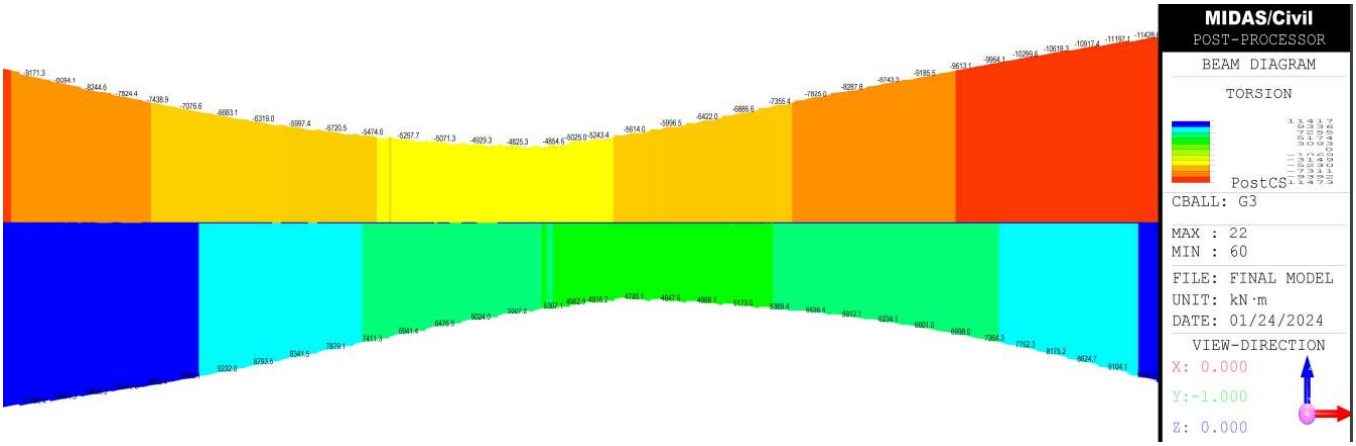


*Figure 76 Torsion for curved bridge*

| Data extracted from straight bridge | | | |
|---|---|---|---|
| Elem | Shear-z (kN) | Torsion (kN·m) | Moment-y (kN·m) |
| 1 | -3709.03 | 9186.72 | -62979.69 |
| 2 | -3148.85 | 7897.13 | -33861.19 |
| 3 | -2531.97 | 6502.77 | 15974.02 |
| 4 | -1903.73 | 5121.61 | 26040.95 |
| 5 | -1330.37 | 4106.01 | 33015.73 |
| 6 | -1249.99 | -3987.28 | 33232.4 |
| 7 | 1294.3 | -4081.56 | 33214.03 |
| 8 | 1864.77 | -5102.55 | 27508.02 |
| 9 | 2491.8 | -6487.94 | 17725.46 |
| 10 | 3109.08 | -7884.18 | -33121.01 |
| 11 | 3670.86 | -9173.74 | -61708.76 |

*Table 3 Data extracted from straight bridge*

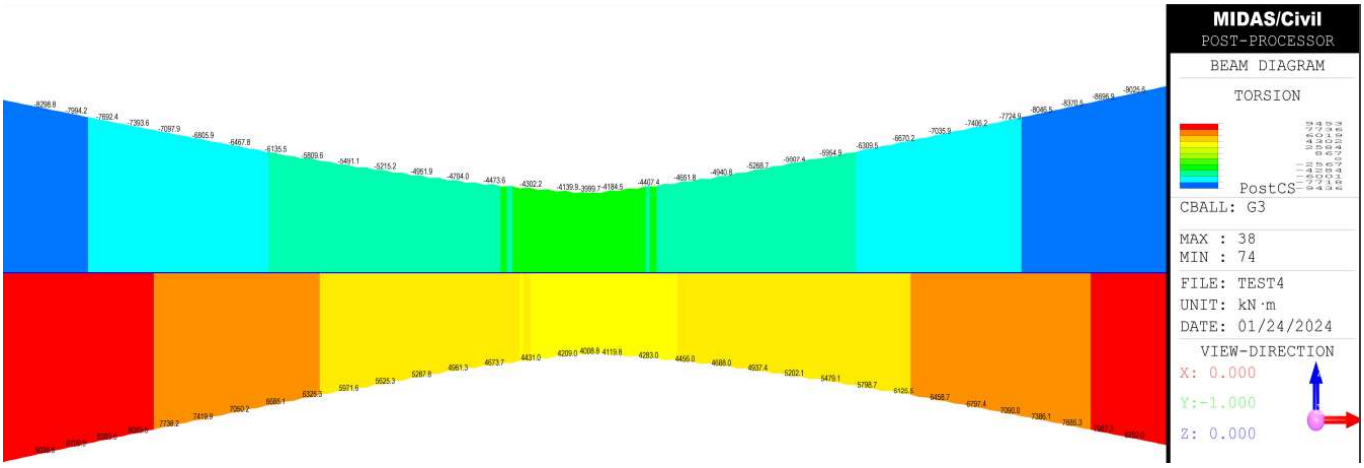


*Figure 77 Torsion effect of the straight bridge*

In light of these findings, acknowledging the significant 20% increase in torsional effect due to curvature, it was deemed essential to consider this factor in the subsequent modelling. This choice ensures a more comprehensive and accurate representation, accounting for both the dominant bending and the now acknowledged influential torsional moments in the structural analysis.

### 4.3.3. Validation Of the Finite Element Model

In the field of civil engineering, the process of model validation plays a pivotal role in refining FE. models of critical structures. The primary objective is to enhance the accuracy of these models by incorporating reference data obtained from experimental tests or numerical exercises. Through meticulous comparison of various quantities of model predictions with test data, known as multivariate analysis, engineers strive to ensure that the refined FE. models accurately represent the physical behavior of actual structures (Thacker et al. 2004). This approach, which has only recently been extended to civil engineering structures, holds significant promise in optimizing designs and enhancing the understanding of the behavior of structures(Atamturktur, Hemez, and Laman 2012). Ultimately, the success of repair and retrofit schemes hinges on the development of verified and validated simulation capabilities, empowering engineers to make informed decisions regarding the preservation and enhancement of critical structures (Sankararaman, Ling, and Mahadevan 2011).

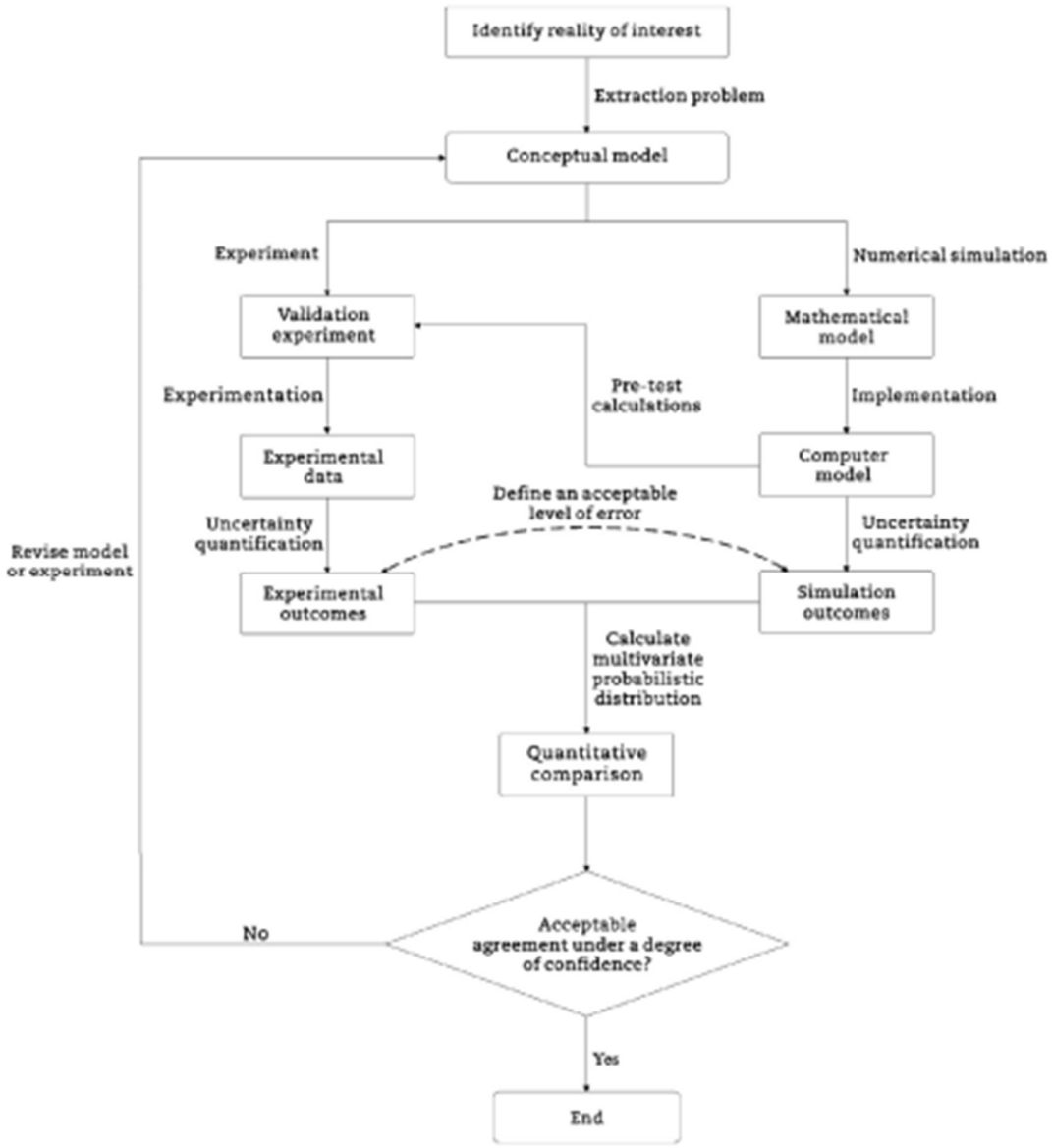


*Figure 78 Flowchart of model validation process.*(Lin, Zong, and Niu 2015)

In order to validate the model designed on Midas, two distinct approaches were undertaken. The first approach involved verifying the torsion moment diagram, a critical aspect of structural analysis, by comparing it with a study conducted by (Mairone et al. 2022). This study delves into the behavior of horizontally curved steel box-girder bridges, specifically focusing on bending and torsional moments. The second approach centered on verifying the maximum deflection of the bridge under a point load, utilizing hand calculations for comparison. This method provided a practical means of confirming the model's predictive capabilities by assessing its agreement with established engineering calculations. By employing these two rigorous verification approaches, engineers sought to validate the Midas-designed model comprehensively, ensuring its suitability for accurate structural analysis and design considerations.

➢ verifying the torsion moment diagram

The study conducted by Mairone et al. in 2022 provided valuable insights into the behavior of horizontally curved steel box-girder bridges under different constraint conditions, specifically fixed-fixed and isostatic constraints. Under the isostatic constraint, the torsional effect was maximized at the extremities of the bridge with zero bending moment, while the fixed-fixed constraint resulted in maximal bending moment and minimal torsion at the extremities. Figure 79 from the study illustrated that maximum torque moments occurred along the central span, near the quarter points, while torsional moments were relatively high at pier locations and viaduct ends, decreasing towards the mid-spans.

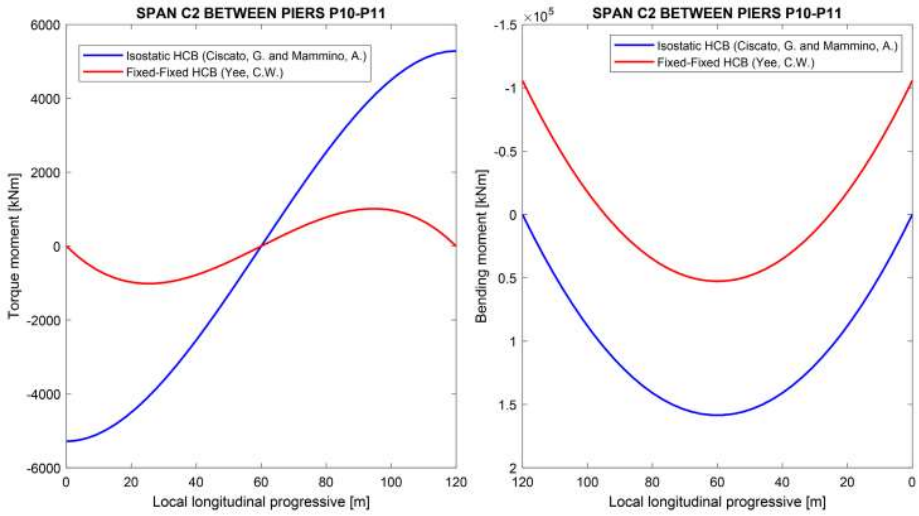


*Figure 79 Torque and Bending Moment Diagrams under permanent loads, comparing Isostatic and Hinged-Clamped configurations.*(Mairone et al. 2022)

$$M(\omega) = R_{v,A} * R\sin(\omega) - q * R^2[1-\cos(\omega)] * \sin(\omega) + M_A * \cos(\omega) * T_A * \sin(\omega)$$

$$T(\omega) = -R_{V,A} * R * [1-\cos(\omega)] + q * R * [\omega - \cos(\omega)] - M_A * \sin(\omega) + T_A * \cos(\omega)$$

In the context of the thesis's case study, the boundary conditions were assumed to fall somewhere between isostatic and fixed-fixed conditions, with permanent loads being the sole consideration. Despite this intermediary positioning of the constraints, the resulting torsional diagram closely mirrored the trend observed in (Mairone et al. 2022) study. This alignment was notable despite the presence of bending moments at the extremities, which logically corresponds to the boundary conditions where rotational restraints along the x-axis were absent, allowing for torsional effects to coexist with bending moments. Given that the moment at the x-axis (Mx) representing torsion exhibited a similar shape to that observed in the referenced study, it can be reasonably inferred that the model is validated.

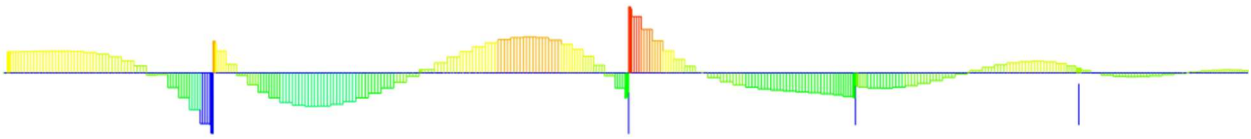

*Figure 80torque moment under permanent load of the case study*

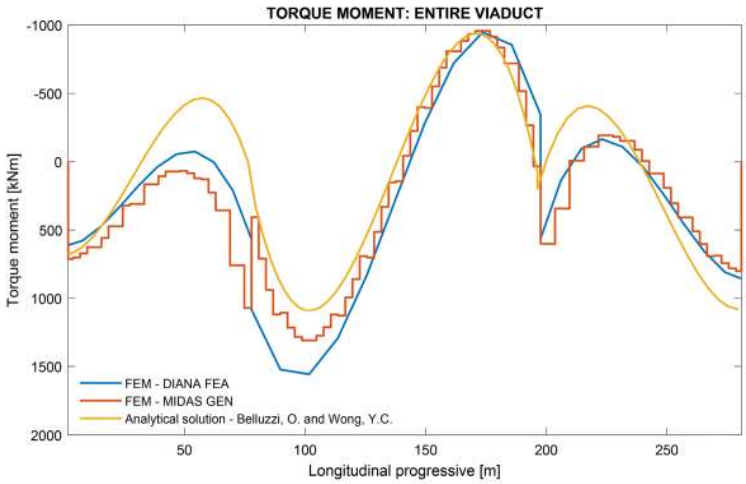


*Figure 81 Torque diagram, under the action of permanent loads.*(Mairone et al. 2022)

- verifying the deflection of the bridge

Another validation method was applied to the bridge, this time focusing on its deflection limits. To facilitate the process, a point load of 1000 kN was placed at the center of the 4th span. Subsequently, the bending moment diagram was drawn, and deflection values were calculated. The bending moment was determined using the moment distribution analysis method. While Deflection was formulated using the conjugate method, following a specific general approach. (DING 1990)

- $\delta_{max} = \frac{\beta \mu^2 \rho l^3}{192 \beta_{sp}}$

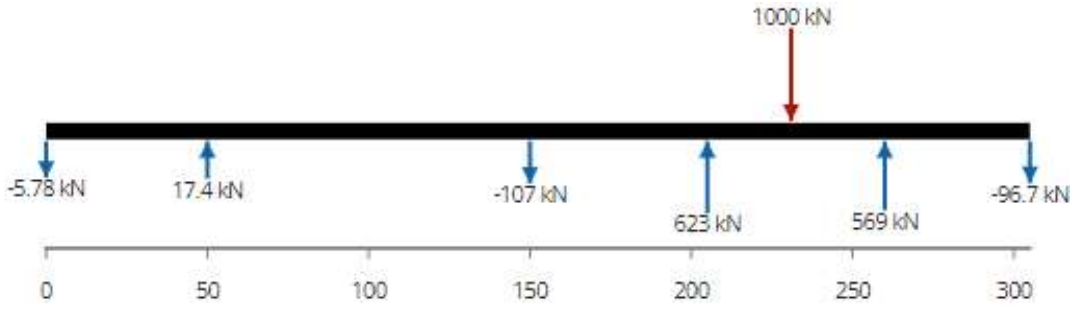


*Figure 82 Loading of the structure*

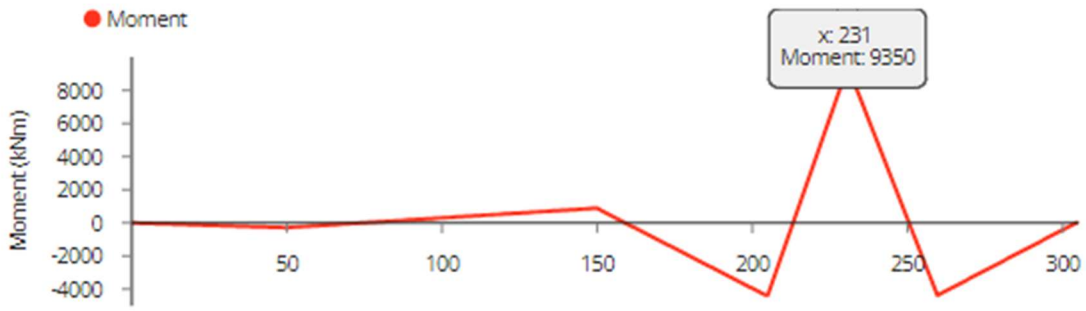


*Figure 83 Calculated bending moment.*

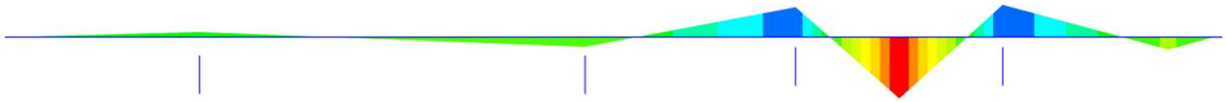

*Figure 84 bending moment from Midas*

The manually calculated bending moment of the structure using the moment distribution method aligns exactly with the value generated by the Midas software. However, it's noteworthy that the figures were plotted with differing sign conventions.

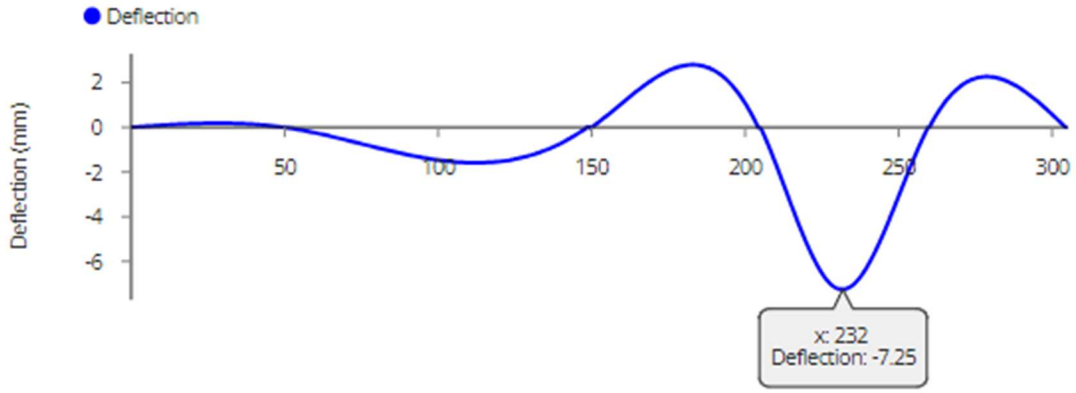


*Figure 85 calculated deflection*


*Figure 86 deflection from Midas*

Using identical cross-sectional considerations and modulus of elasticity for both methods, the resulting bending moment diagram was consistent. Consequently, it was evident that the deformation would yield identical values in both the Midas software and hand calculations. Employing the conjugate method in the hand calculations, the deformation values were found to be almost identical.

### 4.3.4. Challenges Encountered with Midas Wizard Bridge Modelling

The Midas Wizard, while a valuable tool for bridge modeling, comes with certain limitations, particularly when dealing with non-typical bridge structures. In the context of our specific bridge design, several issues were encountered during the modeling process.

➢ Segment Distribution and Pier Structure Discrepancies

- The Midas tutorial instructs that the number of left and right segments should be equal for structural balance. It requires that all piers have equal numbers of left and right segments, regardless of segment length discrepancies.
- In the bridge under study, a unique configuration was present. Pier 3 had eight segments on one side and none on the other. These eight segments were attached to the segments of span (2-3). The wizard of the software, however, was unable to accommodate this non-standard arrangement.

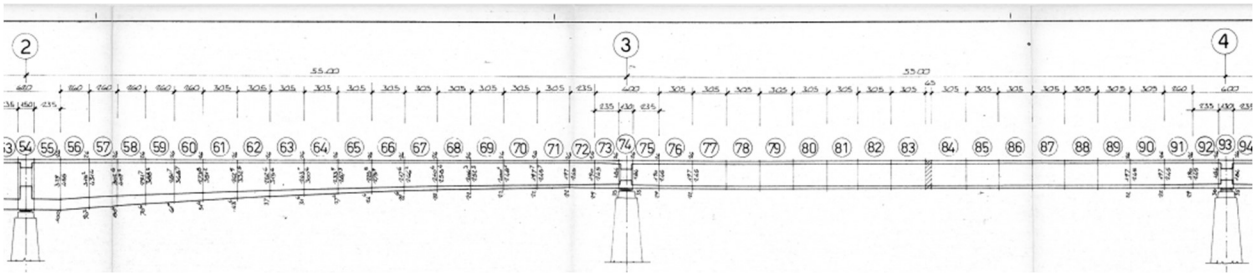


*Figure 87 pier structure discrepancies*

➢ FSM (Free Standing Midspan) Zone Requirement:

- Midas Civil necessitates the inclusion of an "FSM Zone," typically located at the very ends of the bridge. This zone acts as a buffer between segments originating from the first and last piers, and it extends to the final abutments.
- In the bridge under study, this requirement was not met on the left side of Pier 1, where there was no FSM Zone, diverging from the typical model structure.

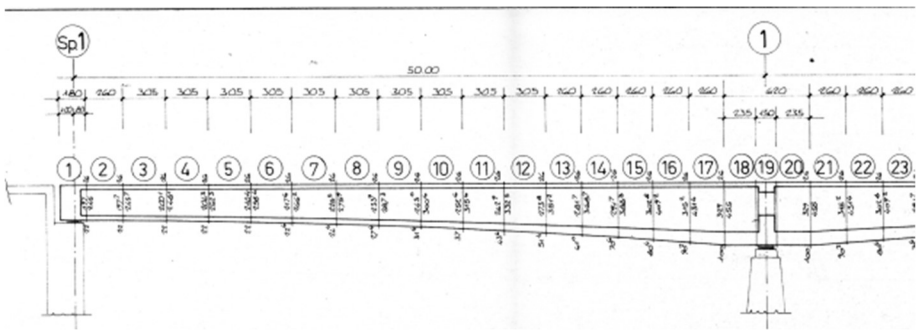


*Figure 88 FSM Zone*

➢ Lack of Data for Pier Table Placing Time:

- Another challenge arose from the absence of data concerning the pier table placement time. This temporal aspect is important for reflecting the age difference of structural elements in the analysis.
- Without this data, the software could not account for variations in the structural age, which is critical for an accurate analysis of the bridge's behavior over time.

➢ Tendon Placement at the Flange End

- The Section tab in the Midas Wizard did not provide an option for modeling a tendon at the end of the flange. However, in our bridge model, we have a tendon numbered 27 on each side of the flange. This unique configuration presented a challenge as the software did not offer a straightforward way to represent it.

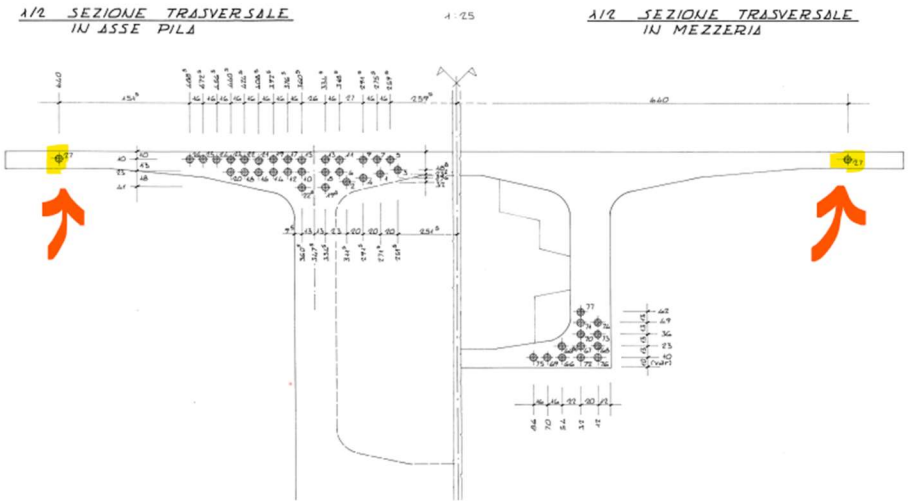


*Figure 89 Tendon placement issue*

➢ Tendon Anchorage Positions Discrepancy

- The predefined tendon anchorage positions of the software differed from the locations specified in the plans of the bridge under study. In all cases, it was necessary to manually adjust the coordinates of the anchorage positions to align with the provided plans. This misalignment between the software's default positions and the actual design introduced complexities into the modeling process.

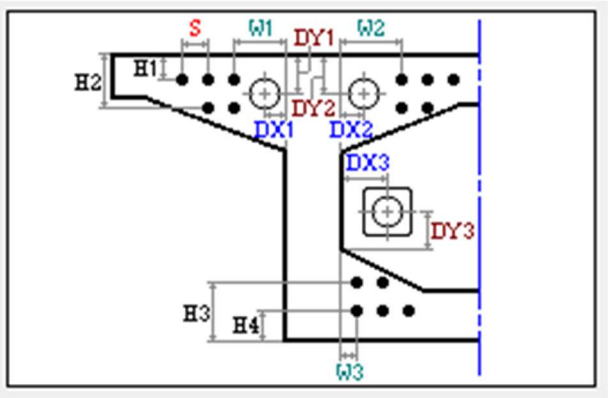


*Figure 90 Tandon anchorage positions*

➢ Web Tendons vs. Flange Tendons Ambiguïté

- The plans for the bridge design did not explicitly clarify whether the middle tendons between the outer and inner flanges should be considered as web tendons or just included with the flange tendons. This ambiguity had implications for the spacing dimensions of the tendons, making it challenging to accurately represent them in the model.

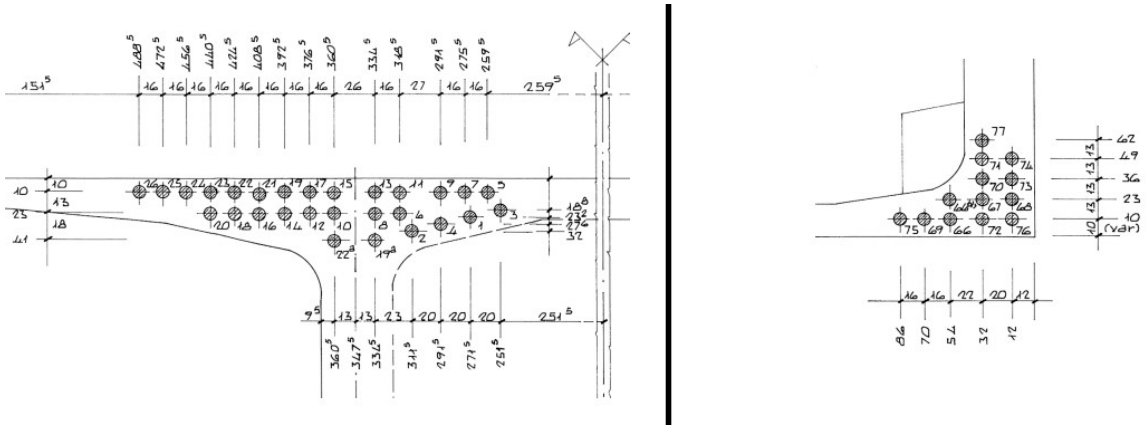

*Figure 91 Tendon Ambiguity*

➢ Limited Information on Tendon Type

- In the Tendon tab, a notable challenge was the lack of information regarding the type of steel used for the tendons. While we had data on the ultimate and yielding strength of the tendons, the specific steel type was not provided. This information is crucial for accurate material property representation in the analysis.

These challenges in the Section and Tendon tabs highlight the essential need for flexibility and customization in modeling software, especially when dealing with non-standard bridge designs. In such cases, manual adjustments become necessary to accommodate the bridge's unique characteristics. Addressing these challenges often involves finding custom solutions or workarounds to ensure that the modeling process accurately captures the intricacies of the bridge design. Ultimately, the availability of complete and relevant data is paramount for facilitating a comprehensive and accurate structural analysis. In conclusion, due to these limitations the structure had to be modelled manually.

## 4.4. Results of the Analysis

The serviceability limit states, encompass a range of conditions and phenomena that can affect the performance and longevity of a structure during its service life. These include local damages such as excessive concrete cracking, displacements, and deformations that may restrict the use or efficiency of the construction, as well as compromise its appearance. Additionally, non-structural elements, facilities, and machinery are also susceptible to displacements and deformations that could hinder their efficiency and appearance. Vibrations, fatigue damages, and corrosion are further factors considered within serviceability Limit States, as they have the potential to impact the overall functionality and durability of the construction over time.

The conventional definition of the nominal VN design life of a structure refers to the expected number of years during which the structure is anticipated to maintain specific performance levels, given that it receives the necessary maintenance. The minimum VN values required for various types of construction are provided in Table 2.4.(NTC 2018) in I, which can also serve as a basis for defining time-dependent actions.

| | TIPI DI COSTRUZIONI | Valori minimi di $V_N$ (anni) |
|---|---|---|
| 1 | Costruzioni temporanee e provvisorie | 10 |
| 2 | Costruzioni con livelli di prestazioni ordinari | 50 |
| 3 | Costruzioni con livelli di prestazioni elevati | 100 |

*Figure 92 Minimum values of the Nominal Design Life (VN) for different types of constructions* (NTC 2018)

In an effort to predict the critical failure point of the bridge, calculations were conducted to ascertain the maximum tensile strength of the concrete before structural failure occurs. The findings revealed that the concrete used in the deck construction possesses a maximum tensile strength of 4.1 MPa. Subsequently, a comprehensive study was undertaken to identify the specific stage in the structure's lifespan when it is anticipated to reach this critical point.

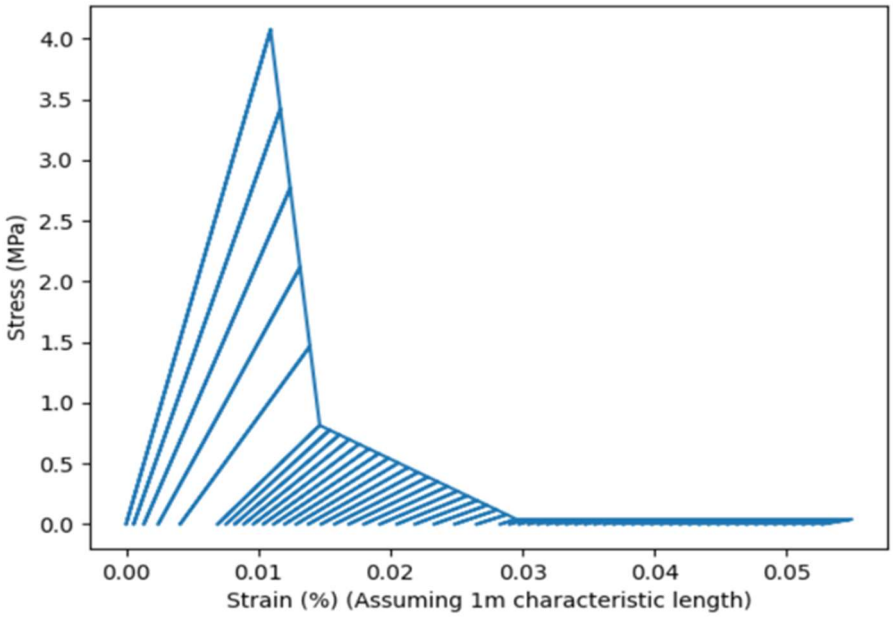


*Figure 93 stress - strain curve of the concrete used in the bridge. (tensile behavior)*

### 4.4.1. Jacking force loss

In this section, an investigation is conducted to analyze the impact of jacking force loss on the global behavior of the bridge. Specifically, the study focuses on understanding the effects of jacking force loss in all tendons, upper tendons, and lower tendons. The primary objective is to examine how these factors influence the stress distribution in the tension zone of the bottom fiber of the second span at midspan.

- Upper tendons jacking force loss.

The first study indicates that a 35% reduction in stress within the upper tendons results in failure at the bottom fiber of the midspan, reaching a final stress of 4.3 MPa. Notably, at 37.5% loss in stressing force, failure extended to the upper fiber of the concrete above the columns, concluding with a final stress of 4.1 MPa. As the stress losses were further increased, a sequence of elements also failed in the bridge, beginning with the bottom fiber of the central element of the bottom span.

| Jacking Stress Loss for Upper Tendons Only | | | |
|---|---|---|---|
| Loss | stress in tendons | stress in conc. Midspan | stress in conc. Supports |
| % | MPa | MPa | MPa |
| 10% | 1224 | -8.7 | -2.5 |
| 20% | 1088 | -6.9 | 1.9 |
| 30% | 952 | -5.3 | 3.1 |
| 35% | 884 | 4.3 | 3.7 |
| 37.5% | 850 | 4.8 | 4.1 |
| 40% | 816 | 5.2 | 4.4 |
| 45% | 748 | 5.9 | 4.9 |

*Table 4 upper tendons stress loss*

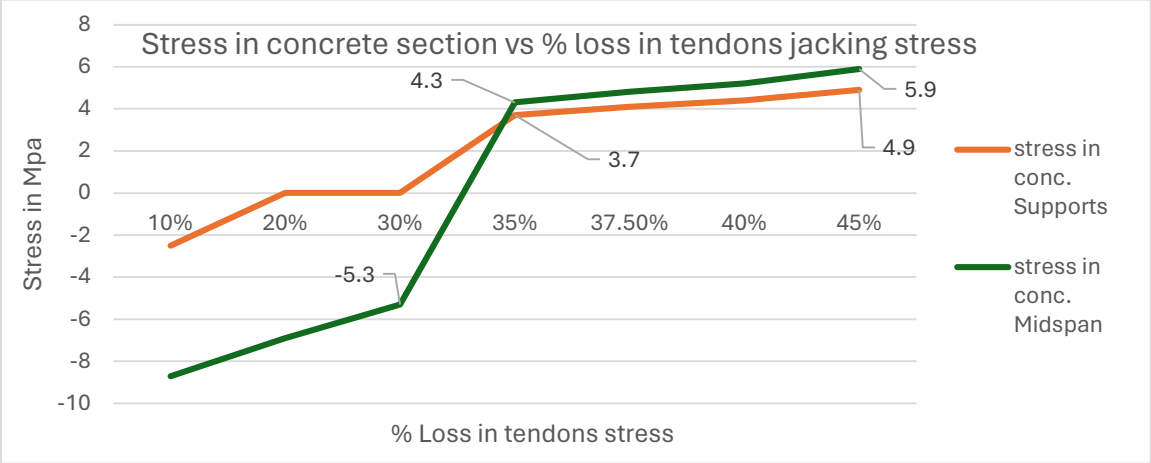


*Figure 94 upper tendons stress loss*

- Lower tendons jacking force loss.

In the second study, the reduction of jacking stress was exclusively applied to the bottom tendons. Notably, it was observed that the section managed to sustain the full load while remaining in the compression zone until a 45% loss of the initial jacking force occurred. At this juncture, the final stress in the bottom fiber peaked at 4.7 MPa. Additionally, it was noted that the upper fiber of the deck above the columns, located in the tension zone, did not experience failure.

| Jacking Stress Loss for Lower Tendons Only | | | |
|---|---|---|---|
| Loss | stress in tendons | stress in conc. Midspan | stress in conc. Supports |
| % | MPa | MPa | MPa |
| 10% | 1224 | -9 | -3.5 |
| 20% | 1088 | -7.5 | -3.3 |
| 30% | 952 | -5.9 | -3.1 |
| 35% | 884 | -5.2 | -3 |
| 37.5% | 850 | -4.7 | -2.9 |
| 40% | 816 | -4.5 | -2.9 |
| 45% | 748 | 4.7 | -2.8 |

*Table 5 lower tendons stress loss*

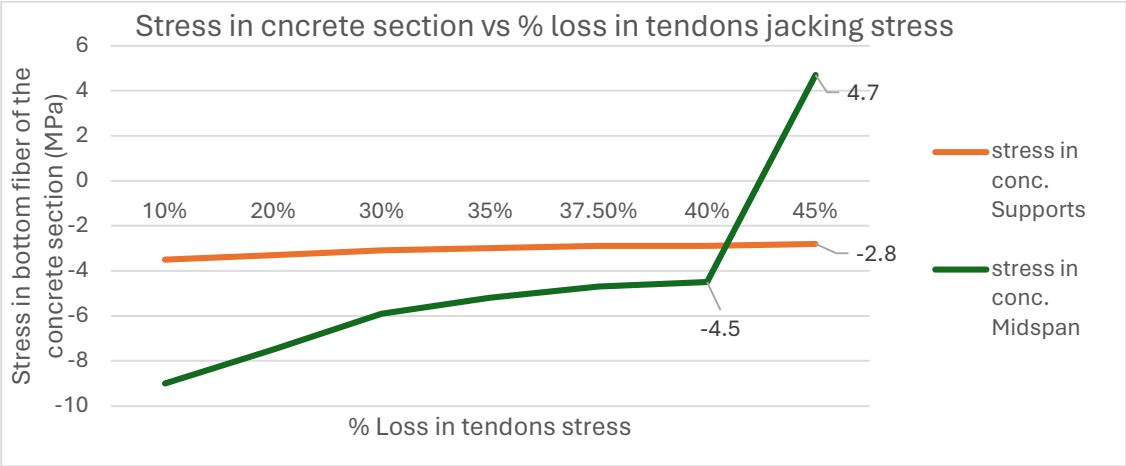


*Figure 95 Variation in the section stress with respect to tendons stress*

- All tendons jacking force loss.

In the third study, the focus was on comprehending the consequences of losing jacking force in all tendons, both upper and lower. Unexpectedly, a substantial reduction in the bridge's strength capacity was observed. Notably, the bottom fiber of the bridge experienced failure shortly after a 20% reduction in tendon stress, resulting in a stress of 4.4 MPa at the bottom fiber of the midspan of the bridge.

| Loss of Stress in All Tendons | | | |
|---|---|---|---|
| Loss | stress in tendons | stress in conc. Midspan | stress in conc. Supports |
| % | MPa | MPa | MPa |
| 10% | 1224 | -7.4 | -2.3 |
| 20% | 1088 | 4.4 | 2.3 |

*Table 6 Stress loss in all tendons*

To sum the section of this chapter a graph is constructed to integrate the findings from the initial three tests, visually presenting the evolution of stress in the bottom fiber of the midspan under three distinct conditions. The graph also clearly indicates the respective points of failure in each scenario.

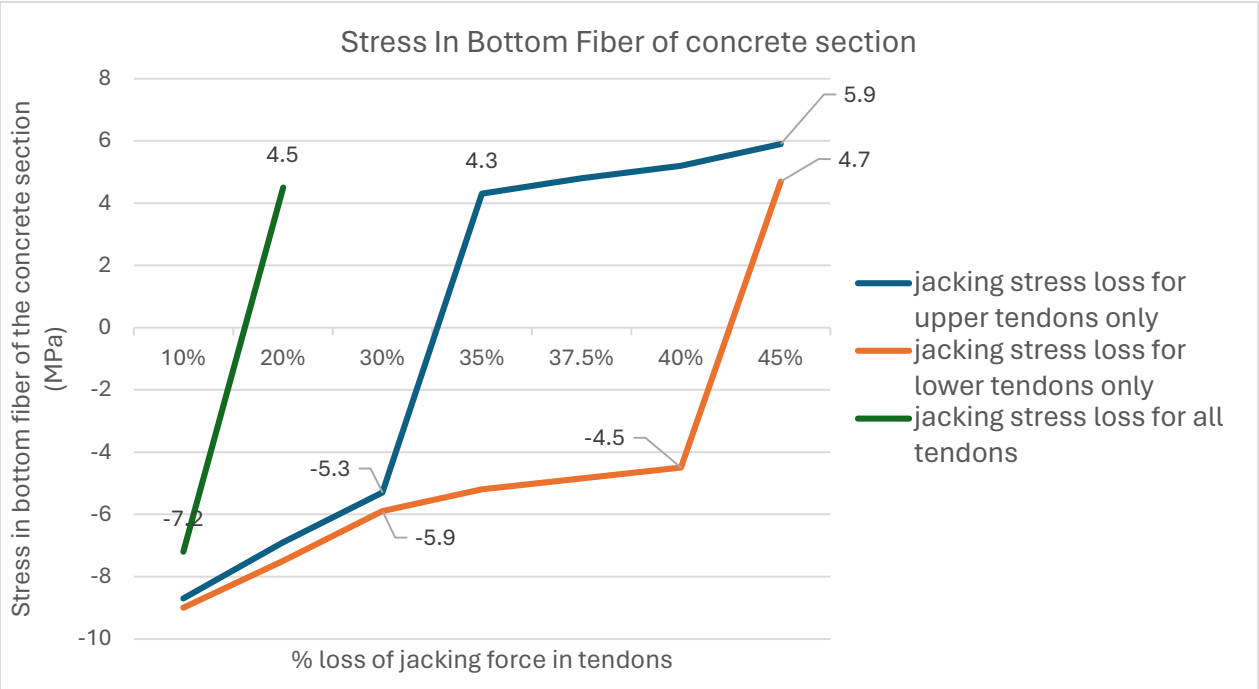


*Figure 96 Concluding stress curve*

### 4.4.2. Cross-sectional Area Loss

Following the examination of the consequences of jacking force loss on the overall behavior of the bridge, a subsequent study delved into comprehending the implications of cross-sectional area loss across all tendons. The findings revealed that a 20% area loss of the total cross-sectional area will lead to crack initiation in the bottom fiber of the midspan.

| Loss of Cross-Sectional Area: | | | |
|---|---|---|---|
| Loss | Area of tendons | stress in conc. Midspan | stress in conc. Supports |
| % | mm2 | MPa | MPa |
| 10% | 2371.5 | -7.4 | -2.3 |
| 20% | 2108 | 4.4 | 2.3 |

*Table 7 Cross sectional area loss in all tendons*

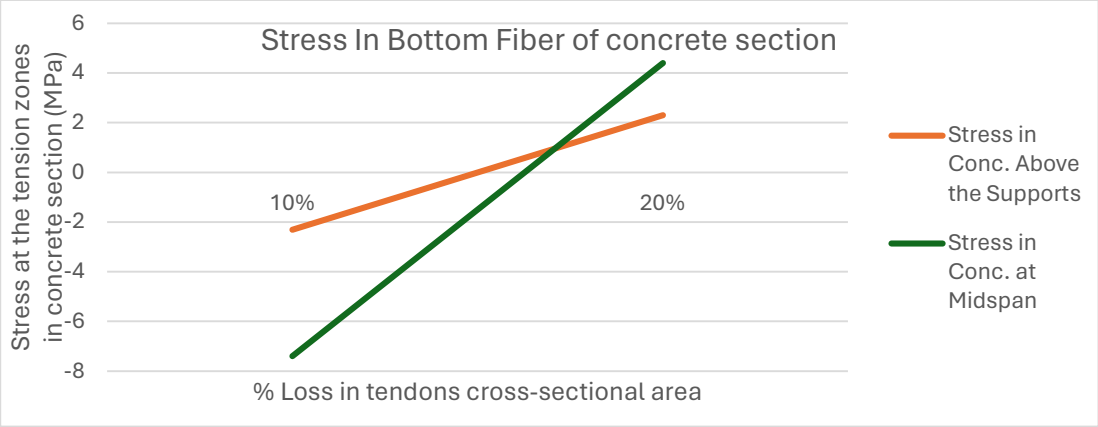


*Figure 97 variation in the section stress with respect to tendons cross sectional area*

### 4.4.3. Combined Effect

To enhance realism and simulate a scenario reflective of real-world conditions, a fifth study was undertaken. This study incorporated a combination of cross-sectional area loss and stress loss in tendons. The results revealed that a failure in the bottom fiber of the cross-section occurred with a simultaneous 4% reduction in cross-sectional area and a 16% decrease in tendon stress.

| Stress Loss in Tendons & Loss of Cross-Sectional Area | | | | |
|---|---|---|---|---|
| - | Loss | Value | stress in conc. Midspan | stress in conc. Supports |
| - | % | mm^2/ MPa | MPa | MPa |
| Area loss | 12.50% | 2305.625 | 5.6 | 2.8 |
| Stress loss | 12.50% | 1190 | | |
| Area loss | 12.50% | 2305.625 | 4.9 | 2.5 |
| Stress loss | 10.00% | 1224 | | |
| Area loss | 11.00% | 2345.15 | 4.5 | 2.3 |
| Stress loss | 10.00% | 1224 | | |
| Area loss | 10.00% | 2371.5 | -4.5 | 2.1 |
| Stress loss | 10.00% | 1224 | | |

*Table 8 combined effect on stresses in bottom fiber*

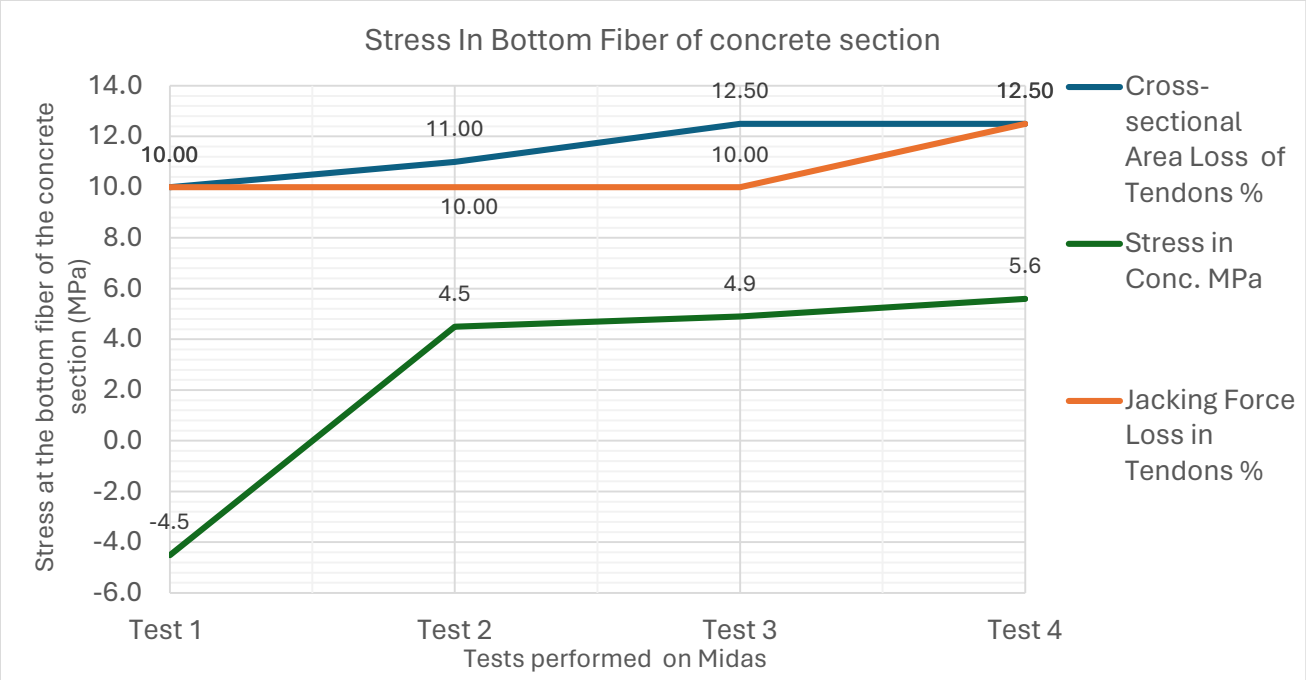


*Figure 98 Combined effect on bottom fiber stress*

## 4.5. Discussion of the Results

Upon acquiring data from Midas and documenting the instances of failure, a comprehensive study was undertaken to validate the observed losses. Predominantly, losses in tendon stress were attributed to friction losses, instantaneous losses stemming from concrete deformation, and long-term relaxation losses of the tendons. On the other hand, cross-sectional area losses were linked to corrosion.

### 4.5.1. Friction losses

In a cross-section which is at a distance "X" from a stressing anchorage. The stress $\sigma_{p_o,(x)}$ in the tendon being tensioned is lower than the stress at the anchorage point $\sigma_{p_o,(max)}$ (Taerwe and Matthys 2013). The difference between the 2 stress corresponds to the losses due to the friction:

$$P_x = P_0 e^{-\mu(\propto + Kx)}$$

Where:

- μ is the coefficient of friction between the prestressing steel and the duct. A value of 0.23 is used.
- α is the sum of the angular displacement over a distance X, irrespective of direction or sign "radians".
- K is the un-intentional angular displacement "per unit length" depending on the design layout "shape" of the tendon, stiffness of duct and spacing of duct supports "radians/m". it is also called the wobble coefficient. Because of lack of data a lower value of 0.005 radian/m is used.

| tendon nb. | Px | P0 | μ | α | k | x | % loss | Y |
|---|---|---|---|---|---|---|---|---|
| 77 | 3338.94 | 3583 | 0.23 | 0.05766 | 0.005 | 50 | 6.81 | -0.071 |
| 76 | 3358.18 | 3583 | 0.23 | 0.0326 | 0.005 | 50 | 6.27 | -0.065 |
| 75 | 3360.94 | 3583 | 0.23 | 0.02902 | 0.005 | 50 | 6.19 | -0.064 |
| 74 | 3352.10 | 3583 | 0.23 | 0.0405 | 0.005 | 50 | 6.44 | -0.067 |
| 73 | 3359.55 | 3583 | 0.23 | 0.03082 | 0.005 | 50 | 6.23 | -0.065 |
| 72 | 3370.83 | 3583 | 0.23 | 0.0162 | 0.005 | 50 | 5.92 | -0.061 |
| 71 | 3361.86 | 3583 | 0.23 | 0.02782 | 0.005 | 50 | 6.17 | -0.064 |
| 70 | 3368.76 | 3583 | 0.23 | 0.01888 | 0.005 | 50 | 5.97 | -0.062 |
| 69 | 3379.52 | 3583 | 0.23 | 0.00498 | 0.005 | 50 | 5.67 | -0.059 |
| 68 | 3378.01 | 3583 | 0.23 | 0.00692 | 0.005 | 50 | 5.72 | -0.059 |
| 67 | 3380.17 | 3583 | 0.23 | 0.00414 | 0.005 | 50 | 5.66 | -0.058 |
| 66 | 3385.80 | 3583 | 0.23 | -0.00312 | 0.005 | 50 | 5.50 | -0.057 |
| 66b | 3382.79 | 3583 | 0.23 | 0.00076 | 0.005 | 50 | 5.58 | -0.058 |

*Table 9 Friction losses in tendons*

Following the computation of friction losses for each tendon, an average value was determined and accepted as the representative friction loss, equating to 6%.

| Beam (m) | Number of steel | Tension control stress (MPa) | Distance (m) | Sag ratio (rad) | Friction loss stress (MPa) |
|---|---|---|---|---|---|
| 20 | N1 | 1337.86 | 8.625 | 0.0927 | 87.32 |
| | | 1499.29 | 5.425 | 0.0927 | 79.29 |
| | N3 | 1499.29 | 9.800 | 0.0927 | 102.86 |
| | | 1499.29 | 5.425 | 0.0927 | 85.54 |
| | N4 | 1336.14 | 9.800 | 0.0349 | 65.14 |
| 25 | N1 | 1356.07 | 9.654 | 0.0927 | 92.68 |
| | | 1315.71 | 6.453 | 0.0927 | 55.00 |
| | N3 | 1315.71 | 12.300 | 0.0927 | 130.14 |
| | | 1229.57 | 6.453 | 0.0927 | 60.57 |
| | N5 | 1232.71 | 12.300 | 0.0349 | 75.86 |
| 30 | N1 | 1427.5 | 12.080 | 0.0927 | 77.62 |
| | | 1347.86 | 9.233 | 0.0927 | 58.57 |
| | N3 | 1347.86 | 14.80 | 0.0927 | 79.4 |
| | | 1273.93 | 9.233 | 0.0927 | 96.67 |
| | N5 | 1335.57 | 14.800 | 0.0349 | 98.67 |
| 30 | N1 | 1285.43 | 12.080 | 0.0927 | 69.14 |
| | | 1404.52 | 9.233 | 0.0927 | 64.17 |
| | N3 | 1404.52 | 14.80 | 0.0927 | 82.86 |
| | | 1283.81 | 9.233 | 0.0927 | 92.14 |
| | N5 | 1311.00 | 14.800 | 0.0349 | 88.86 |

(1) Distance and sag ratio are known values, and tension control stress and friction loss stress are measured values. (2) Measured values are measured in the final stage of tension.

*Figure 99 Data Derived from Secondary Source*

Constituting a significant 6% of tendon losses, the findings prompted a thorough validation process with existing literature to ensure data accuracy and reliability. This involved cross-referencing with the results of an experimental study conducted by (Yuan et al. 2020). Upon comparison, the findings of this paper were found to be coherent and fell within an acceptable range, bolstering confidence in their validity.

### 4.5.2. Relaxation losses

For initial stress values between 70% - 80% of the tensile strength, the relaxation loss may be estimated based on an equation done by Muller, Zetter-Holm (Taerwe and Matthys 2013).

$$y = 0.6656x^{0.1901}$$

Where X is the time in hours. The final value of relaxation loss may be assumed to be reached at almost 114 years for bridges “100 years design life.”

| Tension losses in Tendons | |
|---|---|
| Time span | Tension Losses % |
| 40 years | 7.53 |
| 55 years | 8.00 |
| 114 years | 9.19 |

*Table 10 Long-term losses*

As the primary contributor to maximum stress loss in tendons, relaxation losses play a pivotal role in the evolution of structural integrity over time. Given their critical significance, it was imperative to correlate and validate these losses with existing research findings. Upon thorough examination, all findings were found to align cohesively with data extracted from (Erdélyi 1989), reinforcing the robustness and reliability of the results.

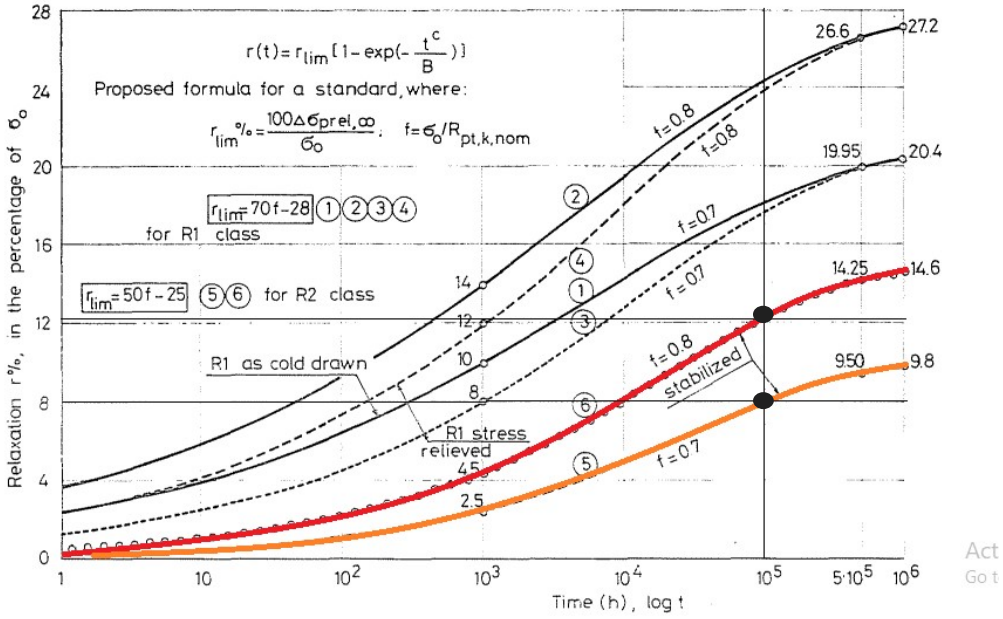


*Figure 100 Erdélyi's Relaxation Study*

### 4.5.3. Instantaneous losses due to concrete deformation.

Instantaneous losses due to concrete deformation refer to the immediate reduction in prestress force experienced by tendons in a concrete structure as a result of the instantaneous deformation of the surrounding concrete. This phenomenon is a critical consideration in prestressed concrete design and construction. As the concrete undergoes deformation, such as shrinkage or early-age loading effects, the tendons experience stress losses instantaneously. These losses can be estimated using the following equation.

- $\Delta P_{ei} = A_p * E_p * \sum(\frac{j\Delta\sigma_c(t)}{E_{cm}(t)}$
- $\Delta\sigma_c(t) = \frac{P_0}{A_c} + P_0 \int_0^L \frac{e(x)^2}{I_c * L} d_x$

| Variable | Value | Results | | |
|---|---|---|---|---|
| NB. Tendons | 24 | | **change in stress** | 1.59E+01 |
| stress | 1360 | | | |
| area | 2635 | | | |
| force | 86006400 | | **Change In Prestress** | 5.26E+06 |
| Ac | 7.50E+06 | | | |
| Ix | 1.53E+13 | | | |
| L (mm) | 1.00E+05 | | | |
| x (mm) | 5.00E+04 | | | |
| $e_{(x)}$ | 1.25E+03 | | **Percentage Loss %** | 6.11% |
| $E_p$ | 1.95E+05 | | | |
| $E_{cm}$ | 3.72E+04 | | | |
| $A_p$ | 63240 | | | |

*Table 11 instantaneous losses*

To enhance the clarity and understanding of the intricate details pertaining to tension stress losses in the tendons, a comprehensive table has been compiled to consolidate all relevant data on these losses. Additionally, a graphical representation has been incorporated to visually depict the relationship between losses and the bridge's timespan.

| Loss Type | Time (years) | Loss Amount | Cumulative Losses |
|---|---|---|---|
| Instantaneous | 0 | 6.11 % | 6.11 % |
| Friction loss | 0 | 6.01 % | 12.12 % |
| Long-term loss | 40 | 7.53 % | 19.65 % |
| Long-term loss | 55 | 8.00 % | 20.12 % |
| Long-term loss | 114 | 9.19 % | 21.31 % |

*Table 12 losses in tendon stress vs time*

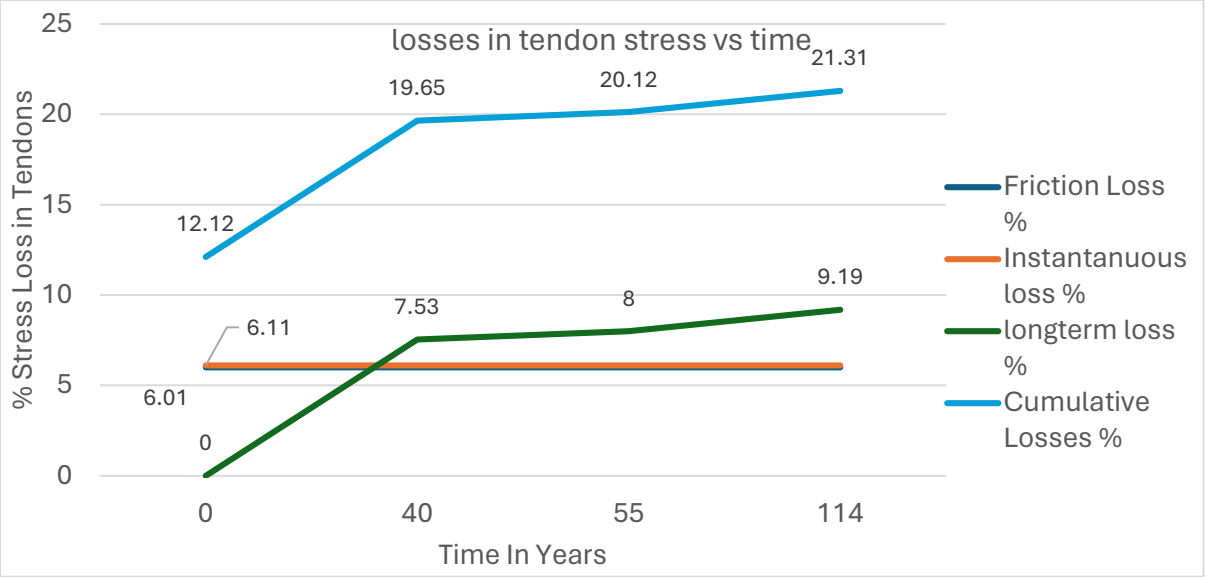


*Figure 101 losses in tendon stress vs time*

### 4.5.4. Cross-sectional Area losses due to Corrosion effects

Corrosion can decrease strand cross-sectional area, induce cover cracking, and change bond performance between strand and concrete (Cavaco, Neves, and Casas 2018). The two major types of corrosion mechanisms involved in prestressed corrosion are uniform corrosion and pitting corrosion, both invasive to the material. Uniform corrosion of iron or steel typically occurs through interactions between iron, hydrogen, and oxygen, requiring contact with moisture to sustain. The rate of uniform corrosion depends on the dissolved oxygen content in water and temperature (Miller et al. 2017)

Corrosion in steel structures is a complex process influenced by environmental factors such as moisture content and the presence of chlorides. In environments with high moisture levels, corrosion initiates when specific thresholds of oxygen and chloride concentrations are surpassed. Chlorides play a crucial role by catalyzing the binding of oxygen to iron atoms in the steel structure, leading to the formation of iron oxide, commonly known as rust, and the release of electrons.

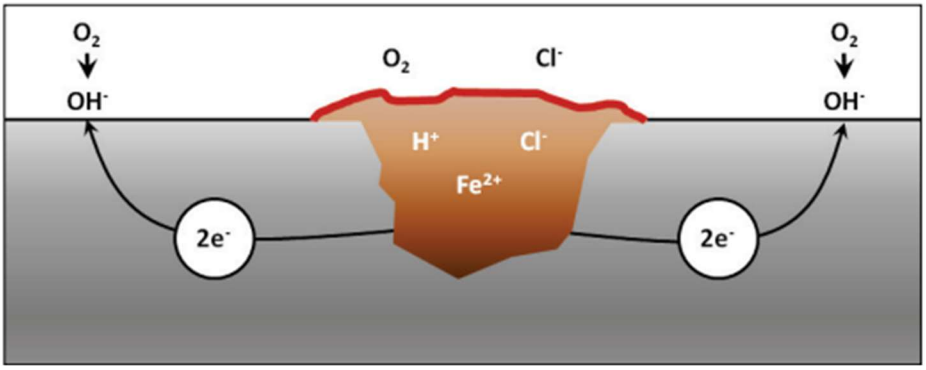


*Figure 102 The process of pitting corrosion.*(S.-K. Lee and Zielske 2014)

This electrochemical process is further facilitated by the presence of water, which provides a pathway for the flow of electrons, exacerbating the corrosion process. Moreover, steel wires are particularly susceptible to electrochemical corrosion, primarily due to the presence of carbon. This type of corrosion occurs when moisture and rainwater penetrate the steel cable, creating an environment conducive to electrochemical reactions.

Within the steel wires, micro batteries form, where carbon acts as the cathode and iron as the anode, leading to oxidation and the formation of corrosion products like ferrous hydroxide and ferric hydroxide. Additionally, pitting corrosion is a significant concern in the corrosion of bridge components, particularly post-tensioned cables(Ebeling et al. 2016). Pitting significantly diminishes the cross-sectional area of cables and alters their properties, ultimately compromising their structural integrity. (Z. Liu et al. 2020)

- Chloride Diffusion

In light of the study conducted by (Pro' 2020), comprehensive insights into chloride diffusion in concrete have been obtained. The investigation has facilitated a nuanced understanding of the time required for chloride ions to reach critical concentration levels within the concrete, posing potential risks to the oxidation of tendon steel. Notably, with a specified water-cement ratio of 0.3 and an m value rounded to 0.2, the study reveals that achieving a chloride concentration threshold of 0.15% of the concrete mass at a distance of 6.5 cm would necessitate approximately 100 years.

$$m = 2.5(^{w}/_{c}) - 0.6$$

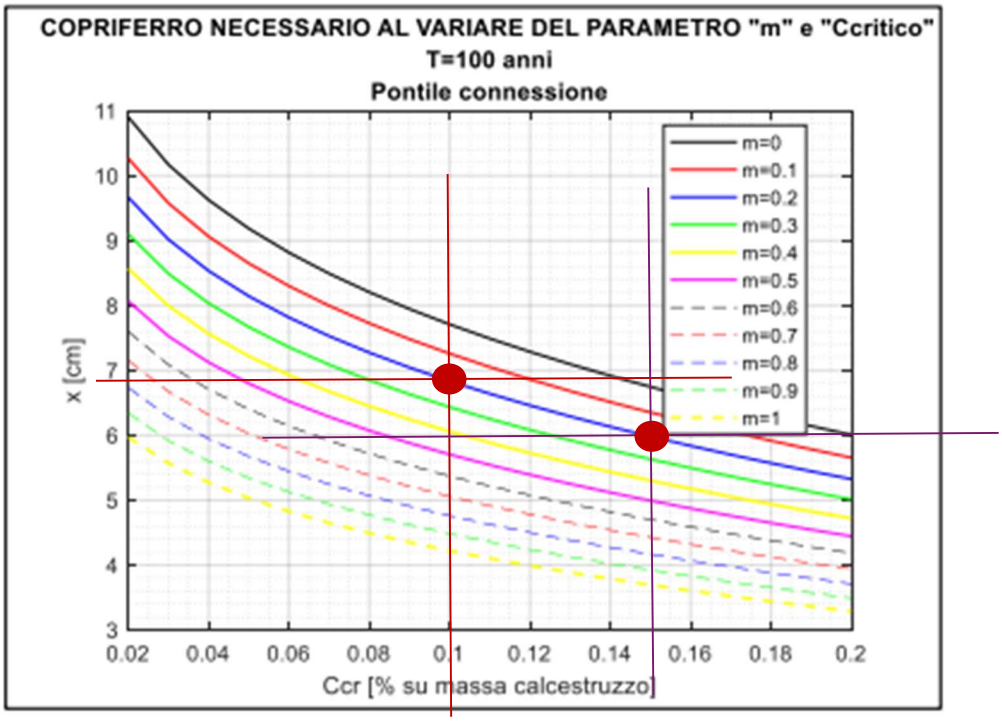


*Figure 103 minimum concrete cover required with respect to Ccr%*

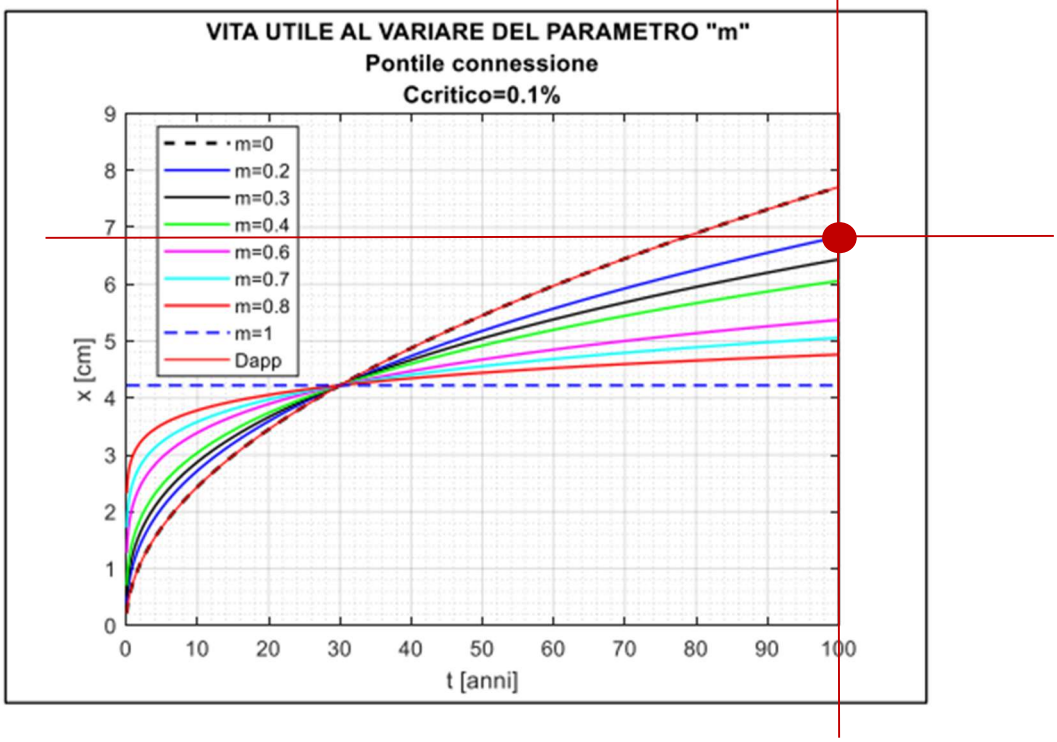


*Figure 104 Time needed for (Ccr% = 0.1) to reach a distance X in concrete.*

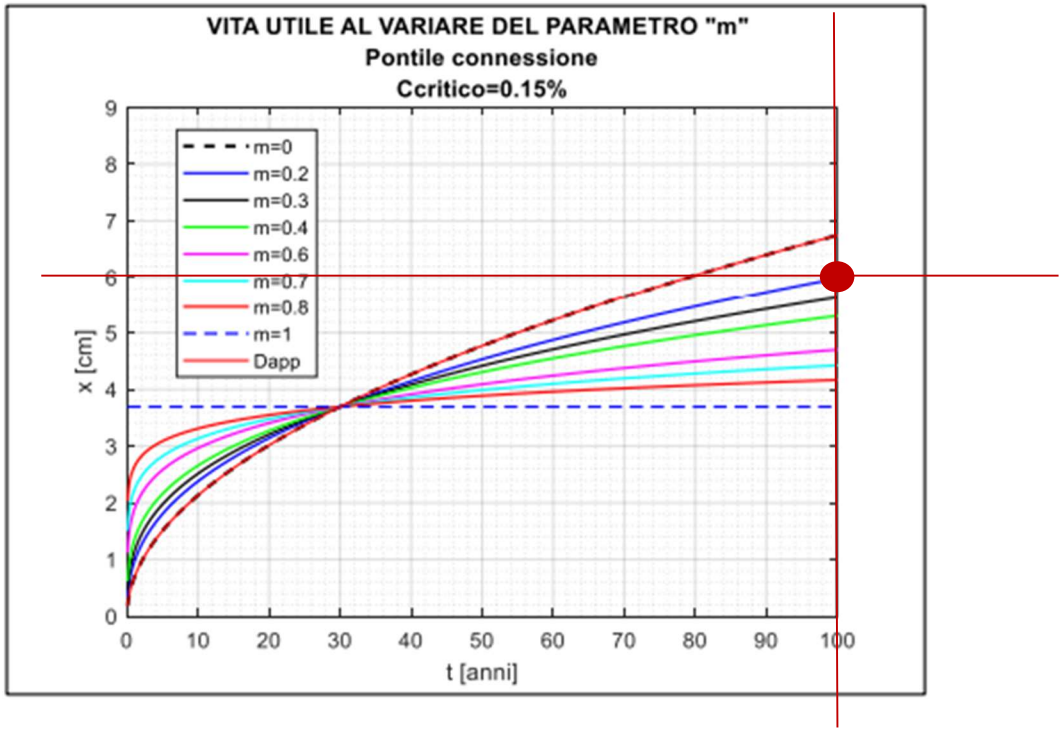


*Figure 105 Time needed for (Ccr% = 0.15) to reach a distance X in concrete*

These findings bear significance in the evaluation of the long-term durability and structural integrity of concrete elements exposed to chloride ingress. the identified chloride concentration levels, even after a century, remain within acceptable thresholds. This observation leads to a reassuring conclusion that the observed chloride diffusion is unlikely to have a deleterious impact on the serviceability life of the bridge.

➢ In Case of Execution Mistake

After reaching the conclusion that corrosion due to chloride diffusion is less likely to take place. Another study was executed to understand the possible consequences of the situation if water seeped into the ducts and corrosion started in the tendons before grouting. It is assumed that the corrosion phenomena would start on day 0.

- Pit Penetration rate.

in an attempt to estimate the time needed for corrosion to reduce the cross-sectional area of the tendons to a limit where the serviceability strength of the bridge is questioned. The pitting penetration rate had to be estimated. With reference to a study executed by (Morales et al. 2019) the parameters needed to calculate $p_{Corr}$, the corrosion penetration rate, and $p_{pit}$, the pit penetration rate, were determined. Including the α parameter which relates the homogeneous corrosion with the maximum pitting penetration as per the equation established by (Yalçyn and Ergun 1996). The study employed confidence intervals of 90%, 95%, and 99% to assess the uncertainty associated with the estimated pitting

penetration. The pitting factors (α values) corresponding to these confidence levels were determined to provide insights into the potential variations.

$$P_{corr}\,(mm/year) = 0.0116 * I_{corr}^{media}$$
$$P_{pit}(mm/year) = P_{corr}\,(mm/year) * \alpha$$

The corrosion rates $I_{Corr}^{AV}$ in the study exhibited by (Morales et al. 2019), a remarkable similarity, suggesting minimal dispersion and facilitating the derivation of a representative value. Notably, it stabilizes within the initial 24 hours of testing, remaining constant thereafter at approximately 10 µA/cm2.

| Icorr (MA/cm2) | Pcorr (mm/year) | confidence level | α | Ppit (mm/year) |
|---|---|---|---|---|
| 10 | 0.116 | 90% | 1.21 | 0.140 |
| 10 | 0.116 | 95% | 1.46 | 0.169 |
| 10 | 0.116 | 99% | 1.86 | 0.215 |

*Table 13 penetration rate*

- Critical Pit depth.

After determining the pit penetration rate per year, it was then needed to understand the pit depth required to reach the area loss that would affect the structural stability of the bridge. equations listed in chapter 2 part 2.2.7. were utilized to find the pit depth and then the correlated area loss depending on the pit type. It was noticed that for the same penetration rate the area loss varies according to the pit type.

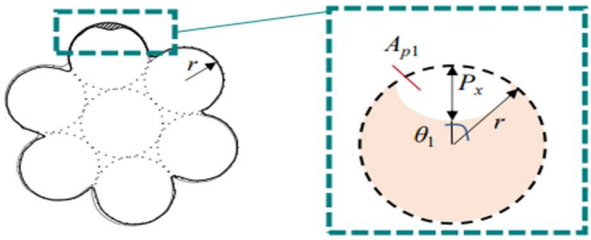


*Figure 106 Pit type 1*

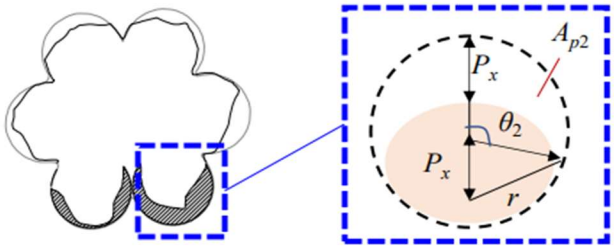


*Figure 107 Pit type 2*

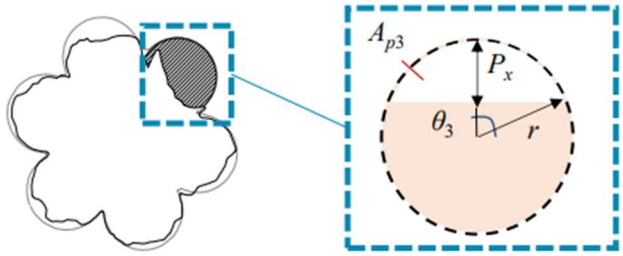


*Figure 108 Pit type 3*

| Ppit(mm/year) | Time in years | Asl1 % | Asl2 % | Asl3 % |
|---|---|---|---|---|
| 0.14036 | 0 | 0 | 0 | 0 |
| 0.14036 | 3 | 0.07 | 1.49 | 0.21 |
| 0.14036 | 6 | 0.21 | 2.88 | 0.59 |
| 0.14036 | 9 | 0.39 | 4.27 | 1.09 |
| 0.14036 | 12 | 0.59 | 5.66 | 1.67 |
| 0.14036 | 15 | 0.83 | 7.05 | 2.33 |
| 0.14036 | 18 | 1.09 | 8.44 | 3.05 |
| 0.14036 | 21 | 1.37 | 9.83 | 3.84 |
| 0.14036 | 24 | 1.67 | 11.22 | 4.68 |
| 0.14036 | 27 | 1.99 | 12.61 | 5.57 |

*Table 14 Cross-sectional area loss in % for α = 90%*

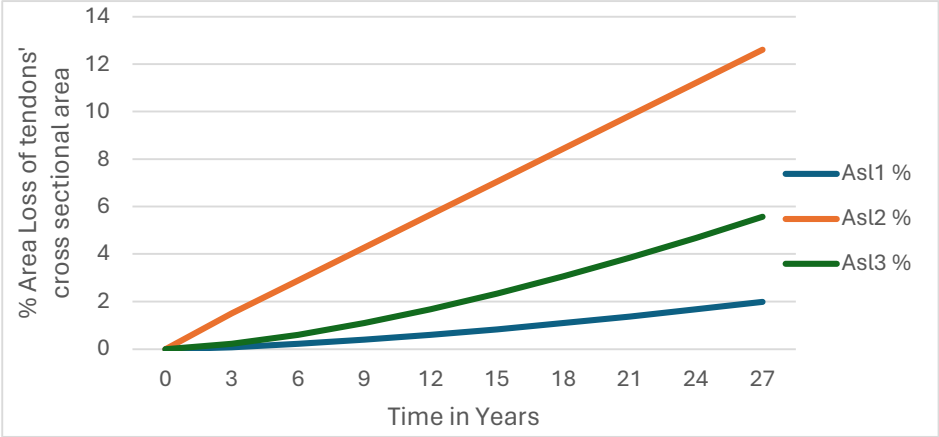


*Figure 109 Cross-sectional area loss by % for α = 90%*

With a penetration rate per year set at 0.14, the most significant area loss occurred as a result of pitting phenomenon 2. The estimation indicates a cumulative loss of 12.61% over a 27-year period. In contrast, the impact of pitting phenomenon 1 is comparatively lesser, leading to a cross-sectional area loss of only 1.99% over the same duration.

| Ppit(mm/year) | Time in years | Asl1 % | Asl2 % | Asl3 % |
|---|---|---|---|---|
| 0.16936 | 0 | 0.00 | 0.00 | 0.00 |
| 0.16936 | 3 | 0.10 | 1.78 | 0.28 |
| 0.16936 | 6 | 0.28 | 3.46 | 0.79 |
| 0.16936 | 9 | 0.51 | 5.13 | 1.44 |
| 0.16936 | 12 | 0.79 | 6.81 | 2.21 |
| 0.16936 | 15 | 1.10 | 8.49 | 3.08 |
| 0.16936 | 18 | 1.44 | 10.17 | 4.04 |
| 0.16936 | 21 | 1.81 | 11.84 | 5.07 |
| 0.16936 | 24 | 2.21 | 13.52 | 6.18 |
| 0.16936 | 27 | 2.63 | 15.19 | 7.36 |

*Table 15 Cross-sectional area loss by % for α = 95%*

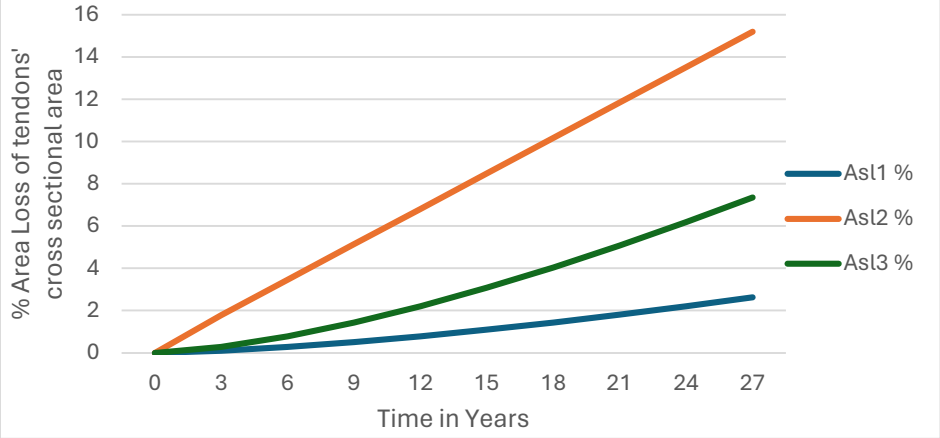


*Figure 110 Cross-sectional area loss by % for α = 95%*

With a penetration rate per year established at 0.169, the predominant area loss is attributed to pitting phenomenon 2. The estimation reveals a total loss of 15.29% over the 27-year duration. Conversely, the influence of pitting phenomenon 1 is relatively modest, resulting in a cross-sectional area loss of merely 2.63% within the same timeframe.

| Ppit(mm/year) | Time in years | Asl1 % | Asl2 % | Asl3 % |
|---|---|---|---|---|
| 0.21576 | 0 | 0 | 0.00 | 0 |
| 0.21576 | 3 | 0.14 | 2.24 | 0.40 |
| 0.21576 | 6 | 0.40 | 4.38 | 1.13 |
| 0.21576 | 9 | 0.73 | 6.51 | 2.06 |
| 0.21576 | 12 | 1.13 | 8.65 | 3.17 |
| 0.21576 | 15 | 1.57 | 10.79 | 4.41 |
| 0.21576 | 18 | 2.06 | 12.92 | 5.78 |
| 0.21576 | 21 | 2.60 | 15.06 | 7.26 |
| 0.21576 | 24 | 3.17 | 17.19 | 8.83 |
| 0.21576 | 27 | 3.77 | 19.33 | 10.50 |

*Table 16Cross-sectional area loss by % for α = 99%*

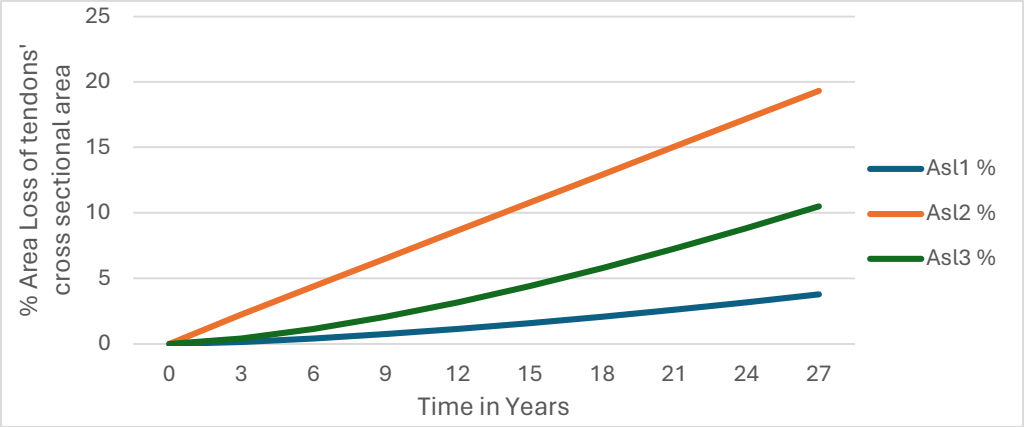


*Figure 111 Cross-sectional area loss by % for α = 99%*

At a pit penetration rate per year 0.215, once again, the primary area loss is ascribed to pitting phenomenon 2. The estimation indicates an aggregate loss of 19.33% over the 27-year period. In contrast, the impact of pitting phenomenon 1 is minimal, leading to a cross-sectional area loss of only 3.77% during the same timeframe.

Across various penetration rates per year (0.14, 0.169, and 0.215), it consistently emerges that pitting phenomenon 2 remains the primary contributor to substantial area loss. With an increasing confidence factor, the projected cumulative losses over a 27-year period escalate: 12.61%, 15.29%, and 19.33%, respectively. Conversely, the impact of pitting phenomenon 1 is comparatively subdued, ranging from 1.99% to 3.77% across the three confidence factors. This observed pattern underscores the sustained influence of pitting phenomenon 2 on cross-sectional area loss, highlighting its growing significance as confidence factors rise.

However, given that the bridge is already 30 years old without evident cracks on its outer surface, values associated with phenomenon 1 will be prioritized for estimating final stresses in the bridge's bottom fibre in the event of losses.

| Time in Years | Corrosion loss % Area | Loss (long-term) % | Friction loss % | Instantaneous loss % | Stress in Bottom fiber MPa |
|---|---|---|---|---|---|
| 0 | 0.00 | 0.00 | 6.01 | 6.11 | -7.60 |
| 3 | 0.07 | 4.61 | 6.01 | 6.11 | -5.4 |
| 6 | 0.21 | 5.26 | 6.01 | 6.11 | -5.2 |
| 9 | 0.39 | 5.68 | 6.01 | 6.11 | -5 |
| 12 | 0.59 | 6.00 | 6.01 | 6.11 | -4.9 |
| 15 | 0.83 | 6.26 | 6.01 | 6.11 | -4.8 |
| 18 | 1.09 | 6.48 | 6.01 | 6.11 | -4.6 |
| 21 | 1.37 | 6.67 | 6.01 | 6.11 | -4.5 |
| 24 | 1.67 | 6.84 | 6.01 | 6.11 | -4.4 |
| 27 | 1.99 | 6.99 | 6.01 | 6.11 | -4.4 |
| 30 | 2.33 | 7.14 | 6.01 | 6.11 | 5.1 |
| 33 | 2.68 | 7.27 | 6.01 | 6.11 | 5.3 |
| 36 | 3.05 | 7.39 | 6.01 | 6.11 | 5.5 |

*Table 17 final stress in bottom fiber in case of corrosion*

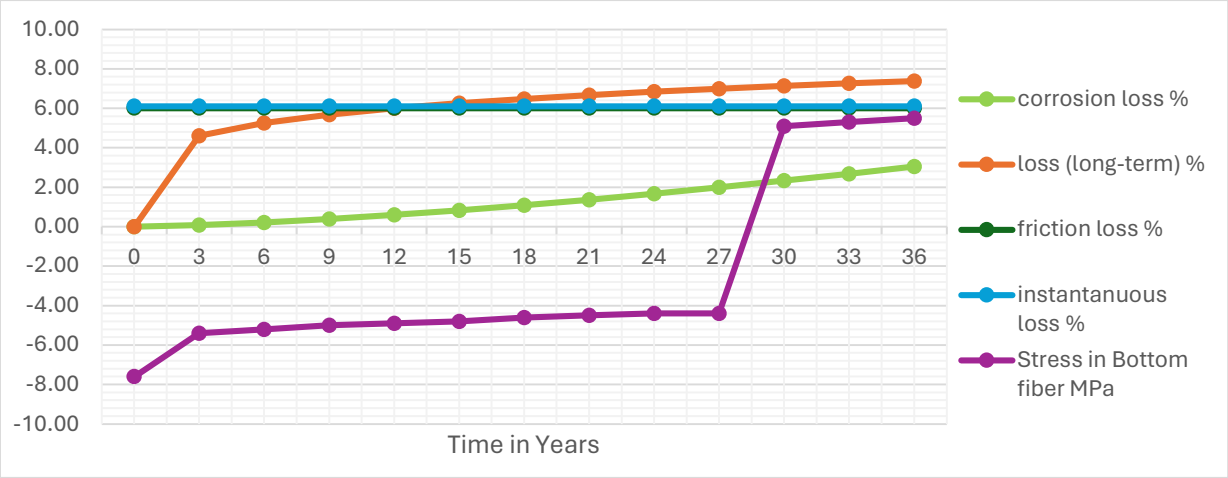


*Figure 112 final stress in bottom fiber in case of corrosion*

It became apparent that the cumulative effect of all losses would compromise the serviceability condition of the bridge after 29 years. Drawing this inference allows us to presume the absence of construction-related execution defects concerning the oxidation phenomenon at the time of the bridge's construction.

## 4.6. Key findings:

- A flawless execution, devoid of any defects, suggests that the bridge is poised to fulfill its intended serviceability life of 50 years.
- In instances of execution defects allowing water ingress into the ducts before grouting, an analysis has determined that cracks may emerge at the bottom fiber of the midspan after 29 years. This occurs due to cumulative stress, surpassing the maximum bearable tension stress of 4.1 MPa.

- Despite the bridge being constructed 30 years ago, the absence of visible cracks in the bottom fiber implies a potential absence of tendon corrosion. However, for definitive confirmation, a thorough field investigation is recommended.
- The initiation of corrosion through the chloride diffusion phenomenon is unlikely, as the required chloride concentration and tendon depth indicate that it would take more than 100 years for such corrosion to commence.

# 5. Conclusion

In conclusion, this study has conducted a comprehensive analysis of the short-term and long-term losses experienced by the post-tension system throughout the lifespan of the bridge under study. Based on our findings, we project that the bridge will maintain its serviceability for its entire design life of 50 years. Our research underscores the significant impact of friction, instantaneous, and long-term losses on the structural integrity of the bridge. Adherence to the recommendations provided by researchers regarding minimum concrete cover can effectively prevent chloride diffusion, thus ensuring the structural durability of the bridge. The absence of visible cracks on the outer surface of the bridge, even after 30 years since construction, suggests the absence of significant execution mistakes during construction. Additionally, our study indicates that if pitting were to occur, cracking would typically initiate after approximately 29 years, further supporting the absence of execution errors. Furthermore, our findings corroborate existing literature regarding failure times due to tendon damage, thereby enhancing our understanding of structural vulnerabilities and informing maintenance practices for prolonged bridge longevity.

Following extensive investigations and analysis, researchers have unveiled crucial insights into the prevalent locations and timing of bridge failures. Moreover, their scrutiny extends to identifying warning signs indicative of potential bridge failures. Building upon these findings, the researchers have meticulously crafted recommendations for tailored maintenance interventions. These recommendations are tailored to the specific condition of the bridge, ensuring the preservation of its structural health and integrity.

The utilization of the free cantilevered construction method in bridge construction offers notable advantages by minimizing the use of supports. However, it is imperative for designers to remain vigilant throughout the construction process, given the dynamic changes in structural behavior. Designers must carefully manage evolving stress distribution, both during and after construction, to ensure the ongoing structural integrity of the bridge.

Lastly, the incorporation of bridge curvatures introduces an enhanced torsional effect on the structure, necessitating meticulous consideration during the design phase. This effect influences not only torsional stresses but also other structural aspects. Given the critical importance of design integrity, inspectors must pay close attention to potential errors during the inspection process, as design flaws are among the primary causes of bridge failures. By prioritizing thorough inspections and promptly addressing design errors, engineers can ensure optimal performance, longevity, and safety of bridge structures.

# 6. Reference


Atamturktur, S, F M Hemez, and J A Laman. 2012. “Uncertainty Quantification in Model Verification and Validation as Applied to Large Scale Historic Masonry Monuments.” *Engineering Structures* 43: 221–34.

Azizinamini, Atorod, and Jawad Gull. 2012. “Improved Inspection Techniques for Steel Prestressing/Post-Tensioning Strand: Volume I.”

Blitz, Jack, and Geoff Simpson. 1995. *Ultrasonic Methods of Non-Destructive Testing*. Vol. 2. Springer Science & Business Media.

Carsana, Maddalena, and Luca Bertolini. 2015. “Corrosion Failure of Post-Tensioning Tendons in Alkaline and Chloride-Free Segregated Grout: A Case Study.” *Structure and Infrastructure Engineering* 11 (3): 402–11. https://doi.org/10.1080/15732479.2014.887736.

Cavaco, Eduardo S, Luis A C Neves, and Joan R Casas. 2018. “On the Robustness to Corrosion in the Life Cycle Assessment of an Existing Reinforced Concrete Bridge.” *Structure and Infrastructure Engineering* 14 (2): 137–50.

Celaya, Manuel, Parisa Shokouhi, and Soheil Nazarian. 2007. “Assessment of Debonding in Concrete Slabs Using Seismic Methods.” *Transportation Research Record* 2016 (1): 65–75.

Choudhury, Jamilur, and Ariful Hasnat. 2015. *Bridge Collapses around the World: Causes and Mechanisms*.

DaSilva, Marcelo, Saeed Javidi, Aaron Yakel, and Atorod Azizinamini. 2009. “Nondestructive Method to Detect Corrosion of Steel Elements in Concrete.”

Derobert, X, C Aubagnac, and O Abraham. 2002. “Comparison of NDT Techniques on a Post-Tensioned Beam before Its Autopsy.” *NDT & E International* 35 (8): 541–48.

DING, Dajun. 1990. “Calculation for Deflection of Continuous Reinforced Concrete Beams in Consideration of Moment Redistribution.” *Doboku Gakkai Ronbunshu* 1990 (416): 25–36.

Ebeling, Robert M, Barry C White, James A Evans, Richard W Haskins, and Ernest L Miller. 2016. *Corrosion Induced Loss of Capacity of Post-Tensioned Seven Wire Strand Cable Used in Multistrand Anchor Systems Installed at Corps Projects*. US Army Engineer Research and Development Center, Information Technology ….

Erdélyi, Attila. 1989. “Estimating the Relaxation of Prestressing Tendons.” *Periodica Polytechnica Civil Engineering* 33 (1–2): 19–32.

Ghorbanpoor, Alireza, R Borchelt, M Edwards, and E Abdel Salam. 2000. “Magnetic-Based NDE of Prestressed and Post-Tensioned Concrete Members: The MFL System.”

Harris, DMJM. 2003. “Test and Assessment of NDT Methods for Post-Tensioning Systems in Segmental Balanced Cantilever Concrete Bridges.” *Tallahassee, FL, Florida Department of Transportation*, 3–215.

Hillemeier, B, and H Scheel. 1998. “Magnetic Detection of Prestressing Steel Fractures in Prestressed Concrete.” *Materials and Corrosion* 49 (11): 799–804.

Hurlebaus, Stefan, Mary Beth Hueste, Madhu Karthik, and Tevfik Terzioglu. 2016. *Condition Assessment of Bridge Post-Tensioning and Stay Cable Systems Using NDE Methods*.

Hutchinson, Peter J, and P G Bryan Teschke. n.d. “Ground Penetrating Radar as a Sentinel Device.”

Im, Seok Been, and Stefan Hurlebaus. 2012. “Non-Destructive Testing Methods to Identify Voids in External Post-Tensioned Tendons.” *KSCE Journal of Civil Engineering* 16: 388–97.

Jagannadha Rao, Kodukula. 2018. “Acid Resistance of Quaternary Blended Recycled Aggregate Concrete.” *Case Studies in Construction Materials* 8 (March). https://doi.org/10.1016/j.cscm.2018.03.005.

Jeon, Chi-Ho, Jae-Bin Lee, Sokanya Lon, and Chang-Su Shim. 2019. “Equivalent Material Model of Corroded Prestressing Steel Strand.” *Journal of Materials Research and Technology* 8 (2): 2450–60. https://doi.org/https://doi.org/10.1016/j.jmrt.2019.02.010.

Jeon, Chi-Ho, Cuong Duy Nguyen, and Chang-Su Shim. 2020. “Assessment of Mechanical Properties of Corroded Prestressing Strands.” *Applied Sciences* 10 (12): 4055.

Krause, Martin, Klaus Mayer, Martin Friese, Boris Milmann, Frank Mielentz, and Gregor Ballier. 2011. “Progress in Ultrasonic Tendon Duct Imaging.” *European Journal of Environmental and Civil Engineering* 15 (4): 461–85.

Law, D W, S G Millard, and J H Bungey. 2000. “Linear Polarisation Resistance Measurements Using a Potentiostatically Controlled Guard Ring.” *NDT & E International* 33 (1): 15–21.

Lee, George C, Satish Mohan, Chao Huang, and Bastam N Fard. 2013. *A Study of US Bridge Failures (1980-2012)*. MCEER Buffalo, NY.

Lee, Seung-Kyoung, and James Zielske. 2014. “An FHWA Special Study: Post-Tensioning Tendon Grout Chloride Thresholds.”

Lin, Xiaosong, Zhouhong Zong, and Jie Niu. 2015. “Finite Element Model Validation of Bridge Based on Structural Health Monitoring—Part II: Uncertainty Propagation and Model Validation.” *Journal of Traffic and Transportation Engineering (English Edition)* 2 (4): 279–89.

Liu, Wei, Robert Hunsperger, Michael Chajes, and Eric Kunz. 2001. “An Overview of Corrosion Damage Detection in Steel Bridge Strands Using TDR.” In *Proc., 2nd Int. Symp. on TDR for Innovative Applications*, 1–9. Northwestern University Evanston, Ill.

Liu, Zhongxiang, Tong Guo, Daguang Han, and Aiqun Li. 2020. “Experimental Study on Corrosion-Fretting Fatigue Behavior of Bridge Cable Wires.” *Journal of Bridge Engineering* 25 (12): 04020104.

Mairone, Mattia, Rebecca Asso, Davide Masera, and Pietro Palumbo. 2022. “Behaviour and Analysis of Horizontally Curved Steel Box-Girder Bridges.” *Open Journal of Civil Engineering* 12 (3): 390–414.

Martin, J, K J Broughton, A Giannopolous, M S A Hardy, and M C Forde. 2001. “Ultrasonic Tomography of Grouted Duct Post-Tensioned Reinforced Concrete Bridge Beams.” *Ndt & E International* 34 (2): 107–13.

Matos, Arthur Resende, MecRoc Engenharia, Alexandre Assunção Gontijo, Leandro Roque Fonseca, Gustavo Antônio Pereira Batista, AngloGold Ashanti, and Gérson Rincon Ribeiro. n.d. “Detailing the Use and Installation of the Time Domain Reflectometer in Geomechanics Monitoring.”

Menga, Antonia, Terje Kanstad, and Daniel Cantero. 2022. “Corrosion Induced Failures of Post-Tensioned Bridges.”

Menga, Antonia, Terje Kanstad, Daniel Cantero, Lise Bathen, Karla Hornbostel, and Anja Klausen. 2023. “Corrosion-Induced Damages and Failures of Posttensioned Bridges: A Literature Review.” *Structural Concrete* 24 (1): 84–99. https://doi.org/https://doi.org/10.1002/suco.202200297.

Miller, Ernest L, Barry C White, Richard W Haskins, Robert M Ebeling, and James A Evans. 2017. “An Investigation of Corrosion Mitigation Strategies for Aging Post-Tensioned Cables.”

NTC. 2018. “Norme Tecniche per Le Costruzioni (NTC 2018).” *Ministerial Decree DM 17 Gennaio 2018 “Aggiornamento Delle Norme Tecniche per Le Costruzioni.”*

Morales, Juan A, Julio Torres, Nuria Rebolledo, and Javier Sánchez. 2019. “Experimental and Statistical Analysis of the Corrosion in Tendons in Contact with Water.” *Frontiers in Materials* 6: 167.

Morgese, Maurizio, Farhad Ansari, Marco Domaneschi, and Gian Paolo Cimellaro. 2020. “Post-Collapse Analysis of Morandi’s Polcevera Viaduct in Genoa Italy.” *Journal of Civil Structural Health Monitoring* 10: 69–85.

Myakushev, Konstantin, Dmitry Slesarev, Dmitry Sukhorukov, and Intron Plus. 2018. “Magnetic Flux Leakage (MFL) Method for Nondestructive Testing of Pre-Stressed Steel Reinforcement Strands.” In *12th European Conference on Non-Destructive Testing (ECNDT 2018), Gothenburg*, 11–15.

Pavlakovic, Brian, Mike Lowe, David Alleyne, and Peter Cawley. 1997. “Disperse: A General Purpose Program for Creating Dispersion Curves.” *Review of Progress in Quantitative Nondestructive Evaluation: Volume 16A*, 185–92.

Pollock, David G, Kenneth J Dupuis, Benjamin Lacour, and Karl R Olsen. 2008. “Detection of Voids in Prestressed Concrete Bridges Using Thermal Imaging and Ground-Penetrating Radar.” *Washington State Transportation Center (TRAC)*.

Pro’, Giosuele. 2020. “Degrado Delle Opere Portuali in C.A & C.A.P Bacino Alti Fondali: Porto Di Manfredonia.” Edited by Degrado delle opere portuali in C A & C A P Bacino alti fondali: porto di Manfredonia. *Corso Di Laurea Magistrale in Ingegneria Civile*.

Sankararaman, Shankar, You Ling, and Sankaran Mahadevan. 2011. “Uncertainty Quantification and Model Validation of Fatigue Crack Growth Prediction.” *Engineering Fracture Mechanics* 78 (7): 1487–1504. https://doi.org/https://doi.org/10.1016/j.engfracmech.2011.02.017.

Santarsiero, Giuseppe, Angelo Masi, Valentina Picciano, and Andrea Digrisolo. 2021. “The Italian Guidelines on Risk Classification and Management of Bridges: Applications and Remarks on Large Scale Risk Assessments.” *Infrastructures* 6 (8): 111.

Siang, T W, M Firdaus Akbar, G Nihad Jawad, T S Yee, and M I S Mohd Sazali. 2021. “A Past, Present, and Prospective Review on Microwave Nondestructive Evaluation of Composite Coatings. Coatings 2021, 11, 913.” s Note: MDPI stays neutral with regard to jurisdictional claims in published ….

Streicher, Doreen, Daniel Algernon, Jens Wöstmann, Matthias Behrens, and Herbert Wiggenhauser. 2006. “Automated NDE of Post-Tensioned Concrete Bridges Using Imaging Echo Methods.” In *Proceedings of the 9th European Conference on NDT*, 25–29. DGZfP Berlin.

Taerwe, Luc, and Stijn Matthys. 2013. “Fib Model Code for Concrete Structures 2010.” Ernst & Sohn, Wiley.

Thacker, Ben H, Scott W Doebling, Francois M Hemez, Mark C Anderson, Jason E Pepin, and Edward A Rodriguez. 2004. “Concepts of Model Verification and Validation.”

Tinkey, Yajai, and Larry D Olson. 2008. “Applications and Limitations of Impact Echo Scanning for Void Detection in Posttensioned Bridge Ducts.” *Transportation Research Record* 2070 (1): 8–12.

Velu, Saraswathy. 2007. “Corrosion Monitoring of Reinforced Concrete Structures - A Review.” *International Journal of Electrochemical Science*, January.

Vrablik, Lukas, Zdenek Matous, and Vladimir Kristek. 2013. “Increasing of Deflection of Prestressed Concrete Structures Due to Incorrect and Harmful Tendon Layout.”

Wang, Lei, Lizhao Dai, Hanbing Bian, Yafei Ma, and Jianren Zhang. 2019. “Concrete Cracking Prediction under Combined Prestress and Strand Corrosion.” *Structure and Infrastructure Engineering* 15 (3): 285–95.

Yalçyn, H, and M Ergun. 1996. “The Prediction of Corrosion Rates of Reinforcing Steels in Concrete.” *Cement and Concrete Research* 26 (10): 1593–99. https://doi.org/https://doi.org/10.1016/0008-8846(96)00139-1.

Yuan, Haoyun, Yuan Li, Bin Zhou, Shuanhai He, and Peizhi Wang. 2020. “Friction Characteristics of Post-Tensioned Tendons of Full-Scale Structures Based on Site Tests.” *Advances in Civil Engineering* 2020.

Zaki, Ahmad, and Zainah Ibrahim. 2021. “Corrosion Assessment of Pre-Corrosion Concrete Specimens Using Acoustic Emission Technique,” April.

# 7. Appendix

| Number of spans. | Tendon number | Location of Tendon | Starting point | Ending point |
|---|---|---|---|---|
| 1st span | 1st & 2nd (a) | upper | Peer 1 | 2nd segment towards sp1 |
| 1st span | 3rd & 4th (a) | Upper | Peer1 | 3rd segment towards sp1 |
| 1st span | 5th & 6th (a) | Upper | Peer1 | 4th segment towards sp1 |
| 1st span | 7th & 8th (a) | Upper | Peer1 | 5th segment towards sp1 |
| 1st span | 9th & 10th (a) | Upper | Peer1 | 6th segment towards sp1 |
| 1st span | 11th & 12th (a) | Upper | Peer1 | 7th segment towards sp1 |
| 1st span | 13th & 14th (a) | Upper | Peer1 | 8th segment towards sp1 |
| 1st span | 15th & 16th (a) | Upper | Peer1 | 9th segment towards sp1 |
| 1st span | 17th & 18th (a) | Upper | Peer1 | 10th segment towards sp1 |
| 1st span | 19th & 19ath (a) | Upper | Peer1 | 11th segment towards sp1 |
| 1st span | 20th & 21fst (a) | Upper | Peer1 | 12th segment towards sp1 |
| 1st span | 22nd & 22and (a) | Upper | Peer1 | 13th segment towards sp1 |
| 1st span | 23rd (a) | Upper | Peer1 | 14th segment towards sp1 |
| 1st span | 24th (a) | Upper | Peer1 | 15th segment towards sp1 |
| 1st span | 25th (a) | Upper | Peer1 | 16th segment towards sp1 |
| 1st span | 26th (a) | Upper | Peer1 | 17th segment towards sp1 |
| 1st span | 65tha | Bottom | Abutment Sp1 | 15th segment toward peer 1 |
| 1st span | 65th | Bottom | Abutment Sp1 | 14th segment toward peer 1 |
| 1st span | 64th | Bottom | Abutment Sp1 | 13th segment toward peer 1 |
| 1st span | 63rd | Bottom | Abutment Sp1 | 12th segment toward peer 1 |

| | | | | |
|---|---|---|---|---|
| 1st span | 62nd | Bottom | Abutment Sp1 | 11th segment toward peer 1 |
| 1st span | 61st | Bottom | Abutment Sp1 | 10th segment toward peer 1 |

*Table 18 tendons layout of span 1*

| Number of span. | Tendon number | Location of Tendon | Starting point | Ending point |
|---|---|---|---|---|
| 2nd span | 1st & 2nd (a) | upper | Peer 1 | 2nd segment towards peer 2 |
| 2nd span | 3rd & 4th (a) | Upper | Peer1 | 3rd segment towards peer 2 |
| 2nd span | 5th & 6th (a) | Upper | Peer1 | 4th segment towards peer 2 |
| 2nd span | 7th & 8th (a) | Upper | Peer1 | 5th segment towards peer 2 |
| 2nd span | 9th & 10th (a) | Upper | Peer1 | 6th segment towards peer 2 |
| 2nd span | 11th & 12th (a) | Upper | Peer1 | 7th segment towards peer 2 |
| 2nd span | 13th & 14th (a) | Upper | Peer1 | 8th segment towards peer 2 |
| 2nd span | 15th & 16th (a) | Upper | Peer1 | 9th segment towards peer 2 |
| 2nd span | 17th & 18th (a) | Upper | Peer1 | 10th segment towards peer 2 |
| 2nd span | 19th & 19ath (a) | Upper | Peer1 | 11th segment towards peer 2 |
| 2nd span | 20th & 21fst (a) | Upper | Peer1 | 12th segment towards peer 2 |
| 2nd span | 22nd & 22and (a) | Upper | Peer1 | 13th segment towards peer 2 |
| 2nd span | 23rd (a) | Upper | Peer1 | 14th segment towards peer 2 |
| 2nd span | 24th (a) | Upper | Peer1 | 15th segment towards peer 2 |
| 2nd span | 25th (a) | Upper | Peer1 | 16th segment towards peer 2 |
| 2nd span | 26th (a) | Upper | Peer1 | 17th segment towards peer 2 |
| 2nd span | 77th | Bottom | 4th segment after peer 1 | 4th segment before peer 2 |
| 2nd span | 76th | Bottom | 5h segment after peer 1 | 5th segment before peer 2 |

| | | | | |
|---|---|---|---|---|
| 2nd span | 75th | Bottom | 6th segment after peer 1 | 6th segment before peer 2 |
| 2nd span | 74th | Bottom | 7th segment after peer 1 | 7th segment before peer 2 |
| 2nd span | 73rd | Bottom | 8th segment after peer 1 | 8th segment before peer 2 |
| 2nd span | 72nd | Bottom | 9th segment after peer 1 | 9th segment before peer 2 |
| 2nd span | 71st | Bottom | 10th segment after peer 1 | 10th segment before peer 2 |
| 2nd span | 70th | Bottom | 11th segment after peer 1 | 11th segment before peer 2 |
| 2nd span | 69th | Bottom | 12th segment after peer 1 | 12th segment before peer 2 |
| 2nd span | 68th | Bottom | 13th segment after peer 1 | 13th segment before peer 2 |
| 2nd span | 67th | Bottom | 14th segment after peer 1 | 14th segment before peer 2 |
| 2nd span | 66th | Bottom | 15th segment after peer 1 | 15th segment before peer 2 |
| 2nd span | 66thbis | Bottom | 16th segment after peer 1 | 16th segment before peer 2 |
| 2nd span | 1st & 2nd (b) | upper | Peer 2 | 2nd segment towards peer 1 |
| 2nd span | 3rd & 4th (b) | Upper | Peer 2 | 3rd segment towards peer 1 |
| 2nd span | 5th & 6th (b) | Upper | Peer 2 | 4th segment towards peer 1 |
| 2nd span | 7th & 8th (b) | Upper | Peer 2 | 5th segment towards peer 1 |
| 2nd span | 9th & 10th (b) | Upper | Peer 2 | 6th segment towards peer 1 |
| 2nd span | 11th & 12th (b) | Upper | Peer 2 | 7th segment towards peer 1 |
| 2nd span | 13th & 14th (b) | Upper | Peer 2 | 8th segment towards peer 1 |
| 2nd span | 15th & 16th (b) | Upper | Peer 2 | 9th segment towards peer 1 |
| 2nd span | 17th & 18th (b) | Upper | Peer 2 | 10th segment towards peer 1 |
| 2nd span | 19th & 19ath (b) | Upper | Peer 2 | 11th segment towards peer 1 |
| 2nd span | 20th & 21fst (b) | Upper | Peer 2 | 12th segment towards peer 1 |

| | | | | |
|---|---|---|---|---|
| 2nd span | 22nd & 22and (b) | Upper | Peer 2 | 13th segment towards peer 1 |
| 2nd span | 23rd (b) | Upper | Peer 2 | 14th segment towards peer 1 |
| 2nd span | 24th (b) | Upper | Peer 2 | 15th segment towards peer 1 |
| 2nd span | 25th (b) | Upper | Peer 2 | 16th segment towards peer 1 |
| 2nd span | 26th (b) | Upper | Peer 2 | 17th segment towards peer 1 |

*Table 19 tendons layout of span 2*

| Number of span. | Tendon number | Location of Tendon | Starting point | Ending point |
|---|---|---|---|---|
| 3rd span | 1st & 2nd (b) | upper | Peer 2 | 2nd segment towards peer 3 |
| 3rd span | 3rd & 4th (b) | Upper | Peer 2 | 3rd segment towards peer 3 |
| 3rd span | 5th & 6th (b) | Upper | Peer 2 | 4th segment towards peer 3 |
| 3rd span | 7th & 8th (b) | Upper | Peer 2 | 5th segment towards peer 3 |
| 3rd span | 9th & 10th (b) | Upper | Peer 2 | 6th segment towards peer 3 |
| 3rd span | 11th & 12th (b) | Upper | Peer 2 | 7th segment towards peer 3 |
| 3rd span | 13th & 14th (b) | Upper | Peer 2 | 8th segment towards peer 3 |
| 3rd span | 15th & 16th (b) | Upper | Peer 2 | 9th segment towards peer 3 |
| 3rd span | 17th & 18th (b) | Upper | Peer 2 | 10th segment towards peer 3 |
| 3rd span | 19th & 19ath (b) | Upper | Peer 2 | 11th segment towards peer 3 |
| 3rd span | 20th & 21fst (b) | Upper | Peer 2 | 12th segment towards peer 3 |
| 3rd span | 22nd & 22and (b) | Upper | Peer 2 | 13th segment towards peer 3 |
| 3rd span | 23rd (b) | Upper | Peer 2 | 14th segment towards peer 3 |
| 3rd span | 24th (b) | Upper | Peer 2 | 15th segment towards peer 3 |
| 3rd span | 25th (b) | Upper | Peer 2 | 16th segment towards peer 3 |

| | | | | |
|---|---|---|---|---|
| 3rd span | 26th (b) | Upper | Peer 2 | 17th segment towards peer 3 |
| 3rd span | 81st a | Bottom | Peer 3 | 15th segments towards peer 3 |
| 3rd span | 81st | Bottom | Peer 3 | 14th segments towards peer 3 |
| 3rd span | 80th | Bottom | Peer 3 | 13th segments towards peer 3 |
| 3rd span | 79th | Bottom | Peer 3 | 12th segments towards peer 3 |
| 3rd span | 29th & 28th | upper | Peer 3 | 3rd segment towards peer 2 |
| 3rd span | 31st & 30th | Upper | Peer 3 | 4th segment towards peer 2 |
| 3rd span | 32nd & 33rd | Upper | Peer 3 | 5th segment towards peer 2 |
| 3rd span | 34th & 35th | Upper | Peer 3 | 6th segment towards peer 2 |
| 3rd span | 36th | Upper | Peer 3 | 7th segment towards peer 2 |
| 3rd span | 38th | Upper | Peer 3 | 8th segment towards peer 2 |
| 3rd span | 39th | Upper | Peer 3 | 9th segment towards peer 2 |
| 3rd span | 40th | Upper | Peer 3 | 10th segment towards peer 2 |

*Table 20 tendon layout of span 3*

| Number of span. | Tendon number | Location of Tendon | Starting point | Ending point |
|---|---|---|---|---|
| 4th span | 29th & 28th | Upper | Peer 3 | 2nd segment towards peer 4 |
| 4th span | 31st & 30th | Upper | Peer 3 | 3rd segment towards peer 4 |
| 4th span | 32nd & 33rd | Upper | Peer 3 | 4th segment towards peer 4 |
| 4th span | 34th & 35th | Upper | Peer 3 | 5th segment towards peer 4 |
| 4th span | 36th | Upper | Peer 3 | 6th segment towards peer 4 |
| 4th span | 38th | Upper | Peer 3 | 7th segment towards peer 4 |
| 4th span | 39th | Upper | Peer 3 | 8th segment towards peer 4 |

| | | | | |
|---|---|---|---|---|
| 4th span | 40th | Upper | Peer 3 | 9th segment towards peer 4 |
| 4th span | 87thd and 87thc | Bottom | 2nd segment after peer 3 | 2nd segment before peer 4 |
| 4th span | 87tha and 87thb | Bottom | 3rd segment after peer 3 | 3rd segment before peer 4 |
| 4th span | 86th | Bottom | 4th segment after peer 3 | 4th segment before peer 4 |
| 4th span | 85tha & 85th | Bottom | 5th segment after peer 3 | 5th segment before peer 4 |
| 4th span | 84th | Bottom | 6th segment after peer 3 | 6th segment before peer 4 |
| 4th span | 83rd | Bottom | 7th segment after peer 3 | 7th segment before peer 4 |
| 4th span | 82nd | Bottom | 8th segment after peer 3 | 8th segment before peer 4 |
| 4th span | 41st & 42nd | Upper | Peer 4 | 2nd segment towards peer 3 |
| 4th span | 43rd & 44th | Upper | Peer 4 | 3rd segment towards peer 3 |
| 4th span | 45th & 46th | Upper | Peer 4 | 4th segment towards peer 3 |
| 4th span | 47th & 48th | Upper | Peer 4 | 5th segment towards peer 3 |
| 4th span | 49th & 49ath | Upper | Peer 4 | 6th segment towards peer 3 |
| 4th span | 51st | Upper | Peer 4 | 7th segment towards peer 3 |
| 4th span | 52nd & 52ath | Upper | Peer 4 | 8th segment towards peer 3 |
| 4th span | 53rd | Upper | Peer 4 | 9th segment towards peer 3 |

*Table 21 tendon layout of span 4*

| Number of span. | Tendon number | Location of Tendon | Starting point | Ending point |
|---|---|---|---|---|
| 5th span | 41st & 42nd | upper | Peer 4 | 2nd segment towards peer 5 |
| 5th span | 43rd & 44th | Upper | Peer 4 | 3rd segment towards peer 5 |
| 5th span | 45th & 46th | Upper | Peer 4 | 4th segment towards peer 5 |
| 5th span | 47th & 48th | Upper | Peer 4 | 5th segment towards peer 5 |

| | | | | |
|---|---|---|---|---|
| 5th span | 49th & 49ath | Upper | Peer 4 | 6th segment towards peer 5 |
| 5th span | 51st | Upper | Peer 4 | 7th segment towards peer 5 |
| 5th span | 52nd & 52ath | Upper | Peer 4 | 8th segment towards peer 5 |
| 5th span | 53rd | Upper | Peer 4 | 9th segment towards peer 5 |
| 5th span | 60th | Upper | Peer 5 | 4th segment towards peer 4 |
| 5th span | 59th | Upper | Peer 5 | 5th segment towards peer 4 |
| 5th span | 58th | Upper | Peer 5 | 4th segment towards peer 4 |
| 5th span | 56th | Upper | Peer 5 | 3rd segment towards peer 4 |
| 5th span | 55th & 54th | Upper | Peer 5 | 2nd segment towards peer 4 |
| 5th span | 92cnd | Bottom | 2nd segment after peer 4 | 1st segment before peer 5 |
| 5th span | 92dnd | Bottom | 2nd segment after peer 4 | 3rd segment before peer 5 |
| 5th span | 92bnd | Bottom | 3rd segment after peer 4 | 1st segment before peer 5 |
| 5th span | 92and | Bottom | 4th segment after peer 4 | 2nd segment before peer 5 |
| 5th span | 91fst | Bottom | 5th segment after peer 4 | 2nd segment before peer 5 |
| 5th span | 90th | Bottom | 6th segment after peer 4 | 3rd segment before peer 5 |
| 5th span | 89th | Bottom | 7th segment after peer 4 | 4th segment before peer 5 |
| 5th span | 88th | Bottom | 8th segment after peer 4 | 5th segment before peer 5 |

*Table 22 tendon layout of span 5*